



POLITECNICO
MILANO 1863

SCUOLA DI INGEGNERIA INDUSTRIALE
E DELL'INFORMAZIONE

EXECUTIVE SUMMARY OF THE THESIS

Time Dependent Mathematical Modeling of Fluid and Protein transport in Microvascular Vessels

LAUREA MAGISTRALE IN MATHEMATICAL ENGINEERING - INGEGNERIA MATEMATICA

Author: ALBERTO ICARDI

Advisor: PROF. RICCARDO SACCO

Co-advisor: PROF. GIOVANNA GUIDOBONI

Academic year: 2021-2022

1. Introduction

Blood exchange between the microvascular system and tissues plays a key role in meeting the metabolic demand that sustains optimal organ function. Vascular delivery depends on vessel architecture, structure of the capillary membrane as well as the distribution of driving forces, such as hydrostatic and osmotic pressures [5]. Alteration of any of these properties can cause acute pathological conditions. The major example is interstitial edema, an excessive accumulation of fluid in the tissue, which increases the diffusion distance for oxygen and other nutrients and limits the diffusional removal of potentially toxic byproducts. At present, there is a lack of appropriate mathematical models for interpreting data derived from physiological experiments conducted at the cellular, single vessel segment, and whole organ levels. In this context, the stationary model on fluid and protein exchange in microvascular networks presented in [1] has been the first quantitative research. The authors of [1] demonstrated the importance of modelling a heterogeneous microvascular network, where each vessel has its own physical dimensions and biophysiological properties. They focused on the function that plasma proteins play in regulat-

ing fluid homeostasis. Albumin, for example, is the major determinant of plasma colloid osmotic pressure, which regulates the movement of fluids across the microvessel walls [5]. The experimental data used in [1] for model calibration are the same ones we consider in this thesis, and are measurements performed in an *in vivo* frog (*Rana pipiens*) mesenteric microvascular network.

The goal of this thesis is to continue the research started in [1] expanding the model to the non-stationary case. The fact that all variables and parameters are time-dependent allows us to simulate capillary membrane changes and pressure alterations, enlarging the perspective from just the vessel biophysical analysis. What we determined is that a sudden inability of the capillary to retain proteins in the vascular compartment, as may occur in inflammation, sepsis, or vascular remodelling, induces an osmotic gradient sufficiently large to generate the pathological condition of edema. We also investigated the effect of injecting new proteins into the capillary or administering the Atrial natriuretic peptide (ANP) as possible treatments. ANP is a hormone involved in homeostatic control, which is capable of promoting fluid reabsorption acting

on membrane hydraulic conductivity [3].

2. Time dependent model

We take advantage of this section to summarize the main steps performed for the derivation of the time dependent model of fluid and protein transport in a microvascular vessel. The first assumption is the approximation of the vessel geometry as a straight rigid cylinder of length L and radius R , with constant circular cross-section. Therefore, the equations employ a local system of cylindrical coordinates in which r , s and θ are the radial, axial and angular coordinates, with $r \in [0, R]$, $s \in (0, L)$ and $\theta \in [0, 2\pi]$, as shown in Figure 1.

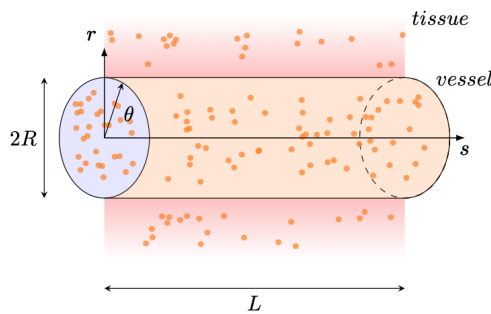


Figure 1: Schematic representation of the vessel geometry.

The second step is the blood fluid phase modeling, which relies upon the theory of multicomponent mixtures (see [4], Chapter 8). Specifically, we focus on water and proteins, which play the major role in the microvascular exchange. Then, considering additional assumptions such as that volumetric forces and sources of mass are absent, water is an incompressible fluid and the mixture is a dilute solution of proteins in water, we obtain the following equations:

$$\nabla \cdot \underline{\mathbf{v}}_w = 0, \quad (1a)$$

$$\rho_{fp} \frac{\partial \underline{\mathbf{v}}_w}{\partial t} = -\nabla p + 2\mu_w \Delta \underline{\mathbf{v}}_w, \quad (1b)$$

$$\frac{\partial C}{\partial t} + \nabla \cdot (C \underline{\mathbf{v}}_w - D_{pt} \nabla C) = 0. \quad (1c)$$

Eqs. (1a) and (1c) represent the balance of mass for the fluid and protein components, respectively, whereas Eq. (1b) represents the balance of linear momentum for the fluid phase. The unknowns of system (1) are the water velocity $\underline{\mathbf{v}}_w$, the hydrostatic pressure p and the protein

concentration C . Instead, the parameters are the fluid phase partial density ρ_{fp} , the water dynamic viscosity μ_w and the protein diffusion coefficient D_{pt} .

Our interest is in computing the fluid and protein exchange fluxes between the microvessel and the surrounding tissue, rather than in finding the values of the variables in (1) at each point in the domain. For this reason, the final step consists in reducing the equations of (1) to the only dependence on the axial coordinate s along the vessel centerline (Figure 1). For this purpose, we first notice that axial symmetry holds for all involved variables, which means that all problem unknowns do not depend on the angular coordinate θ , and then we integrate the equations over the tube cross-section. This procedure transforms velocities into axial and lateral flows leading to the following reduced coupled model for the transport of fluid and proteins:

$$\frac{\partial q_f}{\partial s} + j_f = 0, \quad (2a)$$

$$\frac{\rho_{fp}}{\pi R^2} \frac{\partial q_f}{\partial t} = -\frac{\partial p}{\partial s} - \frac{2\mu_w(\gamma + 2)}{\pi R^4} q_f, \quad (2b)$$

$$\frac{\partial C}{\partial t} + \frac{1}{\pi R^2} \frac{\partial q_p}{\partial s} + \frac{j_p}{\pi R^2} = 0, \quad (2c)$$

$$q_p = C q_f - \pi R^2 D \frac{\partial C}{\partial s}. \quad (2d)$$

From the mathematical viewpoint, the model in (2) is a first-order system of nonlinearly coupled partial differential equations whose solution consists of finding the four dependent variables $q_f = q_f(s, t)$, $p = p(s, t)$, $q_p = q_p(s, t)$ and $C = C(s, t)$ for $s \in (0, L)$ and $t \in (0, T)$, for given suitable initial and boundary conditions. The unknowns q_f and q_p are the axial volumetric flow rate ($cm^3 s^{-1}$) and the axial mass flow rate ($g s^{-1}$), respectively. The equations in (2) already include the boundary conditions on the lateral surface of the vessel, since these conditions are incorporated into the specific lateral volumetric flow rate j_f ($cm^2 s^{-1}$) and the specific lateral mass flow rate j_p ($cm^{-1} g s^{-1}$). These physical quantities represent the fluid volume and the mass of proteins exiting the membrane per unit length and time. The flow rate j_f can be expressed using the Starling equation [2] as:

$$j_f(s, t) = 2\pi R L_p (\Delta p - \sigma \Delta \pi), \quad (3)$$

where Δp and $\Delta\pi$ are the difference between the vascular compartment and the tissue in hydrostatic and osmotic pressure, respectively. The other parameters in (3) are the hydraulic conductivity L_p , which describes the leakiness of the membrane to water, and the osmotic reflection coefficient σ , which, varying between 0 and 1, indicates the likelihood that a molecule approaching a pore in the membrane is reflected back and retained in the vascular system. Thanks to Van't Hoff relation, the osmotic pressure π can be represented as a function of protein concentration as:

$$\pi = a_1 C, \quad (4)$$

where a_1 is a given constant. The flow rate j_p can be expressed through a modified form of Fick's first law of diffusion as:

$$j_p(s, t) = 2\pi R \frac{1 - \sigma}{\sigma} P_d \Delta C, \quad (5)$$

where ΔC is the difference of protein concentration between the vascular space and the tissue, and P_d is the solute permeability of the membrane.

3. Computational algorithm

Finding a numerical solution to system (2) is a nontrivial problem and requires the adoption of diverse mathematical and numerical methods. Time discretization is performed using Backward Euler method, which reduces the solution of problem (2) to performing the following procedure for each time step: $\forall n \geq 0$, given $q_f^n(s)$, $p^n(s)$, $q_p^n(s)$ and $C^n(s)$, find the functions $q_f(s)$, $p(s)$, $q_p(s)$ and $C(s)$ solving the following systems of equations:

Fluid block:

$$\left\{ \begin{array}{l} \frac{\partial q_f}{\partial s} + 2\pi R L_p (p - \sigma a C) = 0, \\ \frac{\rho}{\pi R^2} \frac{\partial q_f}{\partial t} = \frac{\rho}{\pi R^2} \frac{\partial q_f^n}{\partial t} - \frac{\partial p}{\partial s} - \alpha q_f. \end{array} \right. \quad (6a)$$

$$\left\{ \begin{array}{l} \frac{\partial q_f}{\partial s} + 2\pi R L_p (p - \sigma a C) = 0, \\ \frac{\rho}{\pi R^2} \frac{\partial q_f}{\partial t} = \frac{\rho}{\pi R^2} \frac{\partial q_f^n}{\partial t} - \frac{\partial p}{\partial s} - \alpha q_f. \end{array} \right. \quad (6b)$$

Protein block:

$$\left\{ \begin{array}{l} \frac{C}{\Delta t} + \frac{1}{\pi R^2} \frac{\partial q_p}{\partial s} + \frac{2(1 - \sigma)}{\sigma R} P_d C = \frac{C^n}{\Delta t}, \\ q_p = C q_f - \pi R^2 D \frac{\partial C}{\partial s}. \end{array} \right. \quad (7a)$$

$$(7b)$$

Denoting $u(s, t)$ a generic unknown variable of problem (2), in systems (6) and (7) we indicate

with $u^n(s)$ and $u(s)$ its numerical approximation at the instants t^n and t^{n+1} , respectively. We also consider $\alpha = \frac{2\mu_w(\gamma+2)}{\pi R^4}$ and the values of the pressures and protein concentration in the tissue equal to zero, according to the experimental conditions adopted in [1]. The major difficulty in the solution of systems (6) and (7) is related to the nonlinear coupling of the two blocks for fluid and protein, which appears in equation (7b), where the variables C and q_f are present in product form. To address this problem we decouple the equations using fixed-point iterations. In essence, each step k , $k \geq 0$, of the iterative procedure consists of:

Step 1: Fluid block

- 1.1 Set $C(s) = C^{(k)}(s)$ for $s \in (0, L)$ in equation (6a);
- 1.2 Solve the fluid system (6), supplied by boundary conditions, to determine the function $p(s) = p^{(k+1)}(s)$ for $s \in (0, L)$.

Step 2: Protein block

- 2.1 Compute the flow rate $q_f(s) = q_f^{(k+1)}(s)$ for $s \in (0, L)$ through equation (6b);
- 2.2 Solve the protein system (7), supplied by boundary conditions, to determine the function $C(s) = C^{(k+1)}(s)$ for $s \in (0, L)$.

Step 3: Convergence checks

- 3.1 Compute the iteration error $err^{(k)}$ to estimate the difference between the functions $p^{(k+1)}$ and $C^{(k+1)}$ from $p^{(k)}$ and $C^{(k)}$;
- 3.2 If $err^{(k)} < toll$, then the fixed-point iteration has reached convergence, otherwise the procedure is repeated starting from Step 1.

Steps 1 and 2 require the solution of diffusion-advection-reaction problems which is conducted using a displacement-based form of the Galerkin finite element approximation with piecewise linear finite elements. In the case of the protein block, the influence of the advective field $q_f^{(k+1)}$ makes the problem strongly advection-dominated. This requires the adoption of a stabilization technique to prevent the numerical solution from being affected by spurious unphysical oscillations. In the numerical algorithm implemented in the thesis we use the exponentially-fitted stabilization, proposed by Scharfetter and Gummel for the simulation of the drift-diffusion equations in semiconductor devices.

4. Energy and numerical errors

Validation of the algorithm illustrated in Section 3 is conducted by studying the energy consistency of the fixed-point iterations, and finding an exact solution in the ideal case with no proteins, in order to compute numerical errors. Specifically, starting from the equations in (2), we derive an energy identity of the form:

$$\frac{d\mathcal{E}}{dt} + \mathcal{D} = \mathcal{F}, \quad (8)$$

where \mathcal{E} represents the energy of the problem, whereas \mathcal{D} and \mathcal{F} denote the dissipative and forcing terms, respectively. The approach used in our thesis consists of writing the integral forms of the problem equations in (2), multiplying them by appropriate test functions. The resulting energy has the following expression:

$$\begin{aligned} \mathcal{E} &= \frac{1}{2} \frac{\rho}{\pi R^2} \int_0^L q_f^2 ds \\ &+ \lambda K_B T \int_0^L C \left(\ln \left(\frac{C}{C_{ref}} \right) - 1 \right) ds, \end{aligned} \quad (9)$$

where K_B is the Boltzmann constant, T is the temperature, C_{ref} is a reference concentration and $\lambda = \frac{\sigma a_1 \pi R^2}{K_B T}$. Since the dissipation terms in (8) are nonnegative, the energy of the problem decreases over time in absence of forcing terms. This fact occurs also in the numerical energy once the equations are decoupled with fixed point iterations (Figure 2). The finding that energy remains bounded is an evidence of the method stability. Moreover, the computation of the energy identity at each k -th step of the fixed-point iteration proved that the decrease in energy over time, in absence of forcing terms, is a necessary condition for the method convergence.

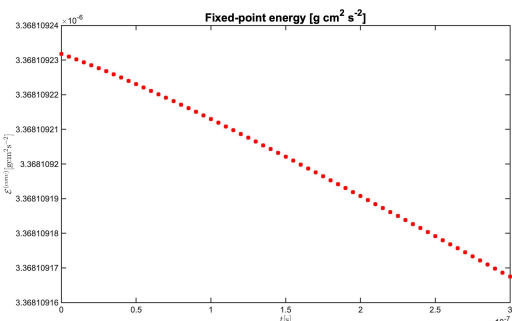


Figure 2: Fixed-point energy plotted over time.

In addition to the energy, we construct an a priori exact solution to examine numerical errors. In particular, to properly test the piecewise linear finite element method, we choose to consider an academic sinusoidal exact solution that can be expressed as:

$$p(s, t) = e^{\lambda t} (\cos(k s) + \sin(k s)). \quad (10)$$

Substituting the function for p in Eq. (10) into the equations of problem (2), in the ideal case with no proteins, we find suitable expressions for the parameters λ and k , as well as the expression for the flow rate q_f . Boundary and initial conditions are set a posteriori. Thanks to this exact solution, we can compute L_∞ -errors and L_2 -errors for both fluid variables p and q_f . These errors allow us to perform two convergence analyses, one refining the time mesh and the other refining the space mesh. The orders of convergence of the computational algorithm illustrated in Section 3 are given in Table 1 (time refining) and in Table 2 (space refining).

Time convergence order

$\mathcal{O}(\text{Err}_{L_\infty}(p))$	0.979	0.988	0.995	0.999	1.002
$\mathcal{O}(\text{Err}_{L_\infty}(q_f))$	0.996	0.998	0.999	1.000	1.002
$\mathcal{O}(\text{Err}_{L_2}(p))$	0.977	0.988	0.995	0.999	1.003
$\mathcal{O}(\text{Err}_{L_2}(q_f))$	0.996	0.998	1.000	1.002	1.005

Table 1: Order of convergence of the errors computed by progressively refining the time mesh.

Space convergence order

$\mathcal{O}(\text{Err}_{L_\infty}(p))$	1.937	1.990	1.979	1.993	1.998
$\mathcal{O}(\text{Err}_{L_\infty}(q_f))$	1.449	1.733	1.891	2.024	2.379
$\mathcal{O}(\text{Err}_{L_2}(p))$	1.442	1.473	1.488	1.496	1.499
$\mathcal{O}(\text{Err}_{L_2}(q_f))$	1.338	1.459	1.495	1.391	0.459

Table 2: Order of convergence of the errors computed by progressively refining the space mesh.

In particular, the results in Table 1 are coherent with the theoretical estimate of the Backward Euler's truncation error, which is linear in time for parabolic problems. Even the results in Table 2 reflect the theoretical estimates for the Galerkin finite element method, with the L_∞ -error of order 2, and the L_2 -error which has more than linear order. Table 2 also highlights that the axial volumetric flow rate q_f is

affected by round-off error in correspondence of very small values of the discretization parameter h .

5. Simulations in physiological and pathological conditions

This section summarizes the main findings of physiological interest. The most significant physical quantities are the total lateral volumetric flow rate J_f and the total lateral mass flow rate J_p , which represent the fluid volume and the mass of proteins exiting the whole lateral surface of the vessel per unit time, respectively. They are computed as follows:

$$J_f(t) = \int_0^L j_f(s, t) ds. \quad (11a)$$

$$J_p(t) = \int_0^L j_p(s, t) ds. \quad (11b)$$

We start by examining the nonpathological scenario, which is simulated by keeping all model parameters constant over time equal to their basal values, and imposing a pressure gradient that drives fluid movement. In particular, the reflection coefficient σ and the hydraulic conductivity L_p are equal to 0.8 and $1.5 \cdot 10^{-7} \text{ cm s}^{-1} \text{ cmH}_2\text{O}^{-1}$, respectively. In this scenario, the amount of protein moving across the membrane is negligible compared to the concentration of protein within the vascular space. As a consequence, protein flux does not affect osmotic pressure π and, under nonpathological conditions, the flow rates J_f and J_p remain constant over time (Figure 3). Next, we simulate the pathological scenario corresponding to a sudden decrease in the reflection coefficient σ , which jumps from the basal value of 0.8 to 0.01. This change causes the inability of the membrane to retain proteins within the vascular space and manifests as a leakage of both protein and fluid into the tissue, leading to edema (Figure 4). Specifically, J_f increases from a rate of $1.2 \cdot 10^{-10} \text{ cm}^{-3} \text{ s}^{-1}$ to $5 \cdot 10^{-10} \text{ cm}^{-3} \text{ s}^{-1}$, because of the osmotic gradient generated by the protein flow into the tissue. J_p undergoes a huge increase from $3.57 \cdot 10^{-13} \text{ g s}^{-1}$ to a value of $1.34 \cdot 10^{-10} \text{ g s}^{-1}$. As expected, once this increase of 3 orders of magnitude is recorded, J_p decreases slightly, since less protein remains in the vascular space.

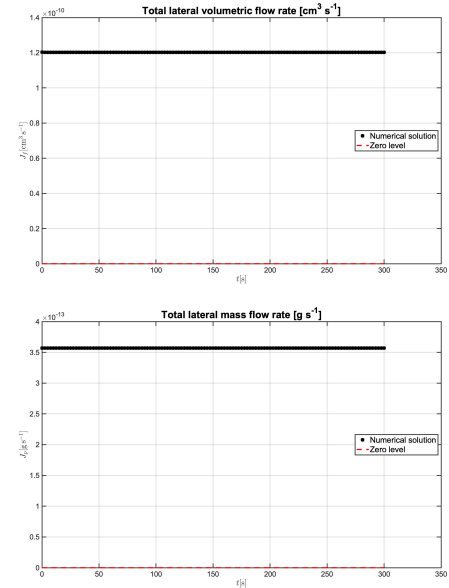


Figure 3: Visualization of the flow rates J_f (top) and J_p (bottom) plotted as a function of time, in the nonpathological scenario.

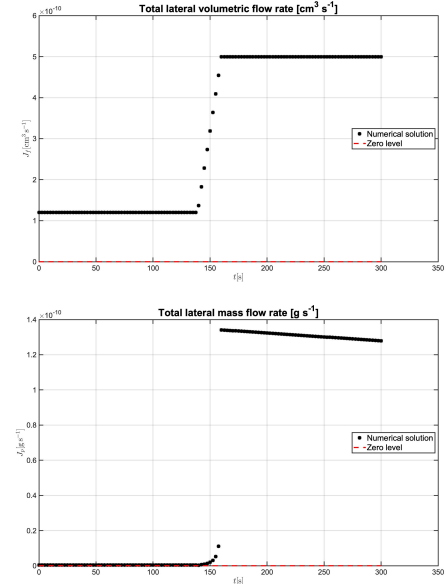


Figure 4: Visualization of flow rates J_f (top) and J_p (bottom) plotted as a function of time, in the pathological scenario.

Finally, we simulate two possible treatments. The first one consists of injecting new proteins inside the capillary in order to rebalance the osmotic pressures acting across the microvascular walls. To produce this effect we act on the boundary conditions. In this case, the lateral volumetric flow rate J_f (Figure 5, top), after rising to pathological levels, is lowered when the

increase in concentration in the capillary takes place. The second treatment consists of the administration of the Atrial natriuretic peptide (ANP) in a venular capillary, where fluid reabsorption is predominant. ANP induces an approximately twofold increase in hydraulic conductivity L_p and makes the capillary absorb about twice as amount of fluid (see J_f at the bottom of Figure 5). For this reason, Atrial natriuretic peptide may play a key role in the treatment of interstitial edema.

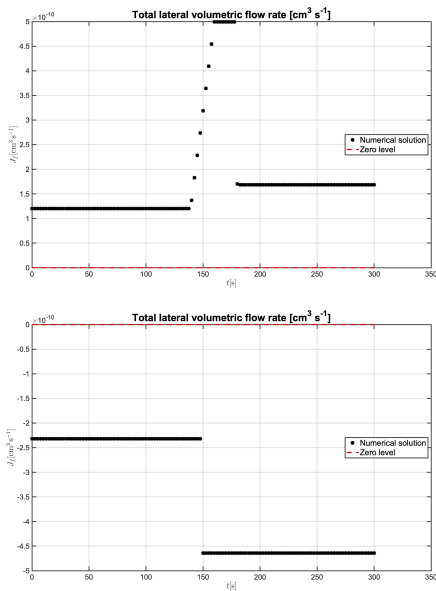


Figure 5: Visualization of flow rate J_f plotted as a function of time, in the case where new proteins are injected inside the capillary (top) and the Atrial natriuretic peptide is administered (bottom).

6. Conclusions

This work developed a time-dependent mathematical model of fluid and protein transport in microvascular vessels, with the aim of investigating fluid exchanges between the vascular system and body tissues. The model was a system of nonlinearly coupled partial differential equations and we used fixed-point iterations to decouple the equations for the fluid part from the equations for the protein part. The first finding was that this decoupling is numerically stable since the fixed-point method keeps the energy bounded. Further, Backward Euler method, together with Galerkin finite element approximation, resulted in a convergent computational algorithm, as proven by the error analysis shown

in Section 4.

As far as the physiological results are concerned, the main finding was that the protein leakage, due to a sudden decrease in the reflection coefficient, was able to induce an osmotic gradient sufficiently large to generate the pathological condition of edema. In this context, this thesis also provides two possible treatments. The major limitation of this work is that the current time-dependent model focuses on a single vessel. Of course, future work will need to extend this non-stationary model to the full network of capillaries. Another interesting development might be the testing of new methods to decouple the fluid-protein problem. A method such as operator splitting for example, which does not need to perform iterations at each time step, might be more efficient. However, its numerical stability remains a critical issue, although the energy balances derived in this thesis are an excellent starting point for tackling this new challenge.

References

- [1] G Guidoboni, N M Marazzi, J Fraser, R Sacco, K Palaniappan, and V H Huxley. Fluid and protein exchange in microvascular networks: Importance of modelling heterogeneity in geometrical and biophysical properties. *J Physiol*, 599:4597–4624, 2021.
- [2] J R Levick. Revision of the starling principle: new views of tissue fluid balance. *J Physiol*, 557, 2004.
- [3] DJ Meyer and VH Huxley. Differential sensitivity of exchange vessel hydraulic conductivity to atrial natriuretic peptide. *Am J Physiol*, 1990.
- [4] R Sacco, G Guidoboni, and A G Mauri. A comprehensive physically based approach to modeling in bioengineering and life sciences. *Elsevier*, 2019.
- [5] J Scallan, V H Huxley, and R J Korthuis. Capillary fluid exchange: Regulation, functions, and pathology. *San Rafael (CA): Morgan Claypool Life Sciences*, 2010.



POLITECNICO
MILANO 1863

SCUOLA DI INGEGNERIA INDUSTRIALE
E DELL'INFORMAZIONE

Time Dependent Mathematical Modeling of Fluid and Protein transport in Microvascular Vessels

TESI DI LAUREA MAGISTRALE IN
MATHEMATICAL ENGINEERING - INGEGNERIA MATEMATICA

Author: **Alberto Icardi**

Student ID: 945579

Advisor: Prof. Riccardo Sacco

Co-advisor: Prof. Giovanna Guidoboni

Academic Year: 2021-22

Abstract

Mathematical models are nowadays a fundamental tool for the interpretation of experimental data. This thesis develops a fluid dynamics time dependent computational model, which describes fluid and protein transport in microvessels using measurements in an *in vivo* frog (*Rana pipiens*) mesenteric microvascular network. The model implementation decouples the equations for the fluid part from the equations for the protein part, using fixed-point iterations, which turn out to be reliable, stable and energetically consistent. The model objective is to analyze which factors lead to the pathological condition of edema, an excessive accumulation of fluid in the tissue, which compromises cellular metabolism and normal organ function. For this purpose variables referred to the fluid dynamics, such as pressure or axial and lateral fluxes, but also physiological parameters, which describe the structure of the vascular wall, are examined to simulate different scenarios. Specifically, this thesis focuses on the scenario in which the vascular membrane suddenly loses its ability to retain proteins in the vascular compartment, as may occur in inflammation, sepsis, or vascular remodelling. To perform this simulation, the osmotic reflection coefficient is subject to a time variation. The main finding is that a sudden decrease in the reflection coefficient induces an osmotic gradient sufficiently large to generate fluid flow in the tissue, leading to the edema condition. Finally, possible treatments are proposed, such as injecting new proteins inside the capillary, or acting on the membrane hydraulic conductivity to promote fluid reabsorption.

Keywords: Microvascular Networks, Mathematical Model, Fixed-point Iterations, Osmotic Reflection Coefficient, Interstitial Edema

Abstract in lingua italiana

I modelli matematici sono oggi uno strumento fondamentale per l'interpretazione dei dati sperimentali. Questa tesi sviluppa un modello computazionale fluidodinamico dipendente dal tempo, che descrive il trasporto di fluidi e proteine nei microvasi utilizzando le misurazioni in vivo effettuate in una rete microvascolare mesenterica di una rana (*Rana pipiens*). L'implementazione del modello viene realizzata tramite il disaccoppiamento delle equazioni per la parte fluida da quelle per la parte proteica. In questo lavoro tale disaccoppiamento è stato affrontato utilizzando le iterazioni di punto fisso, che si sono rivelate affidabili, stabili ed energeticamente consistenti. L'obiettivo del modello è analizzare quali fattori portano alla condizione patologica dell'edema, un accumulo eccessivo di liquido nel tessuto, che compromette il metabolismo cellulare e il normale funzionamento degli organi. A questo scopo vengono incorporate nel modello variabili riferite alla fluidodinamica, come le pressioni o i flussi assiali e laterali, ma anche parametri fisiologici, che descrivono la struttura della parete vascolare. Poiché tutte queste variabili sono sotto controllo, questo approccio consente di simulare diversi scenari. In particolare, questa tesi si concentra sullo scenario in cui la membrana capillare perde improvvisamente la capacità di trattenere le proteine nel compartimento vascolare, come può accadere in caso di infiammazione, sepsi o rimodellamento vascolare. Per effettuare questa simulazione, il coefficiente di riflessione osmotica subisce una variazione nel tempo. Il risultato principale è che una diminuzione improvvisa del coefficiente di riflessione induce un gradiente osmotico sufficientemente grande da generare un flusso di fluido nel tessuto, causando la condizione di edema. Infine, vengono proposti possibili trattamenti, come l'注射 di nuove proteine all'interno del capillare o l'intervento sulla conducibilità idraulica della membrana per promuovere il riassorbimento del fluido.

Parole chiave: Rete Microvascolare, Modello Matematico, Iterazioni di Punto Fisso, Coefficiente di Riflessione Osmotica, Edema Interstiziale

Contents

Abstract	i
Abstract in lingua italiana	iii
Contents	v
Introduction	1
1 Fluid exchange in microvascular and lymphatic system	3
1.1 The Starling equation describing capillary filtration	4
1.2 Pathological Conditions: Edema and Systemic Capillary Leak Syndrome	7
2 Time dependent mathematical model of fluid and protein transport	9
2.1 Geometry of the model	9
2.2 Simplification of balance equations	11
2.3 Derivation of the reduced-order model for the water and protein homogeneous mixture	16
2.4 Coupled model for the transport of fluid and proteins	21
3 Energy of the model	25
3.1 Derivation of the energy balance	25
4 Computational algorithm	33
4.1 Backward Euler method	33
4.2 Fixed-point iteration	35
4.3 Finite element method for diffusion-advection-reaction problem	38
4.4 Exact solution ideal case with no proteins	40
4.5 Numerical results	42
5 Energy in the fixed-point iterations	51

5.1	Derivation of the energy balance in fixed-point iterations	51
5.2	Decrease in energy over time is a necessary condition for convergence	56
6	Simulations in physiological and pathological conditions	59
6.1	Nonpathological scenario	60
6.2	Pathological scenario with sudden decrease in reflection coefficient	65
6.3	Increasing protein concentration in the capillary may prevent edema condition	70
6.4	Atrial natriuretic peptide increases hydraulic conductivity promoting fluid reabsorption in venular capillaries	71
7	Conclusions and future developments	77
Bibliography		79
List of Figures		81
List of Tables		85
List of Symbols		87

Introduction

Blood exchange between the microvascular system and tissues plays a key role in meeting the metabolic demand that sustains optimal organ function [14]. Vascular delivery depends on vessel architecture, structure of the capillary membrane as well as the distribution of driving forces, such as hydrostatic and osmotic pressures [7, 14]. Alteration of any of these properties can cause acute pathological conditions. The major example is interstitial edema, an excessive accumulation of fluid in the tissue, which increases the diffusion distance for oxygen and other nutrients and limits the diffusional removal of potentially toxic byproducts. At present, there is a lack of appropriate mathematical models for interpreting data derived from physiological experiments conducted at the cellular, single vessel segment, and whole organ levels. In addition, most of mass transfer models in microvascular networks focus on gas exchange, particularly molecular oxygen (O_2) [4, 11]. However, this study is not surprising since the experimental analysis of this process has been fairly straightforward, considering that oxygen is associated with hemoglobin within the red blood cells and the red cell flux can be identified with minimal disturbance in a selection of living tissues. In this context, the stationary model on fluid and protein exchange in microvascular networks presented in [5] has been the first quantitative research. The authors of [5] demonstrated the importance of modelling a heterogeneous microvascular network, where each vessel has its own physical dimensions and biophysiological properties. They focused on the function that plasma proteins play in regulating fluid homeostasis. Albumin, for example, is the major determinant of plasma colloid osmotic pressure, which regulates the movement of fluids across the microvessel walls [14].

The goal of this thesis is to continue the research started in [5] expanding the model to the non-stationary case. The fact that all variables and parameters are time-dependent allows us to simulate capillary membrane changes and pressure alterations, enlarging the perspective from just the vessel biophysical analysis. What we determined is that a sudden inability of the capillary to retain proteins in the vascular compartment, as may occur in inflammation, sepsis, or vascular remodelling, induces an osmotic gradient sufficiently large to generate the pathological condition of edema. We also investigated the effect of injecting new proteins into the capillary or administering the Atrial natriuretic peptide

(ANP) as possible treatments. ANP is a hormone involved in homeostatic control, which is capable of promoting fluid reabsorption acting on membrane hydraulic conductivity [10].

The thesis is organized as follows. Chapter 1 presents a physiological overview of the fluid and protein exchange phenomena occurring in microvascular capillaries, introducing the variables involved, the Starling equation and the main pathological conditions. Chapter 2 illustrates the steps to derive the time-dependent mathematical model of fluid and protein transport, starting from the balance laws and describing blood on the basis of the multicomponent mixture theory. Chapter 3 derives the energy balance of the model. Chapter 4 describes the computational algorithm adopted to solve the problem numerically, and proves its validity by providing numerical error results in a test case, in which the exact solution has been obtained. Chapter 5 derives the energy balance once the fluid-protein problem has been decoupled using fixed-point iterations, and finds that the energy remains bounded, evidence of the method stability. Chapter 6 provides results of physiological interest, simulating the pathological condition of edema due to membrane structural changes, and proposing two possible treatments. Finally, conclusions and future developments are reported in Chapter 7.

1 | Fluid exchange in microvascular and lymphatic system

The cardiovascular and lymphatic systems play complementary roles within the human body. While vascular capillaries provide flux of oxygen and nutrients to the tissue cells, lymphatic vessels remove metabolic byproducts from the interstitium. In contrast to the blood vasculature which has been extensively studied, the lymphatics has been considered for years as a largely passive system for return of extravasated fluid and proteins to the blood circulation [2]. This misperception has faded in the past two decades, when the main role played by the lymphatic system in maintaining fluid-homeostasis became more evident. In particular, the accumulation of proteins into the interstitial spaces would alter the balance of forces regulating transcapillary fluid filtration, resulting in a redistribution of blood from the vascular space into the interstitial compartment that is incompatible with life [6]. In this context, the target of our thesis is to quantitatively study the exchange of fluid between microvascular endothelial barrier, cellular tissues and microlymphatic vessels, which intertwine in most parts of the human body as depicted in Figure 1.1.

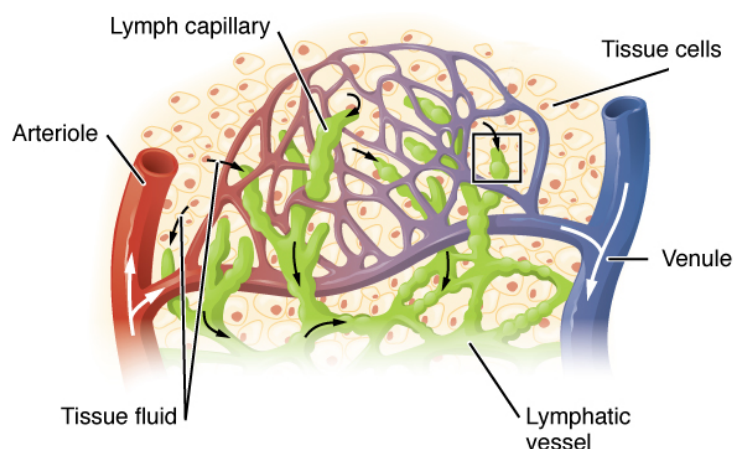


Figure 1.1: Microlymphatic vessels intertwine vascular capillaries in a cellular tissue.

1.1. The Starling equation describing capillary filtration

Under normal conditions, the balance of forces (hydrostatic and osmotic pressures) acting across the microvascular walls of blood capillaries promotes the net flux of fluid from the bloodstream to the interstitium, in a process referred to as capillary filtration. The interstitium is the space separating the microvascular wall and a structural barrier such as a cell membrane or an internal structures, such as organ, where the fluid flows before entering the lymphatic system.

To understand capillary fluid exchange and how plasma moves to the extravascular space we need to refer to the model proposed by Starling in 1896 [17]. According to his view the rate at which fluid is filtered across vascular endothelium is determined by three factors: the surface area (S), and two gradients in hydrostatic (Δp) and osmotic ($\Delta\pi$) pressure. In our context, Δp represents the difference between the capillary pressure (p_c) and the interstitial pressure (p_t), whereas $\Delta\pi$ represents the difference between the plasma protein osmotic pressure (π_c) and the interstitial protein osmotic pressure (π_t). As is well known, hydrostatic pressure causes fluid movement against gradient, thus capillary pressure (p_c) behaves as an outward force while interstitial pressure (p_t) acts as an absorptive force (Figure 1.2). On the other hand, osmosis is the tendency of the solvent to balance the concentration of solute between two compartments divided by a semipermeable membrane. Namely, solvent molecules move spontaneously from a region of lower solute concentration to a region of higher solute concentration and osmotic pressure is defined as the external pressure required to delete this net movement of solvent across the membrane. In view of these considerations, plasma osmotic pressure (π_c) favors the movement of fluid from the extravascular to vascular compartment, whereas interstitial osmotic pressure (π_t) tends to pull fluid out of the vascular space (Figure 1.2). Thanks to Van't Hoff relation, the osmotic pressure π can be represented as a function of protein concentration in a compartment:

$$\pi = \Phi n C \quad (1.1)$$

where Φ is a correction coefficient, n is the valence number, and C is the protein molar concentration.

In recent years, the Starling model has been improved by including two parameters to describe the transport properties of the membrane [9], leading to the modern form of the Starling equation:

$$J_f = L_p S (\Delta p - \sigma \Delta\pi) = L_p S \Delta p_{net}, \quad (1.2)$$

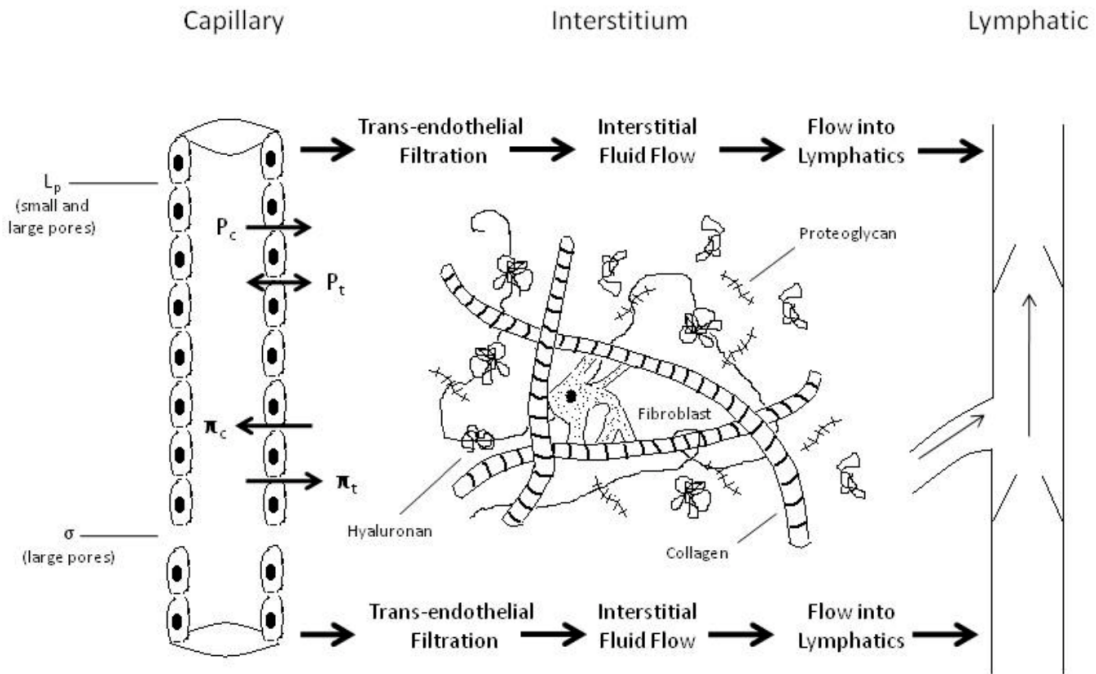


Figure 1.2: Capillary—interstitium—lymphatic fluid and protein exchange system depicting the Starling forces acting across the microvascular wall.

where J_f is the fluid flux ($\text{cm}^3 \text{s}^{-1}$) exiting the membrane, L_p is the hydraulic conductivity ($\text{cm s}^{-1} \text{cmH}_2\text{O}^{-1}$), σ is a unitless coefficient known as the osmotic reflection coefficient and Δp_{net} is the net filtration pressure. Under steady-state control conditions, Δp_{net} is slightly positive so that there is a net fluid movement into the tissues (capillary filtration). Obviously, in order to avoid incurring pathological conditions, interstitial fluid volume needs to remain constant and this is achieved by removal of interstitial fluid via the lymphatics (Figure 1.2).

The hydraulic conductivity L_p describes the leakiness of the membrane to water, whereas σ , the osmotic reflection coefficient, varies between 0 and 1 and indicates the likelihood that a molecule approaching a pore in the membrane is reflected back from the pore and retained in the vascular system. When $\sigma = 0$, all solute molecules pass through the membrane, corresponding to a situation in which osmotic pressure does not have any effect on fluid filtration. Under these conditions, Equation (1.2) simplifies as:

$$J_f = L_p S \Delta p. \quad (1.3)$$

In the opposite case, when $\sigma = 1$, all solute is reflected making the barrier act like a perfect semi-permeable membrane that allows only water to pass through.

1 | Fluid exchange in microvascular and lymphatic system

A graph of volume flux per unit surface area (J_f/S) as a function of hydrostatic pressure, according to Equation (1.2), yields a straight line with slope equal to the hydraulic conductivity (L_p) and intercept on the pressure (x) axis equal to $\sigma\Delta\pi$ (Figure 1.3).

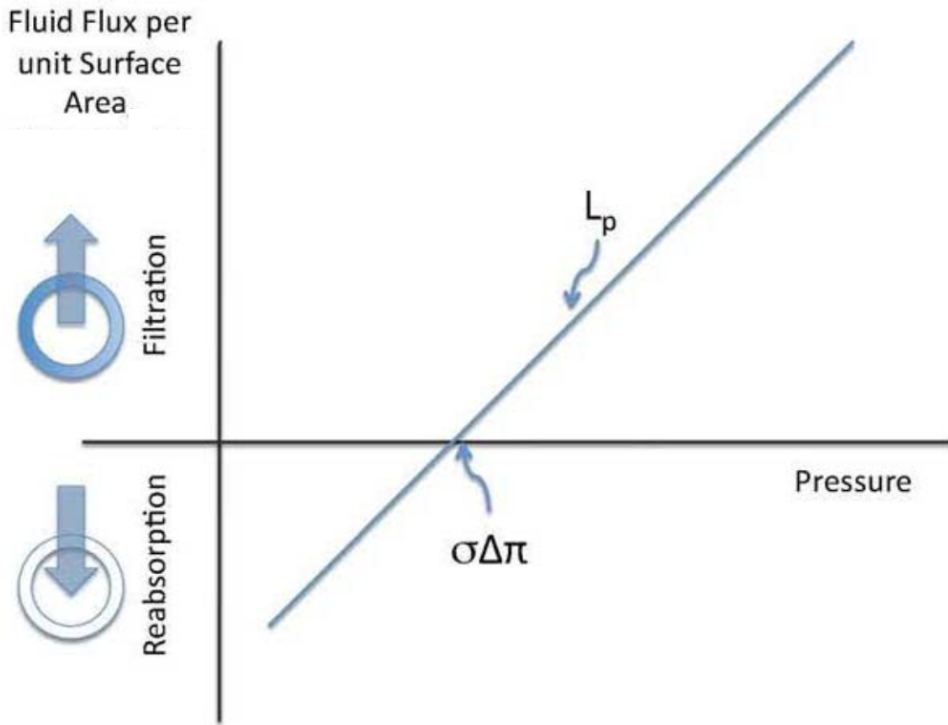


Figure 1.3: Graph of volume flux per unit surface area on hydrostatic pressure.

Another physical quantity of interest in fluid filtration is J_p , the flux of solute ($g s^{-1}$), proteins in our case. As a first approximation, this flux can be modeled by Fick's first law of diffusion as:

$$J_p = P_d S \Delta C = P_d S (C_c - C_t), \quad (1.4)$$

where P_d is the diffusive permeability coefficient ($cm s^{-1}$), C_c is the capillary protein concentration ($g cm^{-3}$) and C_t the interstitial protein concentration ($g cm^{-3}$). The diffusive permeability is defined as the ratio between the diffusion coefficient D_f for the solute ($cm^2 s^{-1}$) and the barrier thickness Δx (cm):

$$P_d = \frac{D_f}{\Delta x}. \quad (1.5)$$

More specifically, in our model, Fick's law (1.4) is modified by adding the factor $\frac{1-\sigma}{\sigma}$ to

account for the porous structure of the endothelial barrier (see for example [14]). Therefore J_p can be expressed as:

$$J_p = \frac{1 - \sigma}{\sigma} P_d S \Delta C. \quad (1.6)$$

If the vessel walls are impermeable to proteins (as is the case in specialized vessels in the brain), then $J_p = 0$. Conversely, if the vessel walls are leaky to proteins (as occurs in the pathophysiological state of vessel injury from sepsis to trauma) then J_p is positive or negative depending on whether proteins are moving from the vascular compartment into the interstitium or vice versa.

1.2. Pathological Conditions: Edema and Systemic Capillary Leak Syndrome

Edema is the build-up of fluid in the body's tissue, either within cells (cellular edema) or within the interstitial spaces (interstitial edema) [1]. This thesis focus on interstitial edema, which may occur as a consequence of alterations in hydrostatic and osmotic pressures, changes in the structure of the membrane, which manifest as variations in hydraulic conductivity and the osmotic reflection coefficient for plasma proteins, or disturbances in the lymphatic outflow system. The negative consequence of edema is that an excessive accumulation of interstitial fluid increases the diffusion distance for oxygen and other nutrients, which may compromise cellular metabolism in the edematous tissue. Interstitial edema can also cause the collapse of capillaries, affecting the back flow of blood to the vascular system. This can limit the diffusional removal of potentially toxic byproducts of cellular metabolism causing a disease condition. Edema can also have positive aspects. For example, enhanced flow within the interstitial space can bring more antibodies into the tissues that aid in killing bacteria. Moreover, increased interstitial fluid volume during an inflammatory response may dilute cytotoxic chemicals released by invading microorganisms. In any case, a quantitative study of fluid capillary exchange can be of great interest in understanding edema, and even to understand less studied diseases such as the Systemic Capillary Leak Syndrome (SCLS). Also known as Clarkson's Syndrome, SCLS is a rare disorder of the lymphatic system characterized by acute recurrent attacks, associated with a rapid fall in blood pressure as a result of fluid leak from capillaries. The mortality rate ranges from 30 % to 76% [3] and, although there are less than 500 patients with SCLS reported in the world, the disease may be more frequent than reported in the literature because its diagnosis is often missed or delayed. In addition, since the underlying mechanism is unknown, no efficacious pharmacological treatment has been clearly established. In this context, the stationary model on fluid and protein exchange presented in [5] has

been pioneering as the first quantitative research on these diseases. More specifically, the authors of [5] demonstrated the importance of modelling a heterogeneous microvascular network instead of considering the average of biophysiological parameters, as is common in medical field. The experimental data used in [5] for model calibration are the same ones we consider in this thesis, and are measurements performed in an *in vivo* frog (*Rana pipiens*) mesenteric microvascular network. Frogs have been the traditional animal model for the observation of blood flow in heart, tongue, web, and mesentery [8]. Our goal is to continue this research by expanding the model proposed in [5] to the non-stationary case. Including the temporal evolution of the variables helps the study of relevant phenomena such as, for example, the response to the Atrial natriuretic peptide (ANP), a hormone involved in homeostatic control, for which physiological studies have shown its role in affecting hydraulic conductivity (see for example, [10]). A mathematical model acts like a virtual laboratory where different scenarios can be simulated since all variables are under control and can be tested.

2 | Time dependent mathematical model of fluid and protein transport

The goal of this chapter is to formulate a time-dependent mathematical description of blood flow throughout the vascular capillaries and the exchange of fluid and proteins with the surrounding tissue. Therefore, the model accounts for phenomena occurring along the vessel longitudinal axes and across their permeable walls. In the next sections we derive the set of partial differential equations of this coupled fluid-protein transport model starting from a description of fluid motion and protein transport based on the theory of multicomponent mixtures (see [13], Chapter 8). More specifically, in Section 2.1 we present the geometry of the model, in Section 2.2 we derive its equations starting from the balance equations, in Section 2.3 we reduce the model to a single spatial coordinate, and finally in Section 2.4 we summarize the equations of the model and the physical meaning of each variable.

2.1. Geometry of the model

The first assumption needed to develop a mathematical model is to approximate the geometry of the vessels as straight rigid cylinders of length L and radius R , with constant circular cross-section. Although capillaries are tortuous, this is the best approximation to simplify the problem by introducing a local system of cylindrical coordinates in which r , s and θ are the radial, axial and angular coordinates, with $r \in [0, R)$, $s \in (0, L)$ and $\theta \in [0, 2\pi)$, as shown in Figure 2.1. Then, thanks to the cylindrical coordinates, we can write any vector \underline{x} as $\underline{x} = (r \cos \theta, r \sin \theta, s)$ and we can identify the geometrical space occupied by a vessel as the domain Ω defined as:

$$\Omega = \{\underline{x} \in \mathbb{R}^3 : r \in [0, R), s \in (0, L), \theta \in [0, 2\pi)\}. \quad (2.1)$$

The boundary of Ω , denoted by $\partial\Omega$, is given by the union of the inlet surface Σ_0 , the outlet surface Σ_L and the lateral surface Σ_R , so that we can write $\partial\Omega = \Sigma_0 \cup \Sigma_L \cup \Sigma_R$, where:

$$\Sigma_0 = \{\underline{x} \in \mathbb{R}^3 : r \in [0, R), s = 0, \theta \in [0, 2\pi)\}. \quad (2.2)$$

$$\Sigma_L = \{\underline{x} \in \mathbb{R}^3 : r \in [0, R), s = L, \theta \in [0, 2\pi)\}. \quad (2.3)$$

$$\Sigma_R = \{\underline{x} \in \mathbb{R}^3 : r = R, s \in (0, L), \theta \in [0, 2\pi)\}. \quad (2.4)$$

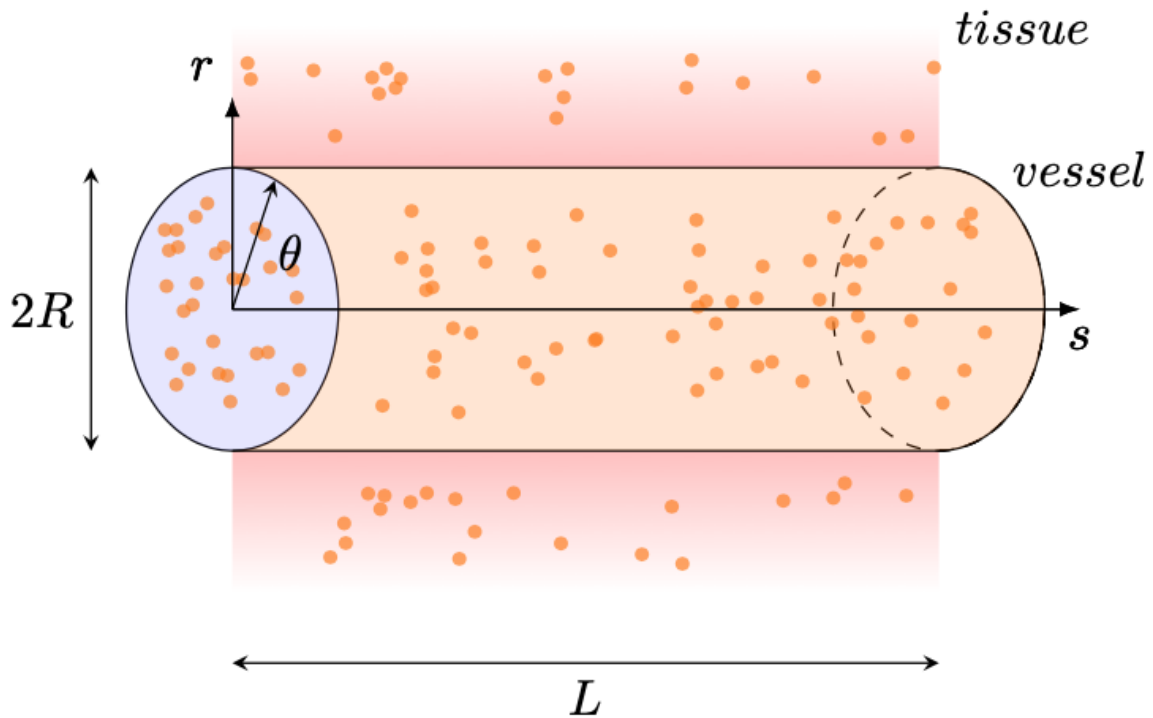


Figure 2.1: Schematic representation of the vessel. The vessel is assumed to be a cylinder of length L and constant circular cross-section of radius R . A local system of cylindrical coordinates is introduced, where r , s and θ denote the radial, axial and angular coordinates, respectively. The model includes fluid (blue shading) and proteins (orange dots), which are transported along the vessel and are exchanged with the tissue (red shading) across the permeable vessel walls (orange shading).

Since these geometric considerations apply to every microvascular capillary in a cellular tissue, the equations we derive in the next sections are extremely general. In order to analyze the fluid and protein exchanges occurring in the entire microvascular network, the caution required is to consider interface conditions between the microvascular capillaries

and different physical dimensions for each vessel, as performed for the stationary model derived in [5]. However, the focus of this thesis is to extend the model to the non-stationary case. Therefore, we limit the study to the single vessel, and computations of the total fluid and protein exchanges across the full network will be neglected at this time. Obviously, in the future, a more comprehensive vascular network non stationary model may be considered.

2.2. Simplification of balance equations

In this section we make some reasonable considerations about the constitutive nature of blood in order to simplify the balance equations of mass and linear momentum. Blood is a complex medium composed by blood cells suspended in blood plasma. Plasma, also referred to as the fluid phase, is mostly water (92% by volume), and contains proteins, glucose, mineral ions, hormones and carbon dioxide. Instead, the blood cell phase consists of red blood cells, white blood cells and platelets. In this work we focus only on water and proteins since they play the major role in the microvascular exchange [14].

The first consideration concerns the fact that the fluid phase and the cellular phase do not mix at the molecular level. As a consequence (see [13], Section 8.2), they are modeled as a heterogeneous mixture so that, after introducing the concept of partial densities, we can consider individual balance equations for each phase. Hence, first of all, we introduce the following volume fractions:

- ϕ_{fp} volume fraction of the fluid phase, defined as the ratio between the volume occupied by the fluid phase and a reference volume in the heterogeneous mixture;
- ϕ_{cp} volume fraction of the cell phase, defined as the ratio between the volume occupied by the blood cell phase and a reference volume in the heterogeneous mixture.

Then, we can define the partial densities of fluid and cell phases as:

$$\rho_{fp} = \phi_{fp} \rho_{fpR}, \quad (2.5a)$$

$$\rho_{cp} = \phi_{cp} \rho_{cpR}, \quad (2.5b)$$

where ρ_{fpR} and ρ_{cpR} indicates the real densities of fluid and cell phase respectively. Now, the application of the mathematical theory of multicomponent mixtures to this two-phase

blood mixture leads to the following system of balance laws for the fluid and cell phases:

$$\frac{\partial \rho_{fp}}{\partial t} + \nabla \cdot (\rho_{fp} \underline{\mathbf{v}}_{fp}) = \beta_{fp} \quad (2.6a)$$

$$\rho_{fp} \frac{\partial \underline{\mathbf{v}}_{fp}}{\partial t} + \rho_{fp} \underline{\mathbf{v}}_{fp} \cdot \nabla \underline{\mathbf{v}}_{fp} = \nabla \cdot \underline{\underline{\mathbf{T}}}_{fp} + \underline{\mathbf{b}}_{fp} \quad (2.6b)$$

$$\underline{\underline{\mathbf{T}}}_{fp} = \underline{\underline{\mathbf{T}}}_{fp}^T, \quad (2.6c)$$

and

$$\frac{\partial \rho_{cp}}{\partial t} + \nabla \cdot (\rho_{cp} \underline{\mathbf{v}}_{cp}) = \beta_{cp} \quad (2.7a)$$

$$\rho_{cp} \frac{\partial \underline{\mathbf{v}}_{cp}}{\partial t} + \rho_{cp} \underline{\mathbf{v}}_{cp} \cdot \nabla \underline{\mathbf{v}}_{cp} = \nabla \cdot \underline{\underline{\mathbf{T}}}_{cp} + \underline{\mathbf{b}}_{cp} \quad (2.7b)$$

$$\underline{\underline{\mathbf{T}}}_{cp} = \underline{\underline{\mathbf{T}}}_{cp}^T. \quad (2.7c)$$

For each phase α , $\alpha = fp$ (fluid phase) or $\alpha = cp$ (cell phase), the first equation in (2.6)-(2.7) is the balance of mass, the second equation is the balance of linear momentum and the third equation is the balance of angular momentum. The variable ρ_α is the partial density of the phase α , $\underline{\mathbf{v}}_\alpha$ is the Eulerian velocity of the phase α , $\underline{\underline{\mathbf{T}}}_\alpha$ is the partial stress tensor of the phase α , β_α is the net production rate of mass per unit volume of the phase α and $\underline{\mathbf{b}}_\alpha$ is the body force per unit volume of the phase α . Systems (2.6)-(2.7) can be solved in the domain Ω once initial and boundary conditions are supplied as well as constitutive laws for β_α , $\underline{\mathbf{b}}_\alpha$ and $\underline{\underline{\mathbf{T}}}_\alpha$. Since our focus is on water and proteins, from now on we consider only the set of partial differential equations in (2.6), which can be simplified by applying the following assumptions:

- **Assumption 1** Water and proteins mix at the molecular level and can be modeled as a homogeneous mixture (see [13], Section 8.1), then:

$$\rho_{fpR} = \rho_w + \rho_{pt}, \quad (2.8a)$$

$$\rho_{fp} = \phi_{fp}(\rho_w + \rho_{pt}), \quad (2.8b)$$

where ρ_w and ρ_{pt} indicate the real densities of water and proteins, respectively.

- **Assumption 2** The fluid phase is a dilute solution of proteins in water. This means that:

$$\frac{\rho_{pt}}{\rho_w} = \epsilon \ll 1, \quad (2.9)$$

but also that proteins do not exchange pressure and friction among each other which implies:

$$\underline{\underline{\mathbf{T}}}_{pt} = 0, \quad (2.10)$$

where $\underline{\underline{T}}_{pt}$ is the partial stress tensor of proteins.

- **Assumption 3** Volumetric forces and volumetric sources of mass are absent. This means that:

$$\underline{b}_{fp} = 0, \beta_{fp} = 0. \quad (2.11)$$

Moreover, regarding the Eulerian velocity of the fluid phase, we can use the Equation (8.49) of [13], which normally applies to homogeneous mixture, to express it as follows:

$$\underline{v}_{fp} = \frac{\rho_w \underline{v}_w + \rho_{pt} \underline{v}_{pt}}{\rho_w + \rho_{pt}}, \quad (2.12)$$

where \underline{v}_w and \underline{v}_{pt} are respectively the velocity of water and protein components. Next, using Equation (2.9) we can write:

$$\underline{v}_{fp} = \frac{\underline{v}_w + \epsilon \underline{v}_{pt}}{1 + \epsilon} = \frac{|\underline{v}_w| \underline{e}_w + \epsilon |\underline{v}_{pt}| \underline{e}_{pt}}{1 + \epsilon} = |\underline{v}_w| \frac{\underline{e}_w + \epsilon \frac{|\underline{v}_{pt}|}{|\underline{v}_w|} \underline{e}_{pt}}{1 + \epsilon}, \quad (2.13)$$

where \underline{e}_w and \underline{e}_{pt} are unit vectors identifying the direction of water and proteins velocity. Finally, under normal conditions, blood flow regime is dominated by transport of proteins which implies that $|\underline{v}_{pt}| \simeq |\underline{v}_w|$. Hence, we get $\epsilon \frac{|\underline{v}_{pt}|}{|\underline{v}_w|} \ll 1$ since epsilon is a very small quantity and we can simplify (2.13) obtaining that the fluid phase velocity is almost equal to the water velocity:

$$\underline{v}_{fp} \simeq \underline{v}_w. \quad (2.14)$$

On the other hand, we can split the Cauchy stress tensor of the fluid phase using the Equation (8.71) of [13] which normally applies to homogeneous mixture expressing it as:

$$\underline{\underline{T}}_{fp} = \underline{\underline{T}}_w - \rho_w \underline{w}_w \otimes \underline{w}_w + \underline{\underline{T}}_{pt} - \rho_{pt} \underline{w}_{pt} \otimes \underline{w}_{pt}, \quad (2.15)$$

where $\underline{\underline{T}}_w$ is the partial stress tensors of water and $\underline{w}_\alpha = \underline{v}_\alpha - \underline{v}_{fp}$ $\alpha = w, pt$. Using into (2.15) relations (2.14) and (2.10), we obtain

$$\underline{\underline{T}}_{fp} = \underline{\underline{T}}_w - \rho_{pt} \underline{w}_{pt} \otimes \underline{w}_{pt}. \quad (2.16)$$

Now, taking into account that fluid advection is negligible, consistently with the fact that

protein transport is dominant in blood flow, we can consider that:

$$\underline{\underline{\mathbf{w}}}_{pt} \otimes \underline{\underline{\mathbf{w}}}_{pt} \simeq 0, \quad (2.17)$$

so that (2.16) becomes:

$$\underline{\underline{\mathbf{T}}}_{fp} = \underline{\underline{\mathbf{T}}}_w. \quad (2.18)$$

Thanks to (2.11),(2.14) and (2.18) the balances of linear and angular momentum in (2.6b)-(2.6c) simplify as:

$$\rho_{fp} \frac{\partial \underline{\mathbf{v}}_w}{\partial t} = \nabla \cdot \underline{\underline{\mathbf{T}}}_w, \quad (2.19a)$$

$$\underline{\mathbf{T}}_w = \underline{\underline{\mathbf{T}}}_w^T. \quad (2.19b)$$

Instead, the fluid phase balance of mass in (2.6a) can be split through relation (2.8b) and (2.12) in two mass balance equations for water and proteins:

$$\frac{\partial \rho_w}{\partial t} + \nabla \cdot (\rho_w \underline{\mathbf{v}}_w) = 0, \quad (2.20a)$$

$$\frac{\partial C}{\partial t} + \nabla \cdot (C \underline{\mathbf{v}}_{pt}) = 0, \quad (2.20b)$$

where protein density ρ_{pt} has been more properly rewritten as concentration C .

The last step is to model water as an incompressible fluid which means that ρ_w is constant and that:

$$\underline{\underline{\mathbf{T}}}_w = -p \underline{\underline{\mathbf{I}}} + 2\mu_w \underline{\underline{\mathbf{D}}}(\underline{\mathbf{v}}_w), \quad (2.21a)$$

$$\underline{\underline{\mathbf{D}}}(\underline{\mathbf{v}}_w) = \frac{1}{2} [\nabla \underline{\mathbf{v}}_w + (\nabla \underline{\mathbf{v}}_w)^T], \quad (2.21b)$$

where p is water pressure (cmH_2O), μ_w is the dynamic viscosity of water ($cmH_2O s$), $\underline{\underline{\mathbf{I}}}$ is the identity tensor and $\underline{\underline{\mathbf{D}}}(\underline{\mathbf{v}}_w)$ is the symmetric gradient of $\underline{\mathbf{v}}_w$, having the physical meaning of strain rate tensor of water (s^{-1}).

Therefore, equations (2.19a) and (2.20a) become:

$$\rho_{fp} \frac{\partial \underline{\mathbf{v}}_w}{\partial t} = -\nabla p + 2\mu_w \Delta \underline{\mathbf{v}}_w, \quad (2.22a)$$

$$\nabla \cdot \underline{\mathbf{v}}_w = 0, \quad (2.22b)$$

where Δ is the Laplace differential operator. Whereas, regarding the protein mass balance equation (2.20b), we further manipulate it as:

$$\frac{\partial C}{\partial t} + \nabla \cdot (C \underline{\mathbf{v}}_w + C \underline{\mathbf{w}}_{pt}) = 0. \quad (2.23)$$

This traditional approach, treated in [13], allows us to introduce the following flux densities:

$$\underline{\mathbf{J}}_{adv} = C \underline{\mathbf{v}}_w \quad (2.24a)$$

$$\underline{\mathbf{J}}_{diff} = C \underline{\mathbf{w}}_{pt} = C(\underline{\mathbf{v}}_{pt} - \underline{\mathbf{v}}_w), \quad (2.24b)$$

where $\underline{\mathbf{J}}_{adv}$ ($g \text{ cm}^{-2} \text{ s}^{-1}$) is the advective flux density of protein concentration whereas $\underline{\mathbf{J}}_{diff}$ ($g \text{ cm}^{-2} \text{ s}^{-1}$) is the diffusive flux density of protein concentration. The latter can be expressed through Fick's law of diffusion as:

$$\underline{\mathbf{J}}_{diff} = -D_{pt} \nabla C, \quad (2.25)$$

where D_{pt} is the diffusion coefficient of the proteins into water ($\text{cm}^2 \text{ s}^{-1}$). Gathering together equations (2.22) and (2.23) we obtain the following simplified model for the water and protein homogeneous mixture:

$$\nabla \cdot \underline{\mathbf{v}}_w = 0, \quad (2.26a)$$

$$\rho_{fp} \frac{\partial \underline{\mathbf{v}}_w}{\partial t} = -\nabla p + 2\mu_w \Delta \underline{\mathbf{v}}_w, \quad (2.26b)$$

$$\frac{\partial C}{\partial t} + \nabla \cdot (C \underline{\mathbf{v}}_w - D_{pt} \nabla C) = 0. \quad (2.26c)$$

The mathematical model (2.26) is a system of nonlinearly coupled partial differential equations with respect to the set of dependent variables $\underline{\mathbf{v}}_w$, p and C . The total number of scalar dependent variables is equal to 5, given by the three scalar components of the velocity $\underline{\mathbf{v}}_w$ and the two scalars p and C . Correspondingly, the number of equations in system (2.26) is equal to 5, three of them given by the linear momentum balance equation (2.26b). Finding a closed-form solution to system (2.26) is a nontrivial problem. Even numerically approximating the problem by treating each capillary as a three-dimensional cylinder as in the figure 2.1 remains a formidable task because it requires a detailed geometrical discretization of the vessel using, for instance, tetrahedral finite elements. For these reasons, a further simplification of the model system (2.26) is performed in the next section where a reduced-order formulation is derived by averaging the equations (2.26) over the circular cross-section of the tube.

2.3. Derivation of the reduced-order model for the water and protein homogeneous mixture

We recall that our interest is in computing the exchange fluxes between the capillaries and the surrounding tissue, rather than in finding the variables values of model (2.26) at each point in the domain. For this reason, we further simplify the mathematical description of the coupled water-proteins model in (2.26) by reducing it to a system of partial differential equations whose the only space variable is the axial coordinate s along the vessel centerline (Figure 2.1). To obtain the reduced order model, we first notice that axial symmetry holds for all involved variables and forcing terms. Referring to the geometry introduced in Section 2.1, this means that all problem unknowns do not depend on the angular coordinate θ so that the variables in (2.26) can be written as:

$$\underline{\mathbf{v}}_w = v_r(r, s, t) \underline{\mathbf{e}}_r + v_s(r, s, t) \underline{\mathbf{e}}_s, \quad (2.27a)$$

$$p = p(r, s, t), \quad (2.27b)$$

$$C = C(r, s, t), \quad (2.27c)$$

where $\underline{\mathbf{e}}_r$ and $\underline{\mathbf{e}}_s$ are unit vectors in the radial and axial directions r and s .

The second consideration is that equations (2.26), valid in the domain Ω , require suitable boundary conditions in order to be solved. The boundary conditions on the inlet surface Σ_0 and on the outlet surface Σ_L can be generic, for example Dirichlet, Neumann or Robin conditions, depending on physiological conditions, or whether the capillary is internal or terminal to the network. They will be placed once the model is reduced. Conversely, the boundary conditions on the lateral surface Σ_R are based on the physiological description of fluid and protein exchanges treated in Chapter 1. More specifically, The Starling Equation (1.2) can be expressed at any point on the lateral surface Σ_R as:

$$\underline{\mathbf{v}}_w \cdot \underline{\mathbf{n}}|_{\Sigma_R} = L_p[(p|_{\Sigma_R} - p_t) - \sigma(\pi|_{\Sigma_R} - \pi_t)], \quad (2.28)$$

where we recall that p and π are respectively the hydrostatic and osmotic pressure inside the capillary, whereas p_t and π_t the hydrostatic and osmotic pressure in the tissue that surrounds the vessel. According to Van't Hoff relation (1.1), the osmotic pressure π is associated with the protein concentration C via a phenomenological relationship:

$$\pi(C) = a_1 C, \quad (2.29)$$

where a_1 is a given constant.

The boundary condition on Σ_R for protein are expressed trough the revisited Fick's law (1.6) as:

$$\underline{\mathbf{J}}_{pt} \cdot \underline{\mathbf{n}}|_{\Sigma_R} = \frac{1-\sigma}{\sigma} P_d (C_t - C|_{\Sigma_R}), \quad (2.30)$$

where

$$\underline{\mathbf{J}}_{pt} = \underline{\mathbf{J}}_{adv} + \underline{\mathbf{J}}_{diff} = C \underline{\mathbf{v}}_w - D_{pt} \nabla C, \quad (2.31)$$

$\underline{\mathbf{J}}_{adv}$ and $\underline{\mathbf{J}}_{diff}$ being the advective and diffusive protein flux densities defined in (2.24a) and (2.25), respectively.

In light of the equations (2.27a),(2.27b) and (2.28), employing the divergence and the Laplace operator in cylindrical coordinates, the mathematical model in equations (2.26a) and (2.26b) for the water component of the mixture for $t \in (0, T)$ reads:

$$\frac{\partial v_s}{\partial s} + \frac{1}{r} \frac{\partial(rv_r)}{\partial r} = 0 \quad r \in (0, R), s \in (0, L) \quad (2.32a)$$

$$\rho_{fp} \frac{\partial v_r}{\partial t} = - \frac{\partial p}{\partial r} + \mu_w \left(\frac{\partial^2 v_r}{\partial r^2} + \frac{1}{r} \frac{\partial v_r}{\partial r} + \frac{\partial^s v_r}{\partial s^s} \right) \quad r \in (0, R), s \in (0, L), \quad (2.32b)$$

$$\rho_{fp} \frac{\partial v_s}{\partial t} = - \frac{\partial p}{\partial s} + \mu_w \left(\frac{\partial^2 v_s}{\partial r^2} + \frac{1}{r} \frac{\partial v_s}{\partial r} + \frac{\partial^s v_s}{\partial s^s} \right) \quad r \in (0, R), s \in (0, L), \quad (2.32c)$$

$$v_r = L_p[(p - p_t) - \sigma(\pi - \pi_t)] \quad r = R, s \in (0, L). \quad (2.32d)$$

On the other hand, as far as the mathematical model for the protein component is concerned, thanks to relation (2.31) equation (2.26c) can be written as:

$$\frac{\partial C}{\partial t} + \nabla \cdot \underline{\mathbf{J}}_{pt} = 0. \quad (2.33)$$

Now, considering the assumption of axial symmetry for protein flux as well, we obtain that:

$$\underline{\mathbf{J}}_{pt} = J_r(r, s, t) \underline{\mathbf{e}}_r + J_s(r, s, t) \underline{\mathbf{e}}_s, \quad (2.34)$$

where J_r and J_s are respectively the radial and axial component of the protein flux $\underline{\mathbf{J}}_{pt}$. Therefore, computing the divergence in cylindrical coordinates and joining the boundary condition (2.30) to equation (2.33), the mathematical model for the protein component

of the mixture for $t \in (0, T)$ reads:

$$\frac{\partial C}{\partial t} + \frac{\partial J_s}{\partial s} + \frac{1}{r} \frac{\partial(r J_r)}{\partial r} = 0, \quad r \in (0, R), s \in (0, L), \quad (2.35a)$$

$$J_r = Cv_r - D_{pt} \frac{\partial C}{\partial r}, \quad r \in (0, R), s \in (0, L), \quad (2.35b)$$

$$J_s = Cv_s - D_{pt} \frac{\partial C}{\partial s}, \quad r \in (0, R), s \in (0, L), \quad (2.35c)$$

$$\sigma J_r + (1 - \sigma) P_d(C_t - C) = 0, \quad r = R, s \in (0, L). \quad (2.35d)$$

Now we are ready to derive separately for water and proteins a reduced model dependent only on the axial coordinate s . The procedure consists of integrating the equations over the tube cross-section. Starting from water, integrating (2.32a) yields:

$$\int_0^{2\pi} \int_0^R \frac{\partial v_s}{\partial s} r dr d\theta + \int_0^{2\pi} \int_0^R \frac{1}{r} \frac{\partial(rv_r)}{\partial r} r dr d\theta = 0. \quad (2.36)$$

Introducing the axial volumetric flow rate q_f ($cm^3 s^{-1}$) of the fluid along the vessel defined as:

$$q_f(s, t) := \int_0^{2\pi} \int_0^R v_s(r, s, t) r dr d\theta, \quad (2.37)$$

and computing the second integral of equation (2.36) we obtain:

$$\frac{\partial q_f(s, t)}{\partial s} + 2\pi R v_r(R, s, t). \quad (2.38)$$

Then, using the lateral boundary condition (2.32d) into (2.38) yields the averaged mass balance equation:

$$\frac{\partial q_f(s, t)}{\partial s} + 2\pi R L_p[(p(s, t) - p_t(s, t)) - \sigma(\pi(s, t) - \pi_t(s, t))]. \quad (2.39)$$

At this stage, a further assumption to consider is that the radial component v_r of water velocity can be neglected inside the vessel compared to the axial component v_s , which means that $v_r(r, s, t) = 0$ for $r \in (0, R), s \in (0, L)$ and thus, from equation (2.32b), we deduce that pressure is constant over each cross-section of the vessel:

$$\frac{\partial p(r, s, t)}{\partial r} = 0 \implies p = p(s, t). \quad (2.40)$$

That's why we wrote equation (2.39) without specifying that the pressure is evaluated at $r=R$.

In order to reduce equation (2.32c) we write the axial velocity as $v_s = v_s(r, s, t) =$

$f(r)V(s, t)$, where $V(s, t)$ is the average value of v_s at time t over the vessel cross section located at s and $f(r)$ is a shape function describing the velocity profile over the cross section. As a basic requirement, any choice for $f(r)$ must satisfy the following condition:

$$\int_0^{2\pi} \int_0^R f(r)r dr d\theta = \pi R^2, \quad (2.41)$$

so that the axial volumetric flow rate q_f can be expressed as:

$$q_f(s, t) = \pi R^2 V(s, t). \quad (2.42)$$

We use the following Generalized Hagen-Poiseuille shape function in the radial direction:

$$f(r) = \frac{\gamma + 2}{\gamma} \left[1 - \left(\frac{r}{R} \right)^\gamma \right], \quad r \in [0, R] \quad (2.43)$$

where $\gamma > 0$ denotes the so-called steepness parameter. The classic Hagen-Poiseuille expression for a parabolic velocity profile is obtained by setting $\gamma = 2$ in (2.43).

Integrating (2.32c) over the capillary cross-section and using (2.40) and (2.42), we get:

$$\begin{aligned} \rho_{fp} \frac{\partial V(s, t)}{\partial t} \int_0^{2\pi} \int_0^R f(r)r dr d\theta &= -\pi R^2 \frac{\partial p(s, t)}{\partial s} \\ &+ \mu_w V(s) \int_0^{2\pi} \int_0^R \frac{d^2 f(r)}{dr^2} r dr d\theta + \mu_w V(s) \int_0^{2\pi} \int_0^R \frac{1}{r} \frac{df(r)}{dr} r dr d\theta \\ &+ \mu_w \frac{\partial^2 V(s, t)}{\partial s^2} \int_0^{2\pi} \int_0^R f(r)r dr d\theta = 0. \end{aligned} \quad (2.44)$$

Simple algebra yields:

$$\int_0^{2\pi} \int_0^R \frac{d^2 f(r)}{dr^2} r dr d\theta = -2\pi \frac{(\gamma + 2)(\gamma - 1)}{\gamma} \quad (2.45a)$$

$$\int_0^{2\pi} \int_0^R \frac{df(r)}{dr} r dr d\theta = -2\pi \frac{(\gamma + 2)}{\gamma}. \quad (2.45b)$$

Using equations (2.41),(2.42) and (2.45) into (2.44) yields the following reduced-order axial momentum balance for the water component of the mixture:

$$\rho_{fp} \frac{\partial q_f(s, t)}{\partial t} = -\pi R^2 \frac{\partial p(s, t)}{\partial s} - 2\mu_w \frac{\gamma + 2}{R^2} q_f(s, t) + \mu_w \frac{\partial^2 q_f(s, t)}{\partial s^2}. \quad (2.46)$$

Finally, adding the simplifying assumption that the axial volumetric flow rate $q_f(s, t)$ depends linearly on s , we aggregate the equations (2.39) and (2.46) obtaining the following

reduced-order model for water component of the two-phase mixture:

$$\frac{\partial q_f(s, t)}{\partial s} + 2\pi R L_p[(p(s, t) - p_t(s, t)) - \sigma(\pi(s, t) - \pi_t(s, t))], \quad (2.47a)$$

$$\rho_{fp} \frac{\partial q_f(s, t)}{\partial t} = -\pi R^2 \frac{\partial p(s, t)}{\partial s} - 2\mu_w \frac{\gamma + 2}{R^2} q_f(s, t), \quad (2.47b)$$

holding for $s \in (0, L)$ and $t \in (0, T)$.

The procedure to derive the reduced model for proteins is analogous. We integrate equation (2.35a) over the vessel cross-section to get:

$$\int_0^{2\pi} \int_0^R \frac{\partial C}{\partial t} r dr d\theta + \int_0^{2\pi} \int_0^R \frac{\partial J_s}{\partial s} r dr d\theta + \int_0^{2\pi} \int_0^R \frac{1}{r} \frac{\partial(r J_r)}{\partial r} r dr d\theta. \quad (2.48)$$

Then, using equation (2.35c) to express J_s and exploiting the surface boundary condition (2.35d) yields:

$$\begin{aligned} & \int_0^R \frac{\partial C(r, s, t)}{\partial t} r dr + \int_0^R \frac{\partial}{\partial s} \left(C(r, s, t) v_s(r, s, t) - D_{pt} \frac{\partial C(r, s, t)}{\partial s} \right) r dr \\ & + R \frac{1 - \sigma}{\sigma} P_d(C(R, s, t) - C_t(R, s, t)) = 0. \end{aligned} \quad (2.49)$$

Since the model is focused on membrane exchanges between microvascular capillaries and interstitium, without losing valuable information, we can assume that concentration is constant over each cross-section of the vessel, and, consequently, depends only on the axial coordinate s and on the time t :

$$C(r, s, t) = C(s, t). \quad (2.50)$$

Therefore, equations (2.49) becomes:

$$\begin{aligned} & \frac{\partial C(s, t)}{\partial t} \int_0^R r dr + \frac{\partial}{\partial s} \left(C(s, t) V(s, t) \int_0^R f(r) r dr - D_{pt} \frac{\partial C(s, t)}{\partial s} \int_0^R r dr \right) \\ & + R \frac{1 - \sigma}{\sigma} P_d(C(s, t) - C_t(s, t)) = 0. \end{aligned} \quad (2.51)$$

Noting that:

$$\int_0^R r dr = \int_0^R f(r) r dr = \frac{R^2}{2}, \quad (2.52)$$

we can re-write equation (2.51) as:

$$\begin{aligned} & \frac{\partial C(s, t)}{\partial t} \frac{R^2}{2} + \frac{\partial}{\partial s} \left(C(s, t) V(s, t) \frac{R^2}{2} - D_{pt} \frac{\partial C(s, t)}{\partial s} \frac{R^2}{2} \right) \\ & + R \frac{1-\sigma}{\sigma} P_d (C(s, t) - C(s, t)) = 0. \end{aligned} \quad (2.53)$$

Finally, using equation (2.42), we obtain the following final form of the reduced-order model for protein component of the two-phase mixture:

$$\pi R^2 \frac{\partial C(s, t)}{\partial t} + \frac{\partial q_p(s, t)}{\partial s} + 2\pi R \frac{1-\sigma}{\sigma} P_d (C(s, t) - C(s, t)) = 0, \quad (2.54a)$$

$$q_p(s, t) = C(s, t) q_f(s, t) - \pi R^2 D_{pt} \frac{\partial C(s, t)}{\partial s}, \quad (2.54b)$$

holding for $s \in (0, L)$ and $t \in (0, T)$. The quantity $q_p(s, t)$ represents the mass rate of protein ($g s^{-1}$) at each point $s \in (0, L)$ and time $t \in (0, T)$ along the axial direction of vessel T.

2.4. Coupled model for the transport of fluid and proteins

The equations (2.47) and (2.54) can be combined as follows:

$$\frac{\partial q_f(s, t)}{\partial s} + 2\pi R L_p [(p(s, t) - p_t(s, t)) - \sigma(\pi(s, t) - \pi_t(s, t))], \quad (2.55a)$$

$$\rho_{fp} \frac{\partial q_f(s, t)}{\partial t} = -\pi R^2 \frac{\partial p(s, t)}{\partial s} - 2\mu_w \frac{\gamma+2}{R^2} q_f(s, t), \quad (2.55b)$$

$$\pi R^2 \frac{\partial C(s, t)}{\partial t} + \frac{\partial q_p(s, t)}{\partial s} + 2\pi R \frac{1-\sigma}{\sigma} P_d (C(s, t) - C(s, t)) = 0, \quad (2.55c)$$

$$q_p(s, t) = C(s, t) q_f(s, t) - \pi R^2 D_{pt} \frac{\partial C(s, t)}{\partial s}. \quad (2.55d)$$

From the mathematical viewpoint, the model in (2.55) is a first-order system of nonlinearly coupled partial differential equations whose solution consists of finding the four dependent variables $q_f = q_f(s, t)$, $p = p(s, t)$, $q_p = q_p(s, t)$ and $C = C(s, t)$ for $s \in (0, L)$ and $t \in (0, T)$, provided the initial conditions, as well as suitable expressions are given for the data in the tissue $p_t = p_t(s, t)$, $\pi_t = \pi_t(s, t)$ and $C_t = C_t(s, t)$, and suitable boundary conditions are provided at the inlet and outlet surfaces, remembering that the relationship between osmotic pressures and protein concentrations is given by (2.29). Moreover, we define additional quantities of physiological interest that will be used to quantify fluid

and protein exchanges. The specific lateral volumetric flow rate of fluid $j_f(s, t)$ ($\text{cm}^2 \text{s}^{-1}$) is defined as:

$$j_f(s, t) := 2\pi R L_p [(p(s, t) - p_t(s, t)) - \sigma(\pi(s, t) - \pi_t(s, t))]. \quad (2.56)$$

Description	Symbols	Unit
<i>Quantities that vary within the vessel</i>		
Axial coordinate along the length	s	[cm]
Time	t	[s]
Hydrostatic pressure	$p(s, t)$	[cmH ₂ O]
Protein concentration	$C(s, t)$	[g cm ⁻³]
Osmotic pressure	$\pi(s, t)$	[cmH ₂ O]
Axial volumetric flow rate	$q_f(s, t)$	[cm ³ s ⁻¹]
Specific lateral volumetric flow rate	$j_f(s, t)$	[cm ² s ⁻¹]
Axial mass flow rate	$q_p(s, t)$	[g s ⁻¹]
Specific lateral mass flow rate	$j_p(s, t)$	[cm ⁻¹ g s ⁻¹]
<i>Quantities that are constant</i>		
Radius of the vessel	R	[cm]
Length of the vessel	L	[cm]
Partial density of the fluid phase	ρ_{fp}	[g cm ⁻³]
Water dynamic viscosity	μ_w	[cmH ₂ O s]
Hydraulic conductivity of the membrane	L_p	[cm s ⁻¹ cmH ₂ O ⁻¹]
Protein reflection coefficient of the membrane	σ	[\cdot]
Solute permeability of the membrane	P_d	[cm s ⁻¹]
Protein diffusion coefficient	D_{pt}	[cm ² s ⁻¹]
Shape factor	γ	[\cdot]
Lateral volumetric flow rate	J_f	[cm ³ s ⁻¹]
Lateral mass flow rate	J_p	[g s ⁻¹]

Table 2.1: Summary of model variables and parameters. The table distinguishes among quantities that vary within the vessel or are constant.

Relation (2.56) agrees with the Starling equation (1.2) since the total lateral volumetric flow rate of fluid J_f ($\text{cm}^3 \text{s}^{-1}$) is computed as the integral of j_f over the length of

the vessel:

$$J_f(t) = \int_0^L j_f(s, t) ds. \quad (2.57)$$

We emphasise that J_f represents the fluid volume exchanged through the whole lateral surface of the vessel per unit time at time $t \in (0, T)$.

In a similar manner, , considering the protein variables, we define the specific lateral mass flow rate $j_p(s, t)$ ($cm^{-1} g s^{-1}$) as:

$$j_p(s, t) := 2\pi R \frac{1 - \sigma}{\sigma} P_d(C(s, t) - C_t(s, t)). \quad (2.58)$$

This variable is related to Fick's law (1.6) through the total lateral mass flow rate of proteins J_p ($g s^{-1}$) computed as:

$$J_p(t) = \int_0^L j_p(s, t) ds. \quad (2.59)$$

We highlight that J_p represents the mass of proteins exchanged through the whole lateral surface of the vessel per unit time at time $t \in (0, T)$. In view of these considerations, the coupled model for the transport of fluid and proteins in equations (2.55) can be summarized in the following system of equations:

$$\left\{ \begin{array}{l} \frac{\partial q_f}{\partial s} + j_f = 0, \\ \frac{\rho_{fp}}{\pi R^2} \frac{\partial q_f}{\partial t} = -\frac{\partial p}{\partial s} - \frac{2\mu_w(\gamma + 2)}{\pi R^4} q_f, \end{array} \right. \quad s \in (0, L), t \in (0, T), \quad (2.60a)$$

$$\left\{ \begin{array}{l} \frac{\partial C}{\partial t} + \frac{1}{\pi R^2} \frac{\partial q_p}{\partial s} + \frac{j_p}{\pi R^2} = 0, \\ q_p = C q_f - \pi R^2 D \frac{\partial C}{\partial s}, \end{array} \right. \quad s \in (0, L), t \in (0, T), \quad (2.60c)$$

$$\left\{ \begin{array}{l} j_f = 2\pi R L_p [(p - p_t) - \sigma(\pi - \pi_t)], \\ j_p = 2\pi R \frac{1 - \sigma}{\sigma} P_d(C - C_t), \end{array} \right. \quad s \in (0, L), t \in (0, T), \quad (2.60e)$$

$$\left\{ \begin{array}{l} B.C. \\ I.C. \end{array} \right. \quad s = 0, s = L, t \in (0, T), \quad (2.60g)$$

$$\left\{ \begin{array}{l} I.C. \end{array} \right. \quad s \in (0, L), t = 0. \quad (2.60h)$$

For ease of reference, the notation and parameters characterising the reduced-order model are listed in Table 2.1 together with a description of the physical meaning of the symbols and its units. A final remark is required concerning the protein reflection coefficient σ . This parameter, already discussed in Chapter 1, indicates the likelihood that a protein molecule approaching a pore in the membrane is reflected back from the pore and retained

in the vascular system. The basal value of sigma is 0.8. As will be shown in Chapter 6, which illustrates the physiological results, this value makes the amount of protein moving across the membrane negligible compared to the concentration of protein within the vascular space. As a consequence, protein flux does not affect osmotic pressure π under nonpathological conditions. This outcome is not true under conditions where the reflection coefficient σ is closer to 0, as would occur in inflammation, sepsis, or vascular remodelling. In these conditions, protein flux into the tissue could induce a gradient in osmotic pressure and both fluid and protein can accumulate in the tissue, causing the interstitial edema. Special mention needs to be made of the limiting case where $\sigma = 0$. As described in Chapter 1 this case corresponds to the condition where all solute molecules pass through the membrane and osmotic pressure does not have any effect on fluid filtration. In the model (2.60), the case $\sigma = 0$ is not taken into account since the reflection coefficient σ appears at the denominator in equation (2.60f). In order to consider this limiting case, we need to express j_p though relation (2.60f) in equation (2.60c) and multiplying the latter by σ . This procedure yields:

$$\frac{\partial C}{\partial t}\sigma + \frac{1}{\pi R^2} \frac{\partial q_p}{\partial s} \sigma + 2\pi R(1 - \sigma)P_d(C - C_t) = 0. \quad (2.61)$$

Taking equation (2.61) to the limit case $\sigma \rightarrow 0$ gives the result that the concentration in the vascular space is forced to be equal to the concentration in the tissue:

$$C = C_t. \quad (2.62)$$

Moreover, since the phenomenological relationship (2.29) holds for the osmotic pressure π , also the specific lateral volumetric flow rate j_f simplifies as:

$$j_f = 2\pi R L_p(p - p_t). \quad (2.63)$$

Therefore, when $\sigma = 0$, the model described in equations (2.60) is reduced to the case where no protein exchange occurs and only fluid variables play a role of interest.

3 | Energy of the model

In this chapter we derive the balance of energy starting from the reduced model for fluid and protein transport and exchange described in equations (2.60). Learning about the energy evolution of the problem certainly enables a greater understanding of the physical phenomenon, allowing for example the identification of dissipative and forcing variables. Furthermore, the calculation of the energy balance at the continuous level is the first step for the purpose of computing the numerical energy in Chapter 5, once the problem is solved using fixed point iterations. This energy is very relevant because, in the absence of forcing terms, it supplies a stability estimate for the numerical problem, since its decrease over time can be considered as a necessary condition for the convergence of the method. In the next section we show the mathematical steps to derive the energy balance equation.

3.1. Derivation of the energy balance

Starting from the equations in (2.60), the goal of this section is to formulate an energy identity of the form:

$$\frac{d\mathcal{E}}{dt} + \mathcal{D} = \mathcal{F}, \quad (3.1)$$

where \mathcal{E} represents the energy of the problem, whereas \mathcal{D} and \mathcal{F} denote the dissipative and forcing terms, respectively.

For ease of reference, we report again the equations (2.60) of the model for fluid and

protein derived in Chapter 2:

$$\begin{cases} \frac{\partial q_f}{\partial s} + j_f = 0, & s \in (0, L), t \in (0, T), \\ \frac{\rho}{\pi R^2} \frac{\partial q_f}{\partial t} = -\frac{\partial p}{\partial s} - \alpha q_f, & s \in (0, L), t \in (0, T), \end{cases} \quad (3.2a)$$

$$\begin{cases} \frac{\partial C}{\partial t} + \frac{1}{\pi R^2} \frac{\partial q_p}{\partial s} + \frac{j_p}{\pi R^2} = 0, & s \in (0, L), t \in (0, T), \\ q_p = C q_f - \pi R^2 D \frac{\partial C}{\partial s}, & s \in (0, L), t \in (0, T), \end{cases} \quad (3.2c)$$

$$\begin{cases} j_f = 2\pi R L_p [(p - p_t) - \sigma(\pi - \pi_t)], & s \in (0, L), t \in (0, T), \\ j_p = 2\pi R \frac{1 - \sigma}{\sigma} P_d (C - C_t), & s \in (0, L), t \in (0, T), \end{cases} \quad (3.2e)$$

$$\begin{cases} & s \in (0, L), t \in (0, T), \\ & s \in (0, L), t \in (0, T), \end{cases} \quad (3.2f)$$

where for sake of simplicity we denote by ρ the partial density of the fluid phase and α the last coefficient in equation (2.60b), so that $\alpha := \frac{2\mu_w(\gamma+2)}{\pi R^4}$. We also introduce the following new dependent variable:

$$w := \frac{q_f}{\pi R^2} - \frac{D}{C} \frac{\partial C}{\partial s}. \quad (3.3)$$

From the physical point of view w has the units of velocity ($cm s^{-1}$) and, since equation (3.2d) implies that $\frac{q_p}{\pi R^2} = Cw$, it allows us to rewrite equation (3.2c) as follows:

$$\frac{\partial C}{\partial t} + \frac{\partial(Cw)}{\partial s} + \frac{j_p}{\pi R^2} = 0. \quad (3.4)$$

We are now in the position to apply the standard approach to derive the energy balance equation which consists of writing the integral form of the problem equations in (3.2). In particular, we multiply the first two equations of (3.2) and equation (3.4) by a test function as follows:

$$\int_0^L \frac{\partial q_f}{\partial s} \xi ds = - \int_0^L j_f \xi ds, \quad (3.5a)$$

$$\int_0^L \frac{\rho}{\pi R^2} \frac{\partial q_f}{\partial t} \psi ds = - \int_0^L \frac{\partial p}{\partial s} \psi ds - \int_0^L \alpha q_f \psi ds, \quad (3.5b)$$

$$\int_0^L \frac{\partial C}{\partial t} \phi ds + \int_0^L \frac{\partial(Cw)}{\partial s} \phi ds + \int_0^L \frac{j_p}{\pi R^2} \phi ds = 0. \quad (3.5c)$$

In order to get the physical units of time derivative of energy from the left hand side term in equation (3.5b), we choose $\psi = q_f$, so that equation (3.5b) becomes:

$$\int_0^L \frac{\rho}{\pi R^2} \frac{\partial q_f}{\partial t} q_f ds = - \int_0^L \frac{\partial p}{\partial s} q_f ds - \int_0^L \alpha q_f^2 ds. \quad (3.6)$$

Moving the time derivative outside the integral and differentiating the first term on the right hand side yields:

$$\frac{d}{dt} \left[\frac{1}{2} \frac{\rho}{\pi R^2} \int_0^L q_f^2 ds \right] = - \int_0^L \frac{\partial(p q_f)}{\partial s} ds + \int_0^L \frac{\partial q_f}{\partial s} p ds - \int_0^L \alpha q_f^2 ds. \quad (3.7)$$

Then, we can identify the first term that contributes to the energy of the problem and define:

$$\mathcal{E}_1 := \frac{1}{2} \frac{\rho}{\pi R^2} \int_0^L q_f^2 ds, \quad (3.8)$$

whose units ($g \text{ cm}^2 \text{ s}^{-1}$) are in agreement with those of energy.

Moreover, we can classify the boundary conditions dependent terms and the nonnegative ones of equation (3.7) as forcing and dissipative terms, respectively:

$$\mathcal{F}_1 := - \int_0^L \frac{\partial(p q_f)}{\partial s} ds, \quad (3.9a)$$

$$\mathcal{D}_1 := \int_0^L \alpha q_f^2 ds. \quad (3.9b)$$

In this case dissipation is due to fluid movement and, as expected, it is proportional to fluid viscosity, recalling that the expression for alpha is $\alpha = \frac{2\mu_w(\gamma+2)}{\pi R^4}$.

Instead, to handle the third term of equation (3.7), we choose $\xi = p$ in equation (3.5a) which becomes:

$$\int_0^L \frac{\partial q_f}{\partial s} p ds = - \int_0^L j_f p ds. \quad (3.10)$$

Substituting relations (3.8),(3.9) and (3.10) into equation (3.7) yields:

$$\frac{d\mathcal{E}_1}{dt} + \mathcal{D}_1 = \mathcal{F}_1 - \int_0^L j_f p ds. \quad (3.11)$$

On the other hand, to deal with the protein integral equation (3.5c), we need to introduce a chemical potential. We consider the potential adopted in [16] and defined as:

$$\mu := K_B T \ln \left(\frac{C}{C_{ref}} \right), \quad (3.12)$$

3 | Energy of the model

where K_B is the Boltzmann constant ($J K^{-1}$), T is the temperature (K) and C_{ref} is a reference concentration ($g cm^{-3}$). Definition (3.12) implies the two following relations:

$$\frac{\partial \mu}{\partial s} = K_B T \frac{1}{C} \frac{\partial C}{\partial s}, \quad (3.13a)$$

$$\frac{\partial \mu}{\partial t} = K_B T \frac{1}{C} \frac{\partial C}{\partial t}. \quad (3.13b)$$

Let us now choose the test function ϕ in equation (3.5c) proportional to the chemical potential μ , $\phi = \lambda \mu$, so that equation (3.5c) becomes:

$$\int_0^L \lambda \frac{\partial C}{\partial t} \mu ds + \int_0^L \lambda \frac{\partial(Cw)}{\partial s} \mu ds + \int_0^L \lambda \frac{j_p}{\pi R^2} \mu ds = 0. \quad (3.14)$$

Thus, differentiating by parts the second term, we obtain:

$$\int_0^L \lambda \frac{\partial C}{\partial t} \mu ds + \int_0^L \lambda \frac{\partial(Cw\mu)}{\partial s} ds - \int_0^L \lambda C w \frac{\partial \mu}{\partial s} ds + \int_0^L \lambda \frac{j_p}{\pi R^2} \mu ds = 0. \quad (3.15)$$

The first term of equation (3.15) is the only one that contains the time derivative, thus it forms the other contribution to the time derivative of the energy. More specifically, we can differentiate it as:

$$\int_0^L \lambda \frac{\partial C}{\partial t} \mu ds = \int_0^L \lambda \frac{\partial(C\mu)}{\partial t} ds - \int_0^L \lambda C \frac{\partial \mu}{\partial t} ds. \quad (3.16)$$

Using relation (3.13b) and taking the time derivative out of the integral, we get:

$$\int_0^L \lambda \frac{\partial C}{\partial t} \mu ds = \lambda \left[\int_0^L \left(\frac{\partial(C\mu)}{\partial t} - K_B T \frac{\partial C}{\partial t} \right) ds \right] = \frac{d}{dt} \left[\lambda \int_0^L (C\mu - K_B T C) ds \right]. \quad (3.17)$$

We define the amount of energy due to protein as:

$$\mathcal{E}_2 := \lambda \int_0^L (C\mu - K_B T C) ds = \lambda K_B T \int_0^L C \left(\ln \left(\frac{C}{C_{ref}} \right) - 1 \right) ds, \quad (3.18)$$

where in the last expression we substituted the definition of chemical potential (3.12). The second term in (3.15) depends only on the boundary conditions and thus contributes to the forcing term in the right-hand side of equation (3.1):

$$\mathcal{F}_2 := - \int_0^L \lambda \frac{\partial(Cw\mu)}{\partial s} ds. \quad (3.19)$$

The third term of equation (3.15) is handled as follows:

$$\begin{aligned} - \int_0^L \lambda C w \frac{\partial \mu}{\partial s} ds &= - \int_0^L \lambda C \frac{q_f}{\pi R^2} \frac{\partial \mu}{\partial s} ds + \int_0^L \lambda D \frac{\partial C}{\partial s} \frac{\partial \mu}{\partial s} ds \\ &= - \frac{\lambda K_B T}{\pi R^2} \int_0^L q_f \frac{\partial C}{\partial s} ds + \frac{\lambda D}{K_B T} \int_0^L C \left(\frac{\partial \mu}{\partial s} \right)^2 ds. \end{aligned} \quad (3.20)$$

In the first step of equation (3.20) we used definition (5.5) for w , while in the second step we used the relation (3.13a). Now we notice that the last term in equation (3.20) is nonnegative, so it contributes to the dissipation:

$$\mathcal{D}_2 := \frac{\lambda D}{K_B T} \int_0^L C \left(\frac{\partial \mu}{\partial s} \right)^2 ds. \quad (3.21)$$

In this case dissipation is caused by proteins, proportional to their concentration and diffusion coefficient. The other term in equation (3.20) can be differentiated by parts:

$$-\frac{\lambda K_B T}{\pi R^2} \int_0^L q_f \frac{\partial C}{\partial s} ds = -\frac{\lambda K_B T}{\pi R^2} \int_0^L \frac{\partial(C q_f)}{\partial s} ds + \frac{\lambda K_B T}{\pi R^2} \int_0^L C \frac{\partial q_f}{\partial s} ds \quad (3.22)$$

The first term derived in equation (3.22) depends only on boundary conditions, thus it is taken to the right hand-side of equation (3.15) contributing to the forces:

$$\mathcal{F}_3 := \frac{\lambda K_B T}{\pi R^2} \int_0^L \frac{\partial(C q_f)}{\partial s} ds. \quad (3.23)$$

For the second term derived in equation (3.22) we use the equation (3.2a) to obtain:

$$\frac{\lambda K_B T}{\pi R^2} \int_0^L C \frac{\partial q_f}{\partial s} ds = -\frac{\lambda K_B T}{\pi R^2} \int_0^L C j_f ds. \quad (3.24)$$

Finally, in light of the performed mathematical steps, considering relations (3.18),(3.19),(3.21), (3.23) and (3.24), we can write equation (3.15) as:

$$\frac{d\mathcal{E}_2}{dt} + \mathcal{D}_2 = \mathcal{F}_2 + \mathcal{F}_3 + \frac{\lambda K_B T}{\pi R^2} \int_0^L C j_f ds - \int_0^L \lambda \frac{j_p}{\pi R^2} \mu ds. \quad (3.25)$$

The combination of equations (3.11) and (3.25) leads to the following equation, which is a first form of energy balance of the full problem:

$$\begin{aligned} \frac{d}{dt}(\mathcal{E}_1 + \mathcal{E}_2) + \mathcal{D}_1 + \mathcal{D}_2 &= \mathcal{F}_1 + \mathcal{F}_2 + \mathcal{F}_3 \\ - \int_0^L p j_f ds + \frac{\lambda K_B T}{\pi R^2} \int_0^L C j_f ds - \int_0^L \lambda \frac{j_p}{\pi R^2} \mu ds \end{aligned} \quad (3.26)$$

To identify the role of the last three terms in equation (3.26), we replace into (3.26) the expressions (3.2e) for j_f and (3.2f) for j_p , of which we provide a simplified form below, where the values of the hydrostatic pressure p_t , the osmotic pressure π_t and the protein concentration C_t in the tissue outside of the vessel are assumed to be equal to zero, according to the specific experimental conditions adopted in [5] for the stationary model:

$$j_f = 2\pi R L_p (p - \sigma \pi), \quad (3.27)$$

$$j_p = 2\pi R \frac{1-\sigma}{\sigma} P_d C. \quad (3.28)$$

Therefore, the last three terms in (3.26) become:

$$\begin{aligned} - \int_0^L p j_f ds + \frac{\lambda K_B T}{\pi R^2} \int_0^L C j_f ds - \int_0^L \lambda \frac{j_p}{\pi R^2} \mu ds &= \\ - \int_0^L 2\pi R L_p \left(p - \frac{\lambda K_B T}{\pi R^2} C \right) (p - \sigma \pi) ds - \int_0^L \frac{2\lambda}{R} \frac{1-\sigma}{\sigma} P_d C \mu ds &= \\ - \int_0^L 2\pi R L_p \left(p - \frac{\lambda K_B T}{\pi R^2} C \right) (p - \sigma a_1 C) ds - \int_0^L \frac{2\lambda}{R} \frac{1-\sigma}{\sigma} P_d C \mu ds, \end{aligned} \quad (3.29)$$

where in the last step we used expression (2.29) for the osmotic pressure π . For the purpose of having nonnegative values inside the integrals so that we can consider the terms in equation (3.29) as dissipation at the right-hand side, we assume λ , the constant multiplying the chemical potential μ in the test function ϕ , equal to $\frac{\sigma a_1 \pi R^2}{K_B T}$. Moreover, we require the chemical potential μ to be nonnegative assuming that $C \geq C_{ref}$. In view of these considerations, the quantities in (3.29) form a dissipative term due to the exchange of fluid and protein across the lateral surface:

$$\mathcal{D}_{lat} = 2\pi R L_p \int_0^L (p - \sigma a_1 C)^2 ds + \frac{2a_1 \pi R}{K_B T} (1 - \sigma) P_d \int_0^L C \mu ds. \quad (3.30)$$

Finally, equation (3.26) becomes:

$$\frac{d\mathcal{E}}{dt} + \mathcal{D} + \mathcal{D}_{lat} = \mathcal{F}. \quad (3.31)$$

In conclusion, the energy, dissipative and forcing quantities have the following expressions:

$$\mathcal{E} = \mathcal{E}_1 + \mathcal{E}_2 = \frac{1}{2} \frac{\rho}{\pi R^2} \int_0^L q_f^2 ds + \lambda K_B T \int_0^L C \left(\ln \left(\frac{C}{C_{ref}} \right) - 1 \right) ds, \quad (3.32a)$$

$$\mathcal{D} = \mathcal{D}_1 + \mathcal{D}_2 = \int_0^L \alpha q_f^2 ds + \frac{\lambda D}{K_B T} \int_0^L C \left(\frac{\partial \mu}{\partial s} \right)^2 ds, \quad (3.32b)$$

$$\mathcal{D}_{lat} = 2\pi R L_p \int_0^L (p - \sigma a_1 C)^2 ds + \frac{2a_1 \pi R}{K_B T} (1 - \sigma) P_d \int_0^L C \mu ds, \quad (3.32c)$$

$$\begin{aligned} \mathcal{F} = \mathcal{F}_1 + \mathcal{F}_2 + \mathcal{F}_3 &= - \int_0^L \frac{\partial(p q_f)}{\partial s} ds - \int_0^L \lambda \frac{\partial(C w \mu)}{\partial s} ds \\ &+ \frac{\lambda K_B T}{\pi R^2} \int_0^L \frac{\partial(C q_f)}{\partial s} ds, \end{aligned} \quad (3.32d)$$

and λ is expressed by the following relation:

$$\lambda = \frac{\sigma a_1 \pi R^2}{K_B T}. \quad (3.33)$$

4 | Computational algorithm

In this chapter we formulate a computational algorithm to numerically solve the mathematical model for fluid and protein transport and exchange described in equations (2.60). The major difficulty in the numerical solution is related to the nonlinearity of the equation (2.60d), where the unknown variables C and q_f are present in product form. To address this problem we use a fixed-point iteration whose basic goal is to decouple the equations for the fluid part from the equations for the protein part, in such a way that the solution of the nonlinear system is reduced to the successive solution of two model subblocks (fluid and protein blocks) in an iterative fashion until convergence is achieved. The details of the fixed-point iteration method are shown in Section 4.2. The other steps performed to solve the problem numerically involve time discretization, which is executed using Backward Euler method, as shown in Section 4.1, and space discretization, which is achieved thanks to Galerkin finite element approximation, as shown in Section 4.3. Moreover, in Section 4.4 we find the exact solution in the ideal case where protein is absent. This purely academic exact solution allows us to validate the model by comparison with the numerical solution and calculation of numerical errors. The results obtained in this regard are shown in Section 4.5.

4.1. Backward Euler method

Before providing the details of the Backward Euler method, for ease of reference, we report below the problem depicted in (2.60) divided into the two blocks of equations for fluid and protein:

Fluid block:

$$\begin{cases} \frac{\partial q_f}{\partial s} + 2\pi R L_p(p - \sigma aC) = 0, & s \in (0, L), t \in (0, T), \\ \frac{\rho}{\pi R^2} \frac{\partial q_f}{\partial t} = -\frac{\partial p}{\partial s} - \alpha q_f, & s \in (0, L), t \in (0, T), \end{cases} \quad (4.1a)$$

$$(4.1b)$$

Protein block:

$$\begin{cases} \frac{\partial C}{\partial t} + \frac{1}{\pi R^2} \frac{\partial q_p}{\partial s} + \frac{2(1-\sigma)}{\sigma R} P_d C = 0, & s \in (0, L), t \in (0, T), \\ q_p = C q_f - \pi R^2 D \frac{\partial C}{\partial s}, & s \in (0, L), t \in (0, T), \end{cases} \quad (4.2a)$$

$$s \in (0, L), t \in (0, T), \quad (4.2b)$$

where we substituted the values of the lateral volumetric flow rate j_f and of the lateral mass flow rate j_p through the relationships expressed in (3.27) and (3.28), respectively. We also recall that, as in Chapter 3, we consider $\alpha = \frac{2\mu_w(\gamma+2)}{\pi R^4}$ and the values of the pressures and protein concentration in the tissue equal to zero. Analytically solving the problem consists of finding the four dependent variables $q_f = q_f(s, t)$, $p = p(s, t)$, $q_p = q_p(s, t)$ and $C = C(s, t)$ for $s \in (0, L)$ and $t \in (0, T)$, for given initial data and boundary conditions. Fulfilling this task is a nontrivial problem, for this reason our goal is to compute a numerical approximation by discretizing the problem in time and space. More specifically, in this section we describe the Backward Euler method to achieve time discretization, an implicit one-step method that is reliable from the point of view of stability. In fact, it can be proved that Backward Euler is unconditionally stable, namely the method benefits absolute stability without any restriction on the time step Δt (see, for example, [12]). Moreover, regarding the accuracy, Backward Euler's local truncation error is of the order of $\Delta t + h^2$, where h denotes the spatial discretization step which will be introduced in Section 4.3. The properties just stated apply to parabolic equations. Actually, it is not immediate to see that equations in systems (4.1) and (4.2) are parabolic because they constitute a coupled model in which variables are mixed, for example, the concentration C , a protein-related variable, appears in the fluid block and vice versa the axial volumetric flow rate q_f , a fluid-related variable, is present in the protein block. However, thanks to the fixed point iterations, that will allow us to decouple the problem in Section 4.2, we can consider as if the concentration C and the axial volumetric flow rate q_f were given in equation (4.1a) and (4.2b), respectively. In light of this remark, the blocks of fluid and protein equations can be considered parabolic, and the theoretical argument for Backward Euler stability and convergence applies.

The method starts dividing the time interval into N homogeneous intervals of size $\Delta t = \frac{T}{N} > 0$ such that the time instants are computed as below:

$$t^n = n\Delta t, \quad n = 0, 1, 2, \dots, N. \quad (4.3)$$

Notice that $t^0 = 0$ and $t^N = N\Delta t = N\frac{T}{N} = T$. Denoting $u(s, t)$ a generic unknown variable, we indicate with $u^n(s)$ its numerical approximation at the instant t^n . Since the

approximations still depend on the variable s , at this stage we are performing a semi-discretization of the problem. In view of these considerations, once provided the initial conditions $q_f^0(s) = q_f(s, 0)$, $p^0(s) = p(s, 0)$, $q_p^0(s) = q_p(s, 0)$ and $C^0(s) = C(s, 0)$, the Backward Euler method is stated as follows:

Backward Euler method:

For $n = 0, 1, 2 \dots N$, given $q_f^n(s)$, $p^n(s)$, $q_p^n(s)$ and $C^n(s)$, solve the following blocks of equations:

Fluid block:

$$\left\{ \begin{array}{l} \frac{\partial q_f^{n+1}}{\partial s} + 2\pi R L_p (p^{n+1} - \sigma a C^{n+1}) = 0, \\ \frac{\rho}{\pi R^2} \frac{q_f^{n+1}}{\Delta t} = \frac{\rho}{\pi R^2} \frac{q_f^n}{\Delta t} - \frac{\partial p^{n+1}}{\partial s} - \alpha q_f^{n+1}, \end{array} \right. \quad s \in (0, L), \quad (4.4a)$$

$$\left\{ \begin{array}{l} \frac{\partial q_f^{n+1}}{\partial s} + 2\pi R L_p (p^{n+1} - \sigma a C^{n+1}) = 0, \\ \frac{\rho}{\pi R^2} \frac{q_f^{n+1}}{\Delta t} = \frac{\rho}{\pi R^2} \frac{q_f^n}{\Delta t} - \frac{\partial p^{n+1}}{\partial s} - \alpha q_f^{n+1}, \end{array} \right. \quad s \in (0, L), \quad (4.4b)$$

Protein block:

$$\left\{ \begin{array}{l} \frac{C^{n+1}}{\Delta t} + \frac{1}{\pi R^2} \frac{\partial q_p^{n+1}}{\partial s} + \frac{2(1-\sigma)}{\sigma R} P_d C^{n+1} = \frac{C^n}{\Delta t}, \\ q_p^{n+1} = C^{n+1} q_f^{n+1} - \pi R^2 D \frac{\partial C^{n+1}}{\partial s}, \end{array} \right. \quad s \in (0, L), \quad (4.5a)$$

$$\left\{ \begin{array}{l} \frac{C^{n+1}}{\Delta t} + \frac{1}{\pi R^2} \frac{\partial q_p^{n+1}}{\partial s} + \frac{2(1-\sigma)}{\sigma R} P_d C^{n+1} = \frac{C^n}{\Delta t}, \\ q_p^{n+1} = C^{n+1} q_f^{n+1} - \pi R^2 D \frac{\partial C^{n+1}}{\partial s}, \end{array} \right. \quad s \in (0, L), \quad (4.5b)$$

to determine the functions $q_f^{n+1}(s)$, $p^{n+1}(s)$, $q_p^{n+1}(s)$ and $C^{n+1}(s)$ for $s \in (0, L)$.

4.2. Fixed-point iteration

The goal of this section is to elaborate an iterative algorithm to solve the fluid-protein coupled problem in equations (4.4) and (4.5). First of all, since the numerical approximations $u^{n+1}(s)$ at the time instant $n+1$ are the unknowns of the problem, we rewrite them without the superscript, so that $q_f^{n+1}(s) = q_f(s)$, $p^{n+1}(s) = p(s)$, $q_p^{n+1}(s) = q_p(s)$ and $C^{n+1}(s) = C(s)$. This abuse of notation facilitates the writing of the fixed point method and allows us to reformulate the problem in (4.4) and (4.5) for each time step ($\forall n \geq 0$) as follows:

Given $q_f^n(s)$, $p^n(s)$, $q_p^n(s)$ and $C^n(s)$, find the functions $q_f(s)$, $p(s)$, $q_p(s)$ and $C(s)$ solving the following systems of equations:

Fluid block:

$$\left\{ \begin{array}{l} \frac{\partial q_f}{\partial s} + 2\pi R L_p (p - \sigma a C) = 0, \\ \frac{\rho}{\pi R^2 \Delta t} q_f = \frac{\rho}{\pi R^2 \Delta t} q_f^n - \frac{\partial p}{\partial s} - \alpha q_f, \end{array} \right. \quad s \in (0, L), \quad (4.6a)$$

$$\left\{ \begin{array}{l} \frac{\partial q_f}{\partial s} + 2\pi R L_p (p - \sigma a C) = 0, \\ \frac{\rho}{\pi R^2 \Delta t} q_f = \frac{\rho}{\pi R^2 \Delta t} q_f^n - \frac{\partial p}{\partial s} - \alpha q_f, \end{array} \right. \quad s \in (0, L), \quad (4.6b)$$

Protein block:

$$\left\{ \begin{array}{l} \frac{C}{\Delta t} + \frac{1}{\pi R^2} \frac{\partial q_p}{\partial s} + \frac{2(1-\sigma)}{\sigma R} P_d C = \frac{C^n}{\Delta t}, \\ q_p = C q_f - \pi R^2 D \frac{\partial C}{\partial s}, \end{array} \right. \quad s \in (0, L), \quad (4.7a)$$

$$\left\{ \begin{array}{l} \frac{C}{\Delta t} + \frac{1}{\pi R^2} \frac{\partial q_p}{\partial s} + \frac{2(1-\sigma)}{\sigma R} P_d C = \frac{C^n}{\Delta t}, \\ q_p = C q_f - \pi R^2 D \frac{\partial C}{\partial s}, \end{array} \right. \quad s \in (0, L), \quad (4.7b)$$

Note that from Equation (4.6b) we can express q_f as a function of the pressure:

$$q_f = -\frac{1}{K} \frac{\partial p}{\partial s} + \frac{\rho}{\pi R^2 K \Delta t} q_f^n, \quad (4.8)$$

where we defined $K := \frac{\rho}{\pi R^2 \Delta t} + \alpha$. Therefore, substituting the expression (4.8) for q_f , equation (4.6a) becomes:

$$\frac{\partial}{\partial s} \left(-\frac{1}{K} \frac{\partial p}{\partial s} \right) + 2\pi R L_p p = 2\pi R L_p \sigma a C - \frac{\rho}{\pi R^2 K \Delta t} \frac{\partial q_f^n}{\partial s}. \quad (4.9)$$

Instead, regarding the protein block, we can substitute the expression (4.7b) for q_p into equation (4.7a) which becomes:

$$\frac{\partial}{\partial s} \left(\frac{q_f}{\pi R^2} C - D \frac{\partial C}{\partial s} \right) + \left(\frac{1}{\Delta t} + \frac{2(1-\sigma)}{\sigma R} P_d \right) C = \frac{C^n}{\Delta t}. \quad (4.10)$$

Now we are ready to formulate the computational algorithm. In essence each step k , $k \geq 0$, of the iterative procedure consists of:

Step 1: Fluid block

- 1.1 Set $C(s) = C^{(k)}(s)$ for $s \in (0, L)$ in equation (4.9);
- 1.2 Solve the fluid equation (4.9), supplied by boundary conditions, to determine

the function $p(s) = p^{(k+1)}(s)$ for $s \in (0, L)$:

$$\frac{\partial}{\partial s} \left(-\frac{1}{K} \frac{\partial p^{(k+1)}}{\partial s} \right) + 2\pi R L_p p^{(k+1)} = 2\pi R L_p \sigma a C^{(k)} - \frac{\rho}{\pi R^2 K \Delta t} \frac{\partial q_f^n}{\partial s}. \quad (4.11)$$

Step 2: Update axial volumetric flow rate

2.1 Compute the axial volumetric flow rate $q_f(s) = q_f^{(k+1)}(s)$ for $s \in (0, L)$ through relation (4.8):

$$q_f^{(k+1)} = -\frac{1}{K} \frac{\partial p^{(k+1)}}{\partial s} + \frac{\rho}{\pi R^2 K \Delta t} q_f^n. \quad (4.12)$$

Step 3: Protein block

3.1 Solve the protein equation (4.10), supplied by boundary conditions, to determine the function $C(s) = C^{(k+1)}(s)$ for $s \in (0, L)$: (4.8):

$$\frac{\partial}{\partial s} \left(\frac{q_f^{(k+1)}}{\pi R^2} C^{(k+1)} - D \frac{\partial C^{(k+1)}}{\partial s} \right) + \left(\frac{1}{\Delta t} + \frac{2(1-\sigma)}{\sigma R} P_d \right) C^{(k+1)} = \frac{C^n}{\Delta t}. \quad (4.13)$$

Step 4: Convergence checks

4.1 Compute the estimates of the iteration errors:

$$err_p^{(k)} := \frac{\|p^{(k+1)} - p^{(k)}\|_\infty}{\|p^{(k+1)}\|_\infty}, \quad err_C^{(k)} := \frac{\|C^{(k+1)} - C^{(k)}\|_\infty}{\|C^{(k+1)}\|_\infty}, \quad (4.14)$$

where $\|\Phi\|_\infty := \max_{s \in (0, L)} |\Phi(s)|$ for any continuous function $\Phi : (0, L) \rightarrow \mathbb{R}$.

4.2 Set $err^{(k)} := \max \{err_p^{(k)}, err_C^{(k)}\}$.

4.3 If $err^{(k)} < toll$, then the fixed-point iteration has reached convergence and we can proceed to Step 5, otherwise the procedure is repeated starting from Step 1.

Step 5: Post-processing

5.1 Solve the axial mass flow rate and the lateral fluxes via equations (4.7b), (3.27) and (3.28).

The fixed-point algorithm requires the choice of a specific value for the tolerance $toll$ and an initial guess for the distribution of hydrostatic pressure and protein concentration, corresponding to $k = 0$. The results reported in Section 4.5 have been obtained by

setting $toll = 10^{-6}$, whereas, as initial guess, we consider the mean value between the ones provided by the boundary conditions at the points $s = 0$ and $s = L$.

4.3. Finite element method for diffusion-advection-reaction problem

Steps 1 and 3 in the computational algorithm depicted in Section 4.2 require the solution of diffusion-advection-reaction problems. More specifically, equations (4.11) and (4.13) can be written in the general form:

$$\frac{\partial \mathcal{J}}{\partial s} + r U = g \quad s \in (0, L), \quad (4.15a)$$

$$\mathcal{J} = \mathcal{V} U - \mathcal{D} \frac{\partial U}{\partial s} \quad s \in (0, L). \quad (4.15b)$$

In the above first-order model system, $U = U(s)$ is the dependent variable and $\mathcal{J} = \mathcal{J}(s)$ is the associated flux density comprising an advective term $\mathcal{V} U$ and a diffusive term $-\mathcal{D} \frac{\partial U}{\partial s}$, where \mathcal{V} and \mathcal{D} are given functions representing the advective field that passively drives the motion of U and the diffusivity of U , respectively. The given functions r and g represent the reaction and generation terms, respectively. The problem (4.15) can be solved once the boundary conditions are provided. In particular, we consider the most general expression for the boundary conditions, which includes the possibility of having Dirichlet, Neumann or Robin conditions, and is expressed as follows:

$$\gamma_0 \mathcal{J} \cdot \mathbf{n}_0 = \alpha_0 U(0) - \beta_0, \quad s = 0, \quad (4.16a)$$

$$\gamma_L \mathcal{J} \cdot \mathbf{n}_L = \alpha_L U(L) - \beta_L, \quad s = L, \quad (4.16b)$$

where \mathbf{n}_0 and \mathbf{n}_L are the normal vectors to the inlet surface Σ_0 and to the outlet surface Σ_L , respectively. Because of the 1D geometry, it can be noted that $\mathbf{n}_0 = -1$ and $\mathbf{n}_L = 1$ (Figure 4.1). Instead, the parameters γ , α and β in equation (4.16), which generally are functions of time, are computed at time t^n .

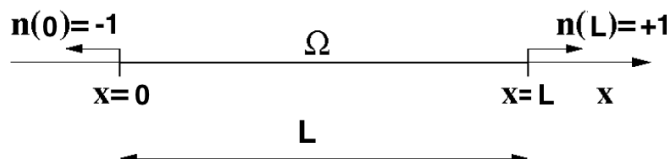


Figure 4.1: Geometrical notation and unit normal vectors.

If $\gamma = 1$, the corresponding relation (4.16) is known as Robin condition, while if $\gamma = 0$, relation (4.16) degenerates into the so-called Dirichlet condition, where the value of the unknown U is given at the boundary and is equal to $\frac{\beta}{\alpha}$. In the case of a Robin condition, if $\alpha = 0$ then the (outward) flux density \mathcal{J} is given at the boundary and equal to $-\beta$, and relation (4.16) takes the name of Neumann condition.

In our model, the dependent variables for the fluid equation (4.11) and for the protein equation (4.13) are respectively $p^{(k+1)}$ and $C^{(k+1)}$, and the coefficients of reaction r , generation g , advection \mathcal{V} and diffusion \mathcal{D} assume the following forms:

Coefficients for fluid equation:

$$\left\{ \begin{array}{l} r = 2\pi R L_p, \\ g = 2\pi R L_p \sigma a C^{(k)} - \frac{\rho}{\pi R^2 K \Delta t} \frac{\partial q_f^n}{\partial s}, \\ \mathcal{V} = 0, \\ \mathcal{D} = \frac{1}{K}. \end{array} \right. \quad (4.17a)$$

$$\left\{ \begin{array}{l} r = 2\pi R L_p, \\ g = 2\pi R L_p \sigma a C^{(k)} - \frac{\rho}{\pi R^2 K \Delta t} \frac{\partial q_f^n}{\partial s}, \\ \mathcal{V} = 0, \\ \mathcal{D} = \frac{1}{K}. \end{array} \right. \quad (4.17b)$$

$$\left\{ \begin{array}{l} r = 2\pi R L_p, \\ g = 2\pi R L_p \sigma a C^{(k)} - \frac{\rho}{\pi R^2 K \Delta t} \frac{\partial q_f^n}{\partial s}, \\ \mathcal{V} = 0, \\ \mathcal{D} = \frac{1}{K}. \end{array} \right. \quad (4.17c)$$

$$\left\{ \begin{array}{l} r = 2\pi R L_p, \\ g = 2\pi R L_p \sigma a C^{(k)} - \frac{\rho}{\pi R^2 K \Delta t} \frac{\partial q_f^n}{\partial s}, \\ \mathcal{V} = 0, \\ \mathcal{D} = \frac{1}{K}. \end{array} \right. \quad (4.17d)$$

Coefficients for protein equation:

$$\left\{ \begin{array}{l} r = \frac{1}{\Delta t} + \frac{2(1-\sigma)}{\sigma R} P_d, \\ g = \frac{C^n}{\Delta t}, \\ \mathcal{V} = \frac{q_f^{(k+1)}}{\pi R^2}, \\ \mathcal{D} = D. \end{array} \right. \quad (4.18a)$$

$$\left\{ \begin{array}{l} r = \frac{1}{\Delta t} + \frac{2(1-\sigma)}{\sigma R} P_d, \\ g = \frac{C^n}{\Delta t}, \\ \mathcal{V} = \frac{q_f^{(k+1)}}{\pi R^2}, \\ \mathcal{D} = D. \end{array} \right. \quad (4.18b)$$

$$\left\{ \begin{array}{l} r = \frac{1}{\Delta t} + \frac{2(1-\sigma)}{\sigma R} P_d, \\ g = \frac{C^n}{\Delta t}, \\ \mathcal{V} = \frac{q_f^{(k+1)}}{\pi R^2}, \\ \mathcal{D} = D. \end{array} \right. \quad (4.18c)$$

$$\left\{ \begin{array}{l} r = \frac{1}{\Delta t} + \frac{2(1-\sigma)}{\sigma R} P_d, \\ g = \frac{C^n}{\Delta t}, \\ \mathcal{V} = \frac{q_f^{(k+1)}}{\pi R^2}, \\ \mathcal{D} = D. \end{array} \right. \quad (4.18d)$$

The numerical solution of the two diffusion-advection-reaction problems is conducted using a displacement-based form of the Galerkin finite element approximation with piecewise linear finite elements. For a detailed description of the method and of its theoretical properties, we refer to [13], Chapter 23. Summing up, $h > 0$ denotes the mesh size on the space interval $(0, L)$, and U_h stands for the numerical approximation of U computed on the partition of the interval $(0, L)$ into elements of size less than or equal than h . In practice, the application of finite element method to approximate the fluid and protein equations (4.11) and (4.13) leads to solving at each step k of the fixed-point iteration illustrated in Section 4.2 the following linear algebraic system

$$\underline{\underline{\mathbf{K}}} \underline{\mathbf{U}} = \underline{\mathbf{G}}, \quad (4.19)$$

where $\underline{\mathbf{U}}$ is the column vector containing the nodal values of the approximation U_h of U , $\underline{\mathbf{G}}$ is the load vector and $\underline{\underline{\mathbf{K}}}$ is a positive definite square matrix that benefits the property of being an M-matrix. This ensures that $\underline{\underline{\mathbf{K}}}^{-1}$ is a strictly positive so that, in turn, also the solution $\underline{\mathbf{U}} = \underline{\underline{\mathbf{K}}}^{-1} \underline{\mathbf{G}}$ is a positive vector. This result is an instance of the discrete maximum principle, see [13] for reference. In the case of the protein problem, the influence of the advective field $q_f^{(k+1)}/\pi R^2$ makes the diffusion-advection-reaction equation (4.13) strongly advection-dominated. This requires the adoption of a stabilization technique to prevent the numerical solution from being affected by spurious unphysical oscillations which might pollute the computed protein concentration so seriously to violate the property of positivity. In the numerical algorithm implemented in this work we use the exponentially-fitted stabilization proposed by Scharfetter and Gummel for the simulation of the drift-diffusion equations in semiconductor devices [15]. The convergence estimates for Galerkin finite element method can be stated as follows:

$$\|U - U_h\|_\infty \leq Ch^2, \quad (4.20a)$$

$$\|U - U_h\|_{L^2(\Omega)} \leq Ch^2, \quad (4.20b)$$

where $\|\cdot\|_\infty$ and $\|\cdot\|_{L^2(\Omega)}$ are the infinity and the L_2 norm, respectively. The estimates in (4.20) refer to Theorems 23.6 and 23.8 of [13], Chapter 23, and are valid under the assumption that the domain, the solution and the diffusion, reaction, transport coefficients are sufficiently regular.

4.4. Exact solution ideal case with no proteins

For the purpose of validating the computational algorithm described in Section 4.2, that is solved using the Galerkin finite element approximation, as briefly discussed in Section 4.3, we look for an exact solution of the problem. For the sake of simplicity, we take into account the ideal case where protein is absent, namely protein concentration $C = 0$. Therefore, the problem depicted in (2.60) reduces to the following system of equations, which corresponds to the equations for the fluid block only:

$$\begin{cases} \frac{\partial q_f}{\partial s} + 2\pi R L_p p = 0, & s \in (0, L), t \in (0, T), \\ \frac{\rho}{\pi R^2} \frac{\partial q_f}{\partial t} = -\frac{\partial p}{\partial s} - \alpha q_f, & s \in (0, L), t \in (0, T), \\ B.C. & s = 0, s = L, t \in (0, T), \\ I.C. & s \in (0, L), t = 0. \end{cases} \quad (4.21a)$$

$$\begin{cases} \frac{\partial q_f}{\partial s} + 2\pi R L_p p = 0, & s \in (0, L), t \in (0, T), \\ \frac{\rho}{\pi R^2} \frac{\partial q_f}{\partial t} = -\frac{\partial p}{\partial s} - \alpha q_f, & s \in (0, L), t \in (0, T), \\ B.C. & s = 0, s = L, t \in (0, T), \\ I.C. & s \in (0, L), t = 0. \end{cases} \quad (4.21b)$$

$$\begin{cases} \frac{\partial q_f}{\partial s} + 2\pi R L_p p = 0, & s \in (0, L), t \in (0, T), \\ \frac{\rho}{\pi R^2} \frac{\partial q_f}{\partial t} = -\frac{\partial p}{\partial s} - \alpha q_f, & s \in (0, L), t \in (0, T), \\ B.C. & s = 0, s = L, t \in (0, T), \\ I.C. & s \in (0, L), t = 0. \end{cases} \quad (4.21c)$$

$$\begin{cases} \frac{\partial q_f}{\partial s} + 2\pi R L_p p = 0, & s \in (0, L), t \in (0, T), \\ \frac{\rho}{\pi R^2} \frac{\partial q_f}{\partial t} = -\frac{\partial p}{\partial s} - \alpha q_f, & s \in (0, L), t \in (0, T), \\ B.C. & s = 0, s = L, t \in (0, T), \\ I.C. & s \in (0, L), t = 0. \end{cases} \quad (4.21d)$$

Clearly, under changing initial and boundary conditions, the solution of the system of equations (4.21) takes different forms. Thus, instead of setting boundary and initial conditions and solving the equations (4.21), we construct an a priori solution. In particular, to properly test the piecewise linear finite element method, we choose to consider a sinusoidal exact solution that can be expressed as:

$$p(s, t) = e^{\lambda t} (\cos(k s) + \sin(k s)). \quad (4.22)$$

The parameter λ , if negative, can be considered as an exponential decay rate for the function p . Indeed, in the field of signal processing, the quantity $-\lambda$ is called decay constant, in order to have this decay constant always positive. However, to simplify the following calculations, we prefer to consider this more general parameter with sign. As we will see, in the exact solution considered to achieve the numerical results shown in Section 4.5, λ is always negative. Instead, the parameter k is known in physical sciences as the wave number. It is the spatial frequency of a wave.

The goal is to find the values of λ and k to make the pressure p satisfy equations (4.21). We start noting that from equation (4.21a) we can express the space derivative of the axial volumetric flow rate q_f as:

$$\frac{\partial q_f}{\partial s} = -2\pi R L_p p. \quad (4.23)$$

From equation (4.26a) the axial volumetric flow rate q_f can be found by integrating both members in space and discarding any time-dependent integration constant, obtaining:

$$q_f = -2\pi R L_p \int p ds \quad (4.24)$$

Integrating the sinusoidal function for p in (4.22), equation (4.24) becomes:

$$q_f = \frac{2\pi R L_p}{k} e^{\lambda t} (\cos(k s) - \sin(k s)) \quad (4.25)$$

Hence, we want to replace the expressions (4.22) for p and (4.25) for q_f into the equation (4.21b) in order to find a relationship between the parameters λ and k that allows to the functions p and q_f to satisfy the problem (4.21). For this purpose, starting from the

expressions (4.22) and (4.25), it is useful to calculate the following derivatives:

$$\left\{ \begin{array}{l} \frac{\partial q_f}{\partial t} = \frac{\lambda}{k} 2\pi R L_p e^{\lambda t} (\cos(k s) - \sin(k s)), \\ \frac{\partial p}{\partial s} = k e^{\lambda t} (\cos(k s) - \sin(k s)). \end{array} \right. \quad (4.26a)$$

$$\left\{ \begin{array}{l} \frac{\partial q_f}{\partial t} = \frac{\lambda}{k} 2\pi R L_p e^{\lambda t} (\cos(k s) - \sin(k s)), \\ \frac{\partial p}{\partial s} = k e^{\lambda t} (\cos(k s) - \sin(k s)). \end{array} \right. \quad (4.26b)$$

Replacing (4.25), (4.26a) and (4.26b) into equation (4.21b) yields:

$$\begin{aligned} \frac{\rho}{\pi R^2} \frac{\lambda}{k} 2\pi R L_p e^{\lambda t} (\cos(k s) - \sin(k s)) = \\ - k e^{\lambda t} (\cos(k s) - \sin(k s)) - \alpha \frac{2\pi R L_p}{k} e^{\lambda t} (\cos(k s) - \sin(k s)). \end{aligned} \quad (4.27)$$

Analyzing equation (4.27), simple algebra leads to finding the following relationship between the parameters λ and k :

$$\lambda = - \left(\frac{R}{2\rho L_p} \right) k^2 - \frac{\alpha \pi R^2}{\rho}. \quad (4.28)$$

Thanks to equation (4.28) we can fix a value for the wave number k , retrieve the value for the decay constant λ , and therefore compute the expressions of the pressure p and the axial volumetric flow rate q_f through relations (4.22) and (4.25). With this procedure, the functions $p(s, t)$ and $q_f(s, t)$ represent an a priori constructed solution of the problem (4.21), since they satisfy equations (4.21a) and (4.21b). A posteriori, we can then fix the values of p and q_f at the endpoints by setting them equal to $p(0, t)$, $p(L, t)$, $q_f(0, t)$ and $q_f(L, t)$, corresponding to the case of Dirichlet boundary conditions. Moreover, we can fix the initial conditions by putting them equal to the functions $p(s, 0)$ and $q_f(s, 0)$. These conditions allow us to numerically solve the problem using the computational algorithm depicted in Section 4.2. More specifically, since the problem is reduced to the fluid equation only, the steps to consider are Step 1, 4 and 5. In the next section, we show the results obtained by comparing the exact solution achieved in this section, with the numerical solution. For such results, we consider two cases of exact solution with $|k| = 16 \text{ cm}^{-1}$ and $|k| = 140 \text{ cm}^{-1}$, finding the decay constant λ equal to approximately $-1 \cdot 10^6 \text{ s}^{-1}$ and $-8 \cdot 10^7 \text{ s}^{-1}$, respectively.

4.5. Numerical results

The goal of this section is the validation of the computational algorithm by comparison of the exact solution derived in Section 4.4 and the numerical solution computed via the iterative procedure illustrated in Section 4.2. As a first step, we compare the two solutions

graphically. In this case, we wish to understand whether the numerical solution is capable of capturing the sinusoidal nature of the exact solution. For this reason, in the expression (4.22) of the exact solution for p , we consider a wave number with large $|k| = 140 \text{ cm}^{-1}$. For graphical reasons, the sign has been considered negative but it is not relevant from the point of view of the results. The decay constant λ resulting from equation (4.28) is equal to $-8 \cdot 10^7 \text{ s}^{-1}$. Therefore, the exact solution takes the following form:

$$p(s, t) = e^{-8 \cdot 10^7 t} (\cos(-140 s) + \sin(-140 s)), \quad s \in (0, L), t \in (0, T). \quad (4.29)$$

To appreciate the solution before its exponential decay occurs, we need a short time interval, in particular we consider $T = 3 \cdot 10^{-9} \text{ s}$. Instead, concerning the physical dimensions and physiological properties of the capillary, we take into account the real values. More specifically, we refer to capillary number 1 of the microvascular network analyzed in [5]. This vessel is an arterial capillary, which means that blood flow diverges at both ends. Its physical dimensions are a length of $534.7 \mu\text{m}$ and a radius of $10 \mu\text{m}$. All the values of the model parameters characterizing this capillary are given in Table 4.1.

Description	Symbols	Value	Unit
Radius of the vessel	R	10	$[\mu\text{m}]$
Length of the vessel	L	534.7	$[\mu\text{m}]$
Partial density of the fluid phase	ρ_{fp}	0.8	$[g \text{ cm}^{-3}]$
Water dynamic viscosity	μ_w	$1.1 \cdot 10^{-5}$	$[\text{cm H}_2\text{O s}]$
Hydraulic conductivity of the membrane	L_p	$1.5 \cdot 10^{-7}$	$[\text{cm s}^{-1} \text{ cm H}_2\text{O}^{-1}]$
Protein reflection coefficient of the membrane	σ	0.8	$[-]$
Solute permeability of the membrane	P_d	$1.7 \cdot 10^{-7}$	$[\text{cm s}^{-1}]$
Protein diffusion coefficient	D_{pt}	$61 \cdot 10^{-8}$	$[\text{cm}^2 \text{ s}^{-1}]$
Shape factor	γ	2	$[-]$

Table 4.1: Summary of physical dimensions and physiological properties of the capillary adopted in the numerical results.

The 3D plot of the numerical solution compared to the exact solution for pressure p and for the axial volumetric flow rate q_f is reported in Figures 4.2 and 4.3, respectively. As can be seen from these plots, the numerical solutions are accurate. The numerical approximation of the axial volumetric flow rate q_f is a piecewise linear function on the elements, since it is computed via equation (4.12) starting from the space derivative of

the pressure. Another way to compare the numerical solution with the exact solution is to look at selected snapshots of the solution at different time instants. The plots are reported in Figures 4.4 and 4.5 where the numerical solution (red dots) is compared to the exact solution (black line) at three different time instants. Figure 4.4 refers to pressure p , whereas Figure 4.5 refers to the axial volumetric flow rate q_f .

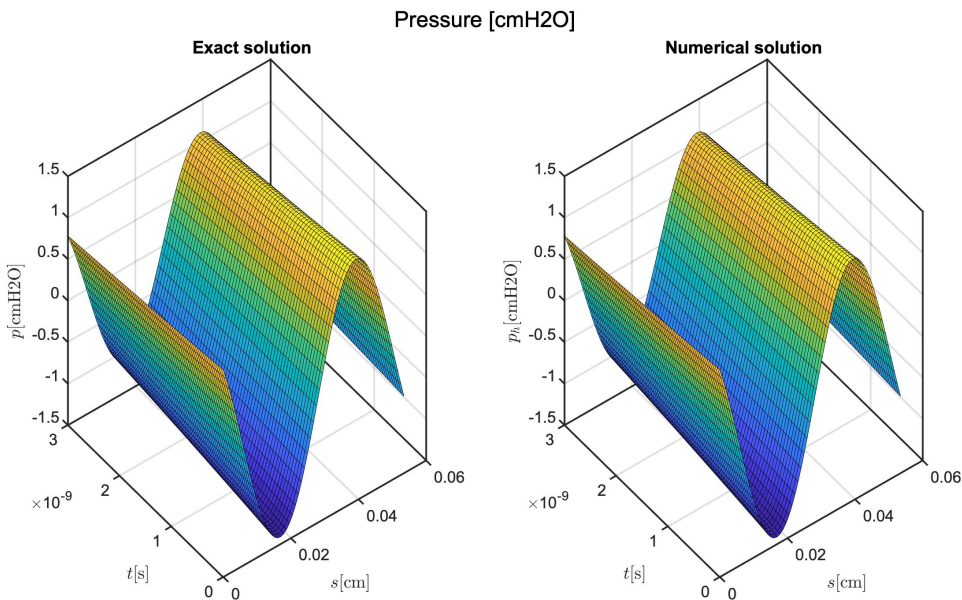


Figure 4.2: 3D plot of the pressure exact solution (left side) compared to the pressure numerical solution (right side) in the domain $(0, L) \times (0, T)$ with $T = 3 \cdot 10^{-9} s$ and $L = 0.0534 cm$

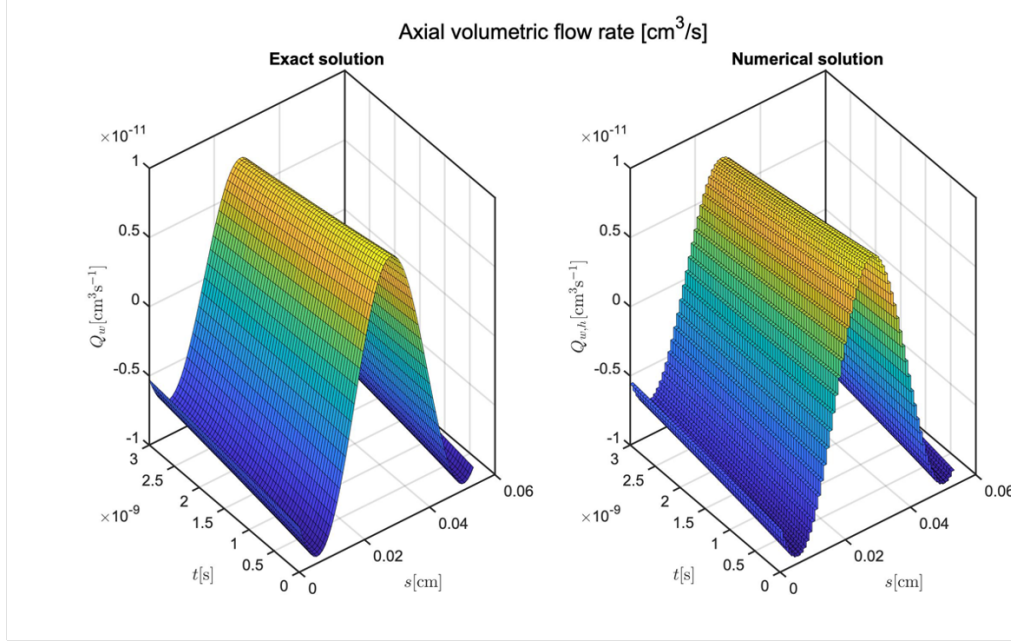


Figure 4.3: 3D plot of the axial volumetric flow rate exact solution (left side) compared to the axial volumetric flow rate numerical solution (right side) in the domain $(0, L) \times (0, T)$ with $T = 3 \cdot 10^{-9} s$ and $L = 0.0534 cm$.

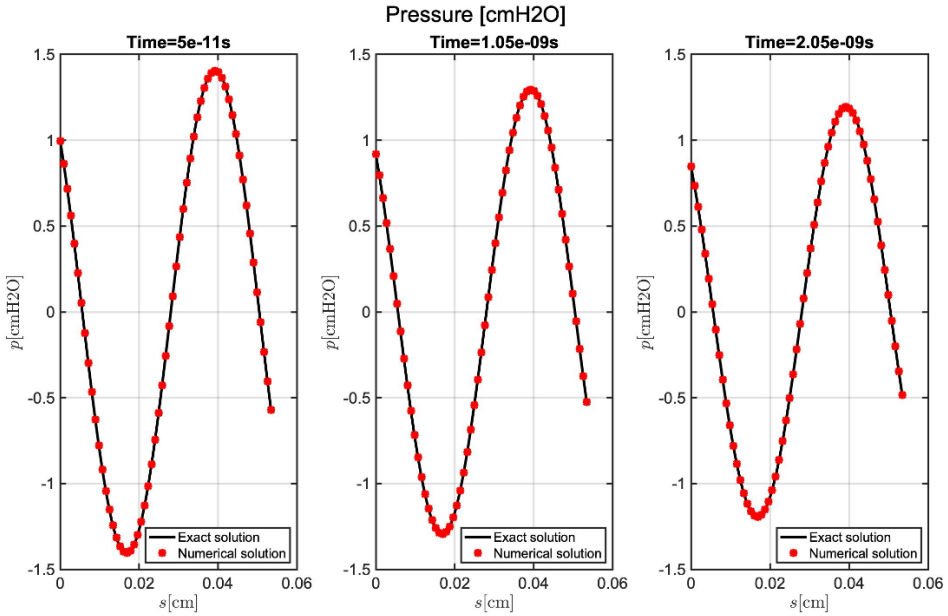


Figure 4.4: The pressure numerical solution (red dots) compared to the pressure exact solution (black line) in the domain $(0, L)$ with $L = 0.0534 cm$ at three different time instants, in particular $T_1 = 5 \cdot 10^{-11} s$, $T_2 = 1.05 \cdot 10^{-9} s$ and $T_3 = 2.05 \cdot 10^{-9} s$

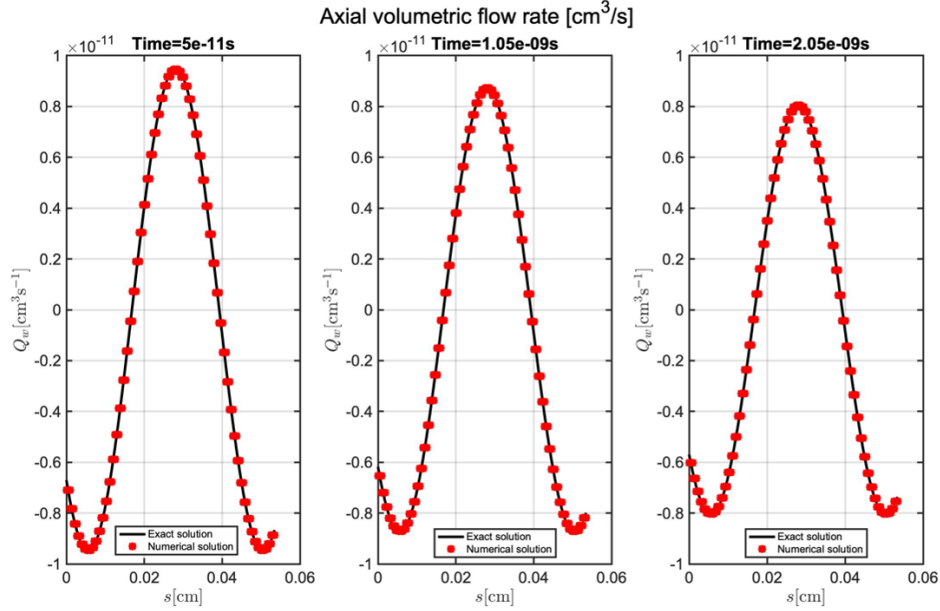


Figure 4.5: The axial volumetric flow rate numerical solution (red dots) compared to the axial volumetric flow rate exact solution (black line) in the domain $(0, L)$ with $L = 0.0534 \text{ cm}$ at three different time instants, in particular $T_1 = 5 \cdot 10^{-11} \text{ s}$, $T_2 = 1.05 \cdot 10^{-9} \text{ s}$ and $T_3 = 2.05 \cdot 10^{-9} \text{ s}$.

The most accurate method for testing the reliability of the iterative algorithm described in Section 4.2 is the computation of numerical errors. In particular, we compute two different types of error. The first type, which we call L_∞ -error, is calculated as follows:

$$\text{Err}_{L_\infty} = \max_n \left(\max_i |u_h(s_i, t_n) - u_{ex}(s_i, t_n)| \right), \quad (4.30)$$

where s_i and t_n indicate the i -th and n -th node of spatial and temporal discretization, respectively, with $i = 0, 1, \dots, N_{\text{elem}}$ and $n = 0, 1, \dots, N$ (N_{elem} is the number of space elements). The subscript h in (4.30) stands for the numerical solution, while the subscript ex for the exact one. Note that the variable u in (4.30) can be either the pressure p or the axial volumetric flow rate q_f . In the first case we call the error $\text{Err}_{L_\infty}(p)$, whereas in the latter $\text{Err}_{L_\infty}(q_f)$. The second type of error we compute, to which we refer as L_2 -error, is calculated as follows:

$$\text{Err}_{L_2} = \max_n (\|\mathbf{u}_h(t_n) - \mathbf{u}_{ex}(t_n)\|_2), \quad (4.31)$$

where $\mathbf{u}_h(t_n)$ and $\mathbf{u}_{ex}(t_n)$ are the vectors of the numerical solution and the exact one evaluated in spatial nodes s_i at time t_n with $i = 1, 2, \dots, N_{\text{Nodes}}$ and N_{Nodes} indicating the

number of finite element nodes. The vector 2-norm in (4.31) is defined as follows:

$$\|\mathbf{v}\|_2 := \sqrt{\sum_{i=0}^n |v_i|^2}, \quad (4.32)$$

for any vector \mathbf{v} in \mathbb{R}^n and can be considered the numerical approximation of the continuous L_2 -norm. The standard approach for convergence analysis is to progressively refine the mesh and studying the evolution of the error. In our case we perform two analyses, one refining the time mesh and the other refining the space mesh. The error analysis is performed choosing, in expression (4.22), the wave number k equal in modulus to 16 cm^{-1} , so that equation (4.28) provides a decay constant λ of $-1 \cdot 10^6 \text{ s}^{-1}$. Having the decay constant λ bigger than the one in (4.29) allows us to appreciate the sinusoidal form of the solution for longer time intervals, and to compute the errors for larger time mesh sizes Δt . In the case of time convergence analysis, this is useful since the possibility of having a larger Δt makes the temporal discretization error dominant over that in space, and thus easier to be detected. More specifically, regarding time error analysis, we fix 120 space elements, $T = 3 \cdot 10^{-7} \text{ s}$ and a refinement vector of 10, 20, 40, 80, 160, 320 mesh time elements. The graphic visualization of error trends is shown in Figures 4.6 and 4.7 where the L_∞ -error and the L_2 -error (red lines) are plotted in logarithmic scale together with a linear function in the time variable (dashed black line). This choice helps to show graphically that the errors are of linear order with respect to the time variable. The result is in agreement with the order of the local Backward Euler truncation error described in Section 4.1. Moreover, a quantitative evidence that the error in time is of order 1 is provided by calculating the orders of convergence, which are shown in Table 4.2.

Time convergence order

$\mathcal{O}(\text{Err}_{L_\infty}(p))$	0.979	0.988	0.995	0.999	1.002
$\mathcal{O}(\text{Err}_{L_\infty}(q_f))$	0.996	0.998	0.999	1.000	1.002
$\mathcal{O}(\text{Err}_{L_2}(p))$	0.977	0.988	0.995	0.999	1.003
$\mathcal{O}(\text{Err}_{L_2}(q_f))$	0.996	0.998	1.000	1.002	1.005

Table 4.2: Order of convergence of the errors computed by progressively refining the time mesh.

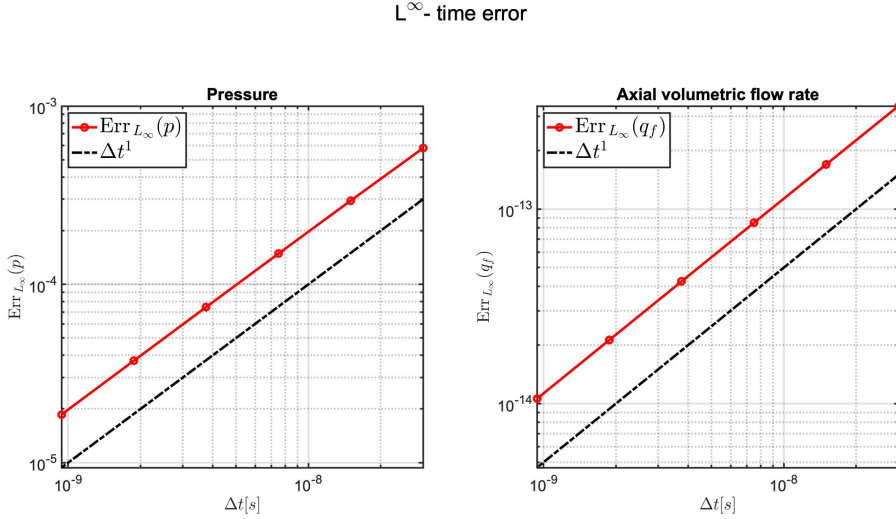


Figure 4.6: L_∞ - error for pressure p and axial volumetric flow rate q_f , computed by progressively refining the time mesh, decreases linearly. Specifically, we set a time interval $(0, T)$ with $T = 3 \cdot 10^{-7} s$ considering a refinement vector of 10, 20, 40, 80, 160, 320 mesh time elements.

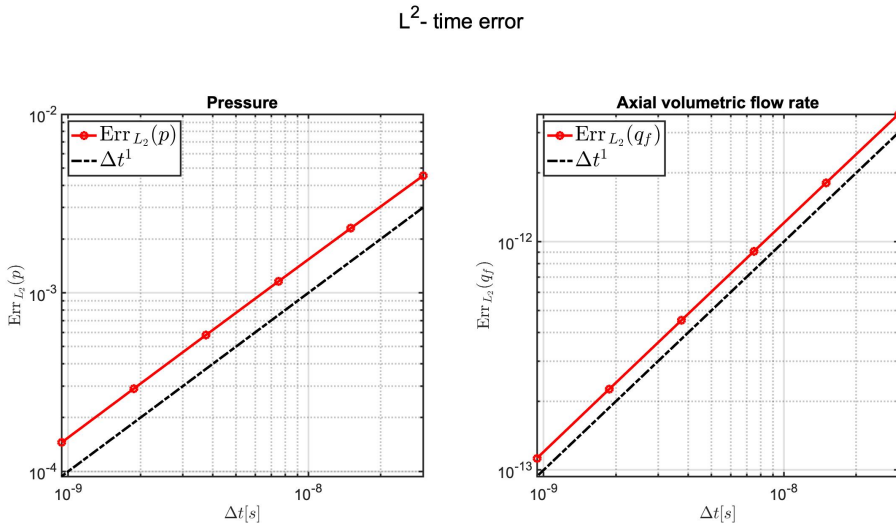


Figure 4.7: L_2 - error for pressure p and axial volumetric flow rate q_f , computed by progressively refining the time mesh, decreases linearly. Specifically, we set a time interval $(0, T)$ with $T = 3 \cdot 10^{-7} s$ considering a refinement vector of 10, 20, 40, 80, 160, 320 mesh time elements.

As far as space convergence analysis is concerned, we consider $T = 3 \cdot 10^{-9} s$ and we fix 120 time elements. This choice makes the time step Δt small and thus the error in space dominates over that in time, becoming easier to be detected. We consider a refinement vector of 10, 20, 40, 80, 160, 320 mesh space elements. The graphic visualization of error trends is shown in Figures 4.8 and 4.9 where the L_∞ -error and the L_2 -error (red lines) are plotted in logarithmic scale together with a quadratic function in the space variable (dashed black line). The figures show that the L_∞ -error is of order 2, whereas the L_2 -error has more than linear order but does not reach second order. These results are in agreement with the convergence estimates reported in equations (4.20). Figure 4.9 reveals that the L_2 -error for the axial volumetric flow rate q_f is affected by round-off error in correspondence of very small values of the discretization parameter h .

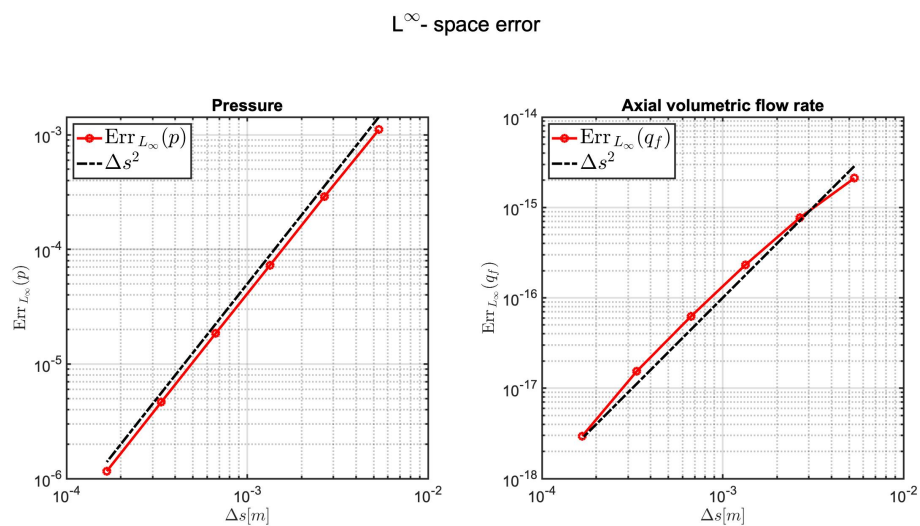


Figure 4.8: L_∞ -error for pressure p and axial volumetric flow rate q_f , computed by progressively refining the space mesh, decreases quadratically. Specifically, we set a space interval $(0, L)$ with $L = 0.0534\text{ cm}$, considering a refinement vector of 10, 20, 40, 80, 160, 320 mesh space elements.

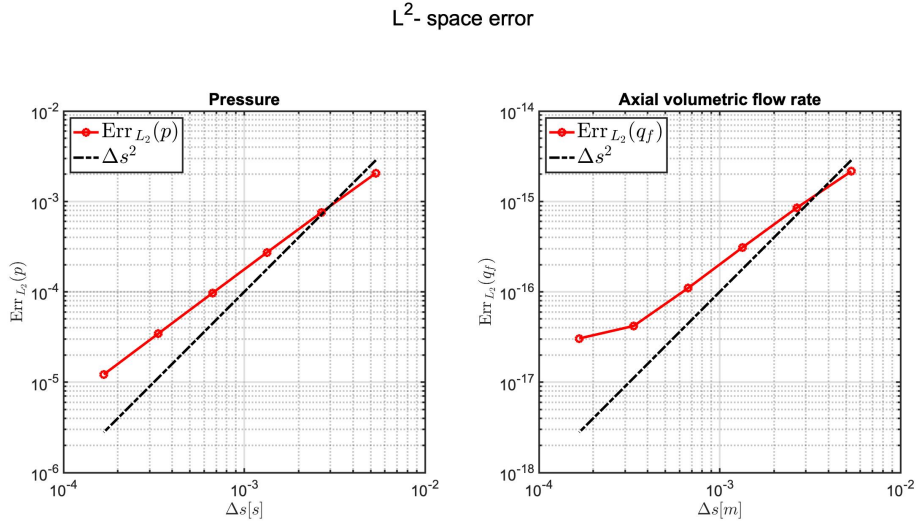


Figure 4.9: L_2 -error for pressure p and axial volumetric flow rate q_f , computed by progressively refining the space mesh, decreases more than linearly. Specifically, we set a space interval $(0, L)$ with $L = 0.0534\text{ cm}$, considering a refinement vector of 10, 20, 40, 80, 160, 320 mesh space elements.

The convergence order of errors when refining the space mesh is shown in Table 4.3.

Space convergence order

$\mathcal{O}(\text{Err}_{L_\infty}(p))$	1.937	1.990	1.979	1.993	1.998
$\mathcal{O}(\text{Err}_{L_\infty}(q_f))$	1.449	1.733	1.891	2.024	2.379
$\mathcal{O}(\text{Err}_{L_2}(p))$	1.442	1.473	1.488	1.496	1.499
$\mathcal{O}(\text{Err}_{L_2}(q_f))$	1.338	1.459	1.495	1.391	0.459

Table 4.3: Order of convergence of the errors computed by progressively refining the space mesh.

5 | Energy in the fixed-point iterations

The goal of this chapter is to analyze the balance of energy once the fluid-protein problem has been decoupled using fixed-point iterations. Learning that the fixed-point energy decreases over time in the absence of forcing terms implies the consistency of the numerical solution with the energy behavior of the problem. Moreover, the fact that the time derivative of the fixed-point energy is bounded provides a stability estimate and a necessary condition for the convergence of the method. The mathematical steps to find the energy balance in fixed point iterations refer to those carried out in Chapter 3 for the continuous energy.

5.1. Derivation of the energy balance in fixed-point iterations

In this section our aim is to find an energy balance of the form:

$$\frac{d\mathcal{E}^{k+1}}{dt} + \mathcal{D}^{k+1} = \mathcal{F}^{k+1}, \quad (5.1)$$

where \mathcal{E}^{k+1} , \mathcal{D}^{k+1} and \mathcal{F}^{k+1} denote the energy, the dissipation and the forcing term at the $k + 1$ iteration of the fixed point method used to decouple the problem in the computational algorithm illustrated in Chapter 4. To this purpose, we need to consider the fixed-point method on the full problem (2.60) before its discretization in time via Backward Euler.

In this case fixed-point iterations read as follows:

For each k , $k \geq 0$:

Step 1: Fluid block Given $C^{(k)}(s, t)$ for $s \in (0, L)$ and $t \in (0, T)$ solve the following fluid equations:

$$\begin{cases} \frac{\partial q_f^{(k+1)}}{\partial s} + j_f^{(k+1)} = 0, \end{cases} \quad (5.2a)$$

$$\begin{cases} \frac{\rho}{\pi R^2} \frac{\partial q_f^{(k+1)}}{\partial t} = -\frac{\partial p^{(k+1)}}{\partial s} - \alpha q_f^{(k+1)}, \end{cases} \quad (5.2b)$$

$$\begin{cases} j_f^{(k+1)} = 2\pi RL_p(p^{(k+1)} - \sigma a C^{(k)}), \end{cases} \quad (5.2c)$$

to determine the functions $p^{(k+1)}(s, t)$ and $q_f^{(k+1)}(s, t)$ for $s \in (0, L)$ and $t \in (0, T)$.

Step 2: Protein block Given $q_f^{(k+1)}(s)$ for $s \in (0, L)$, $t \in (0, T)$ solve the following protein equations:

$$\begin{cases} \frac{\partial C^{(k+1)}}{\partial t} + \frac{1}{\pi R^2} \frac{\partial q_p^{(k+1)}}{\partial s} + \frac{j_p^{(k+1)}}{\pi R^2} = 0, \end{cases} \quad (5.3a)$$

$$\begin{cases} q_p^{(k+1)} = C^{(k+1)} q_f^{(k+1)} - \pi R^2 D \frac{\partial C^{(k+1)}}{\partial s}, \end{cases} \quad (5.3b)$$

$$\begin{cases} j_p^{(k+1)} = 2\pi R \frac{1-\sigma}{\sigma} P_d C^{(k+1)} \end{cases} \quad (5.3c)$$

to determine the functions $C^{(k+1)}(s)$ and $q_p^{(k+1)}(s)$ for $s \in (0, L)$ and $t \in (0, T)$.

As in previous chapters, in the blocks (5.2) and (5.3) we considered $\alpha = \frac{2\mu_w(\gamma+2)}{\pi R^4}$ and the values of the pressures and protein concentration in the tissue equal to zero.

Then, we can rewrite equation (5.3a) as done in (3.4):

$$\frac{\partial C^{(k+1)}}{\partial t} + \frac{\partial(C^{(k+1)} w^{(k+1)})}{\partial s} + \frac{j_p^{(k+1)}}{\pi R^2} = 0, \quad (5.4)$$

where we introduced the following new dependent variable:

$$w^{(k+1)} := \frac{q_f^{(k+1)}}{\pi R^2} - \frac{D}{C^{(k+1)}} \frac{\partial C^{(k+1)}}{\partial s}. \quad (5.5)$$

Replicating the steps performed in Chapter 3 at the continuous level to get the energy balance, we multiply the equations (5.2a), (5.2b) and (5.4) by the test functions $p^{(k+1)}$,

$q_f^{(k+1)}$ and $\lambda \mu^{(k+1)}$, respectively, to obtain:

$$\int_0^L \frac{\partial q_f^{(k+1)}}{\partial s} p^{(k+1)} ds = - \int_0^L j_f^{(k+1)} p^{(k+1)} ds., \quad (5.6a)$$

$$\int_0^L \frac{\rho}{\pi R^2} \frac{\partial q_f^{(k+1)}}{\partial t} q_f^{(k+1)} ds = - \int_0^L \frac{\partial p^{(k+1)}}{\partial s} q_f^{(k+1)} ds - \int_0^L \alpha (q_f^{(k+1)})^2 ds, \quad (5.6b)$$

$$\begin{aligned} & \int_0^L \lambda \frac{\partial C^{(k+1)}}{\partial t} \mu^{(k+1)} ds + \int_0^L \lambda \frac{\partial (C^{(k+1)} w^{(k+1)})}{\partial s} \mu^{(k+1)} ds + \\ & + \int_0^L \lambda \frac{j_p^{(k+1)}}{\pi R^2} \mu^{(k+1)} ds = 0. \end{aligned} \quad (5.6c)$$

In equation (5.6c) the variable $\mu^{(k+1)}$ represents the chemical potential at the $k+1$ iteration of the fixed point method, and can be defined as follows:

$$\mu^{(k+1)} := K_B T \ln \left(\frac{C^{(k+1)}}{C_{ref}} \right), \quad (5.7)$$

where K_B denotes the Boltzmann constant ($J K^{-1}$), T is the temperature (K) and C_{ref} is a reference concentration ($g cm^{-3}$). Note that for the partial derivatives of the potential in space and time we have analogous relationships to those in equations (3.13a) and (3.13b) in Chapter 3, namely:

$$\frac{\partial \mu^{(k+1)}}{\partial s} = K_B T \frac{1}{C^{(k+1)}} \frac{\partial C^{(k+1)}}{\partial s}, \quad (5.8a)$$

$$\frac{\partial \mu^{(k+1)}}{\partial t} = K_B T \frac{1}{C^{(k+1)}} \frac{\partial C^{(k+1)}}{\partial t}. \quad (5.8b)$$

The only difference is that in equations (5.8a) and (5.8b) the variables are considered at iteration $k+1$ of the fixed-point method. The same reasoning can be applied to integral equations (5.6a), (5.6b) and (5.6c) that correspond to equations (3.10), (3.6) and (3.14) in Chapter 3, respectively, differing from them only by the superscript $k+1$ on the problem variables. For this reason, by repeating exactly the same mathematical procedure as in Chapter 3, we derive the following fixed-point energy balance equation:

$$\begin{aligned} & \frac{d}{dt} (\mathcal{E}_1^{(k+1)} + \mathcal{E}_2^{(k+1)}) + \mathcal{D}_1^{(k+1)} + \mathcal{D}_2^{(k+1)} = \mathcal{F}_1^{(k+1)} + \mathcal{F}_2^{(k+1)} + \mathcal{F}_3^{(k+1)} \\ & - \int_0^L p^{(k+1)} j_f^{(k+1)} ds + \frac{\lambda K_B T}{\pi R^2} \int_0^L C^{(k+1)} j_f^{(k+1)} ds - \int_0^L \lambda \frac{j_p^{(k+1)}}{\pi R^2} \mu^{(k+1)} ds. \end{aligned} \quad (5.9)$$

Equation (5.9) corresponds to equation (3.26) in Chapter 3. In (5.9) the quantities $\mathcal{E}_1^{(k+1)}$ and $\mathcal{E}_2^{(k+1)}$ are the fixed-point energies at iteration $k+1$ related to fluid and protein,

respectively:

$$\mathcal{E}_1^{(k+1)} = \frac{1}{2} \frac{\rho}{\pi R^2} \int_0^L (q_f^{(k+1)})^2 ds, \quad (5.10a)$$

$$\mathcal{E}_2^{(k+1)} = \lambda K_B T \int_0^L C^{(k+1)} \left(\ln \left(\frac{C^{(k+1)}}{C_{ref}} \right) - 1 \right) ds. \quad (5.10b)$$

Moreover, $\mathcal{D}_1^{(k+1)}$ and $\mathcal{D}_2^{(k+1)}$ in equation (5.9) denote the fixed-point dissipation terms at iteration $k + 1$ due to fluid and protein, respectively, and are expressed as follows:

$$\mathcal{D}_1^{(k+1)} = \int_0^L \alpha (q_f^{(k+1)})^2 ds, \quad (5.11a)$$

$$\mathcal{D}_2^{(k+1)} = \frac{\lambda D}{K_B T} \int_0^L C^{(k+1)} \left(\frac{\partial \mu^{(k+1)}}{\partial s} \right)^2 ds. \quad (5.11b)$$

Finally, $\mathcal{F}_1^{(k+1)}$, $\mathcal{F}_2^{(k+1)}$ and $\mathcal{F}_3^{(k+1)}$ are the fixed-point forcing terms at iteration $k + 1$:

$$\mathcal{F}_1^{(k+1)} = - \int_0^L \frac{\partial(p^{(k+1)} q_f^{(k+1)})}{\partial s} ds, \quad (5.12a)$$

$$\mathcal{F}_2^{(k+1)} = - \int_0^L \lambda \frac{\partial(C^{(k+1)} w^{(k+1)} \mu^{(k+1)})}{\partial s} ds, \quad (5.12b)$$

$$\mathcal{F}_3^{(k+1)} = \frac{\lambda K_B T}{\pi R^2} \int_0^L \frac{\partial(C^{(k+1)} q_f^{(k+1)})}{\partial s} ds. \quad (5.12c)$$

The three remaining terms in equation (5.9) are treated by substituting expressions (5.2c) and (5.3c) for $j_f^{(k+1)}$ and $j_p^{(k+1)}$, respectively. They become as follows:

$$\begin{aligned} & - \int_0^L p^{(k+1)} j_f^{(k+1)} ds + \frac{\lambda K_B T}{\pi R^2} \int_0^L C^{(k+1)} j_f^{(k+1)} ds - \int_0^L \lambda \frac{j_p^{(k+1)}}{\pi R^2} \mu ds = \\ & - \int_0^L 2\pi R L_p \left(p^{(k+1)} - \frac{\lambda K_B T}{\pi R^2} C^{(k+1)} \right) (p^{(k+1)} - \sigma a_1 C^{(k)}) ds - \\ & - \int_0^L \frac{2\lambda}{R} \frac{1-\sigma}{\sigma} P_d C^{(k+1)} \mu^{(k+1)} ds. \end{aligned} \quad (5.13)$$

We recall that in Chapter 3 we have assumed the chemical potential to be nonnegative, a property extended to the potential $\mu^{(k+1)}$ computed at the $k + 1$ iteration of the fixed-point method. Therefore, the last term in (5.13), taken to the right-hand side in equation (5.9), is nonnegative and contributes to the dissipation. This dissipation is due to the exchange of fluid and protein across the lateral surface and can be written as:

$$\mathcal{D}_{lat,1}^{(k+1)} = \int_0^L \frac{2\lambda}{R} \frac{1-\sigma}{\sigma} P_d C^{(k+1)} \mu^{(k+1)} ds. \quad (5.14)$$

Now, we can substitute in equation (5.9) the value of the multiplicative constant λ equal to $\frac{\sigma a_1 \pi R^2}{K_B T}$, the one considered in Chapter 3, and rewrite the equation as:

$$\begin{aligned} \frac{d}{dt} \mathcal{E}^{(k+1)} + \mathcal{D}^{(k+1)} &= \mathcal{F}^{(k+1)} - \\ &- \int_0^L 2\pi RL_p (p^{(k+1)} - \sigma a_1 C^{(k+1)}) (p^{(k+1)} - \sigma a_1 C^{(k)}) ds, \end{aligned} \quad (5.15)$$

where the energy, the dissipation and the forcing term are given by the following expressions:

$$\mathcal{E}^{(k+1)} = \mathcal{E}_1^{(k+1)} + \mathcal{E}_2^{(k+1)}, \quad (5.16a)$$

$$\mathcal{D}^{(k+1)} = \mathcal{D}_1^{(k+1)} + \mathcal{D}_2^{(k+1)} + \mathcal{D}_{lat,1}^{(k+1)}, \quad (5.16b)$$

$$\mathcal{F}^{(k+1)} = \mathcal{F}_1^{(k+1)} + \mathcal{F}_2^{(k+1)} + \mathcal{F}_3^{(k+1)}. \quad (5.16c)$$

Dealing with the last term in the equation (5.15) is nontrivial because both the concentration at iteration k and the concentration at iteration $k + 1$ of the fixed-point method appear and usually these functions are not equal. The procedure for tackling this problem consists of adding and subtracting the term $\int_0^L 2\pi RL_p (p^{(k+1)} - \sigma a_1 C^{(k+1)})^2 ds$ as follows:

$$\begin{aligned} \frac{d}{dt} \mathcal{E}^{(k+1)} + \mathcal{D}^{(k+1)} &= \mathcal{F}^{(k+1)} - \\ &- \int_0^L 2\pi RL_p (p^{(k+1)} - \sigma a_1 C^{(k+1)}) (p^{(k+1)} - \sigma a_1 C^{(k)}) ds + \\ &+ \int_0^L 2\pi RL_p (p^{(k+1)} - \sigma a_1 C^{(k+1)})^2 ds - \int_0^L 2\pi RL_p (p^{(k+1)} - \sigma a_1 C^{(k+1)})^2 ds, \end{aligned} \quad (5.17)$$

Applying simple algebra to equation (5.17) yields:

$$\begin{aligned} \frac{d}{dt} \mathcal{E}^{(k+1)} + \mathcal{D}^{(k+1)} + \int_0^L 2\pi RL_p (p^{(k+1)} - \sigma a_1 C^{(k+1)})^2 ds &= \mathcal{F}^{(k+1)} + \\ &+ \int_0^L 2\pi RL_p (p^{(k+1)} - \sigma a_1 C^{(k+1)}) (\sigma a_1 C^{(k)} - \sigma a_1 C^{(k+1)}) ds. \end{aligned} \quad (5.18)$$

The third term of (5.18) being nonnegative, contributes to the lateral dissipation and can be denoted as:

$$\mathcal{D}_{lat,2}^{(k+1)} = \int_0^L 2\pi RL_p (p^{(k+1)} - \sigma a_1 C^{(k+1)})^2 ds. \quad (5.19)$$

Then, we can write equation (5.18) as:

$$\begin{aligned} \frac{d}{dt} \mathcal{E}^{(k+1)} + \mathcal{D}^{(k+1)} &= \mathcal{F}^{(k+1)} + \\ &+ \int_0^L 2\pi RL_p (p^{(k+1)} - \sigma a_1 C^{(k+1)}) (\sigma a_1 C^{(k)} - \sigma a_1 C^{(k+1)}) ds, \end{aligned} \quad (5.20)$$

where $\mathcal{D}^{(k+1)} = \mathcal{D}_1^{(k+1)} + \mathcal{D}_2^{(k+1)} + \mathcal{D}_{lat,1}^{(k+1)} + \mathcal{D}_{lat,2}^{(k+1)}$. The last term in (5.20) is treated using Hölder's inequality as follows:

$$\begin{aligned} \int_0^L 2\pi RL_p (p^{(k+1)} - \sigma a_1 C^{(k+1)}) (\sigma a_1 C^{(k)} - \sigma a_1 C^{(k+1)}) ds &\leq \\ \leq 2\pi RL_p \left(\int_0^L (p^{(k+1)} - \sigma a_1 C^{(k+1)})^2 ds \right)^{\frac{1}{2}} &\left(\int_0^L (\sigma a_1 C^{(k)} - \sigma a_1 C^{(k+1)})^2 ds \right)^{\frac{1}{2}} \quad (5.21) \\ \leq 2\pi RL_p L \sigma a_1 \| (p^{(k+1)} - \sigma a_1 C^{(k+1)}) \|_{L^2(0,L)} \| (C^{(k)} - C^{(k+1)}) \|_\infty. \end{aligned}$$

Therefore, the final form of the fixed point energy balance can be stated as:

$$\begin{aligned} \frac{d}{dt} \mathcal{E}^{(k+1)} + \mathcal{D}^{(k+1)} &\leq \mathcal{F}^{(k+1)} + \\ &+ 2\pi RL_p L \sigma a_1 \| (p^{(k+1)} - \sigma a_1 C^{(k+1)}) \|_{L^2(0,L)} \| (C^{(k)} - C^{(k+1)}) \|_\infty. \end{aligned} \quad (5.22)$$

We note that equation (5.22) is not a real balance, but an inequality. We discuss the role of this inequality in the next section.

5.2. Decrease in energy over time is a necessary condition for convergence

The dissipation term in (5.22) is nonnegative and therefore the equation can be rewritten as:

$$\begin{aligned} \frac{d}{dt} \mathcal{E}^{(k+1)} &\leq \mathcal{F}^{(k+1)} + \\ &+ 2\pi RL_p L \sigma a_1 \| (p^{(k+1)} - \sigma a_1 C^{(k+1)}) \|_{L^2(0,L)} \| (C^{(k)} - C^{(k+1)}) \|_\infty. \end{aligned} \quad (5.23)$$

When fixed-point iterations reach convergence, we have that the error $err_C^{(k)}$, in equation (4.14) at Step 4 of the computational algorithm described in Chapter 4, tends to zero and thus:

$$\| (C^{(k)} - C^{(k+1)}) \|_\infty \rightarrow 0. \quad (5.24)$$

The convergence of fixed-point method, which is equivalent to the limit in (5.24), implies that the term in the box in equation (5.23) cancels out, and makes the equation (5.23) become:

$$\frac{d}{dt}\mathcal{E}^{(k+1)} \leq \mathcal{F}^{(k+1)}. \quad (5.25)$$

Summing up, in the absence of forcing terms, the decrease in energy over time is a necessary condition for convergence of the fixed-point method, which written in mathematical words is:

$$\| (C^{(k)} - C^{(k+1)}) \|_{\infty} \rightarrow 0 \implies \frac{d}{dt}\mathcal{E}^{(k+1)} \leq 0. \quad (5.26)$$

For this reason, let us analyze the time behavior of the energy computed through the numerical solution resulting from the computational algorithm illustrated in Chapter 4, in the absence of forcing term, namely with zero boundary conditions. More specifically, at each time step n we compute the energy $\mathcal{E}^{(conv)}$ as the sum of the portions due to the fluid (Eq. (5.10a)) and due to the proteins (Eq. (5.10b)):

$$\mathcal{E}^{(conv)} = \frac{1}{2} \frac{\rho}{\pi R^2} \int_0^L (q_f^{(conv)})^2 ds + \lambda K_B T \int_0^L C^{(conv)} \left(\ln \left(\frac{C^{(conv)}}{C_{ref}} \right) - 1 \right) ds. \quad (5.27)$$

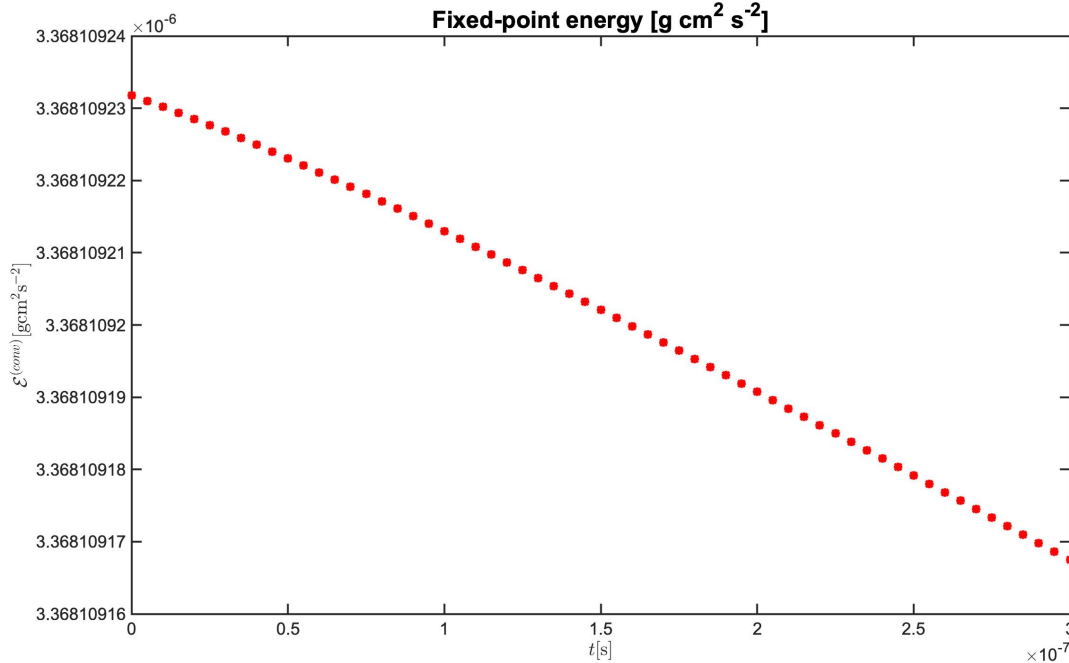


Figure 5.1: Fixed-point energy plotted over time. The energy is computed at each time step n , starting from the numerical solution once the fixed-point method has reached convergence.

The axial volumetric flow rate $q_f^{(conv)}$ and concentration $C^{(conv)}$ variables used in equation (5.27) to compute the energy at each time step n are those corresponding to convergence of the fixed-point iteration. Moreover, the integrals in (5.27) are calculated using the trapezoidal quadrature rule. The plot of energy $\mathcal{E}^{(conv)}$ (y axis) over time t (x axis) is shown in Figure 5.1. Figure 5.1 proves the decrease in energy over time, and is consistent with the findings of this chapter. Furthermore, the fact that the energy remains bounded, in absence of forcing terms, is a strong evidence for the stability of our numerical algorithm. Indeed, if the solution suffered from instability or unphysical oscillation, the energy would also be affected. Instead, the behavior recorded in Figure 5.1 is coherent with the physical problem.

6 | Simulations in physiological and pathological conditions

In this chapter we present some results of physiological interest obtained by solving the model of fluid and protein transport, described in equations (2.60), using the computational algorithm illustrated in Chapter 4. The main focus of this chapter is on fluid and protein fluxes across the membrane, which are the most immediate markers of the interstitial edema. We recall that the causes of this pathological condition are typically alterations in hydrostatic and osmotic pressures, changes in the structure of the membrane, which manifest as variations in hydraulic conductivity L_p and osmotic reflection coefficient σ , or disturbances in the lymphatic outflow system. In particular, with our model it is easy to study structural alterations of the membrane. Indeed, we can examine how a variation in the parameters σ and L_p impacts the model variables, hydrostatic and osmotic pressures, protein concentration, but most importantly lateral volumetric and mass flow rates. All the results presented in this chapter consider a time interval of 300 s, which is long enough to visualize the consequences of parameter variation. Moreover, as in the previous chapters, we assume the values of hydrostatic pressure p_t , the osmotic pressure π_t and the protein concentration C_t in the tissue outside of the vessel equal to zero, according to the specific experimental conditions adopted in [5] for the stationary model. Concerning the computational domain, the first three sections examine the arterial capillary number 1 of the microvascular network analyzed in [5], already considered for the results shown in Chapter 4. Therefore, the physical dimensions and physiological parameters are those given in Table 4.1. Specifically, in Section 6.1 we present the simulation of the nonpathological case in which all parameters remain constant at basal values, in Section 6.2 we simulate the pathological case given by a sudden decrease in the reflection coefficient σ , and in Section 6.3 we show how an increase in protein in the capillary can avoid the edema condition presented in the previous section. Finally, in Section 6.4 we examine the effect of the Atrial natriuretic peptide (ANP) on the venular capillary number 10 of the microvascular network analyzed in [5]. This hormone increases the value of hydraulic conductivity L_p promoting fluid reabsorption, which is already pre-

dominant in the venular capillaries. Therefore, ANP action is an additional method of treating edema.

6.1. Nonpathological scenario

We start by examining the nonpathological scenario. Under normal conditions, the movement of fluid in the vessel is governed by a hydrostatic pressure gradient. In order to simulate this phenomenon, we impose constant boundary conditions $p(0, t) = 5 \text{ cmH}_2\text{O}$ and $p(L, t) = 15 \text{ cmH}_2\text{O}$ for $t \in (0, T)$ and a linear hydrostatic pressure as initial condition. As far as protein concentration is concerned, we set both boundary conditions $C(0, t)$ and $C(L, t)$, as well as initial concentration $C(s, 0)$ equal to 0.025 g cm^{-3} , constant over time and space, respectively. This choice agrees with the real basal value for concentration assumed also by the authors of [5] for the stationary model. In the nonpathological scenario the parameters of the model (2.60) are set constant over time, in particular the reflection coefficient σ and the hydraulic conductivity L_p are equal to their basal values of 0.8 and $1.5 \cdot 10^{-7} \text{ cm s}^{-1} \text{ cmH}_2\text{O}^{-1}$, respectively (see Table 4.1 for reference). Under these conditions, the shape of the hydrostatic pressure over time remains linear, whereas the concentration remains constant and equal to its initial value, as can be seen in Figure 6.1, where selected snapshots of the numerical solution for hydrostatic pressure and concentration are shown. As anticipated at the end of Chapter 2, the reason why in healthy conditions no substantial changes in pressure and concentration occur over time is due to the basal value of 0.8 of the reflection coefficient σ . This value results in an amount of protein exiting the capillary every second equal to $3.57 \cdot 10^{-13} \text{ g}$ (see the plot of the total lateral mass flow rate J_p shown in Figure 6.2). Thus, the number of protein moving across the membrane is orders of magnitude smaller than the concentration of protein within the vascular space, considering that in our case the total amount of protein inside the capillary can be estimated as follows:

$$m_{\text{prot}} = C(\pi R^2 L) = (0.025 \text{ g cm}^{-3}) \pi (1 \cdot 10^{-3} \text{ cm})^2 (0.0535 \text{ cm}) = 4.2 \cdot 10^{-9} \text{ g}. \quad (6.1)$$

As a consequence, the protein concentration remains constant and protein flux has a negligible influence on the distribution of the osmotic pressure π . The result is that also the shape of the specific lateral volumetric flow rate j_f , which we recall is expressed by the relationship (2.60e), remains constant over time (Figure 6.3). Therefore, there is no impact on the axial volumetric flow rate q_f and the fluid dynamics remains unchanged over time. These outcomes are not expected under conditions where the reflection coefficient σ is closer to 0, as would occur in inflammation, sepsis, or vascular remodelling. This scenario

is examined in the next section. In particular, the results show that, under pathological conditions, simulated with a sudden decrease in the reflection coefficient σ , the protein flux into the tissue can indeed be of sufficient magnitude to induce a gradient in osmotic pressure. In this scenario, both fluid and protein accumulate into the tissue causing the pathological condition of interstitial edema. Before proceeding, let us make some final remarks on Figures 6.2 and 6.3. Figure 6.2 represents the two lateral volumetric and mass flow rates over time. These quantities are the amount of fluid and protein leaving the capillary per unit time, and in the absence of parameter changes or pressure alterations we expect them to remain constant. Figure 6.3 represents three selected time snapshots of the specific lateral volumetric and mass flow rate. These quantities are the amount of fluid and protein exiting the membrane per unit length and time. With the assumption that pressures are zero in the tissue, the equation (2.60e) for the specific lateral volumetric flow rate j_f simplifies as follows:

$$j_f = 2\pi R L_p(p - \sigma\pi), \quad s \in (0, L), t \in (0, T). \quad (6.2)$$

Therefore, since the value of concentration C in the capillary remains constant and so does the osmotic pressure π , since we recall that relation (2.29) applies, then the linear shape of j_f reflects that of hydrostatic pressure p , rescaled by the coefficient $-\sigma\pi$. This behavior can be appreciated by comparing the two plots at the top of Figures 6.1 and 6.3. The specific volumetric flow rate j_f intersects the zero level (red dotted line in Figure 6.3). The point of intersection is the so called Starling equilibrium (see [7]), a physical condition of balance between the hydrostatic and osmotic pressure differences, characterising fluid exchange. To the right of this point we observe the phenomenon of fluid filtration (fluid leaves the capillary), while to the left reabsorption occurs (fluid enters the capillary). Finally, the specific mass flow rate j_p , whose plot is shown at the bottom of Figure 6.3 remains constant in space reflecting the behavior of concentration C , in agreement with Equation (2.60f).

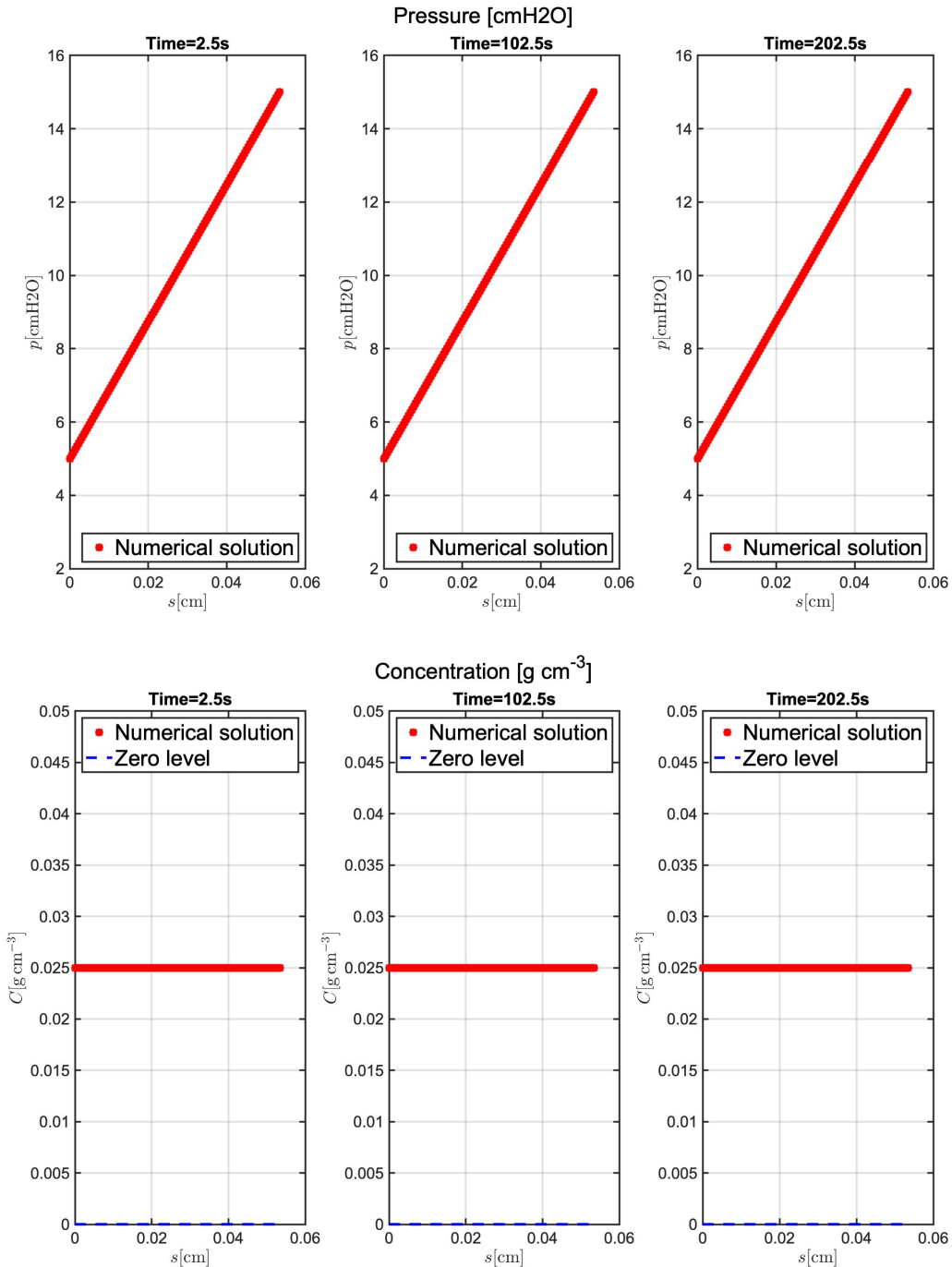


Figure 6.1: Visualization in the nonpathological case of hydrostatic pressure p (top row) and protein concentration C (bottom row) plotted in space at three different time instants ($T_1 = 2.5\text{ s}$, $T_2 = 102.5\text{ s}$ and $T_3 = 202.5\text{ s}$). Under normal conditions, the shape of the hydrostatic pressure p over time remains linear, whereas the protein concentration C remains constant and equal to the basal value of 0.025 g cm^{-3} .

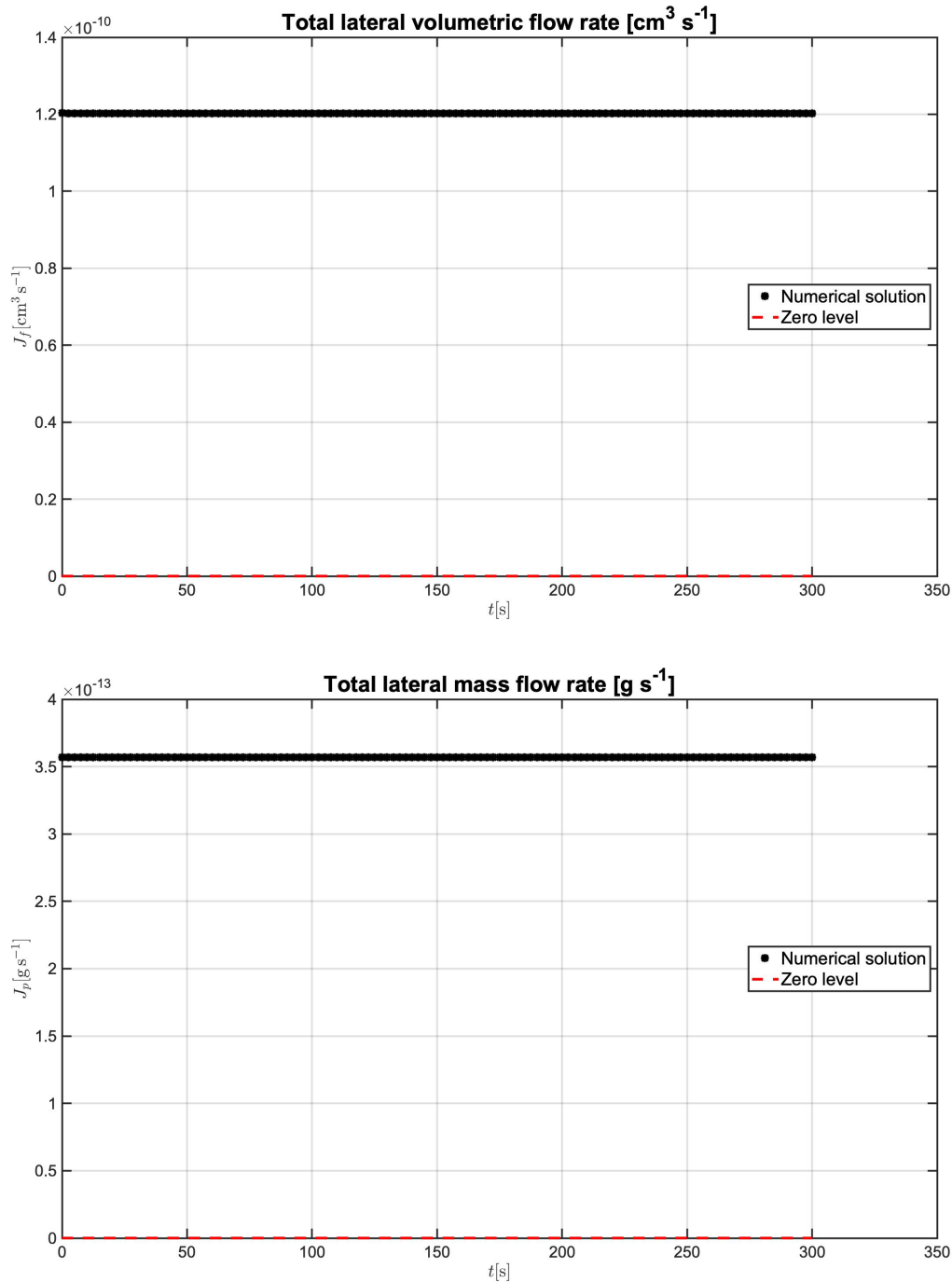


Figure 6.2: Visualization in the nonpathological case of total lateral volumetric flow rate J_f (top) and total lateral mass flow rate J_p (bottom) plotted in time. Under normal conditions, they remain constant over time. The positive value of J_f indicates that fluid filtration dominates over reabsorption, as expected in an arterial capillary. The low value of J_p means that in the nonpathological case the protein flux is negligible.

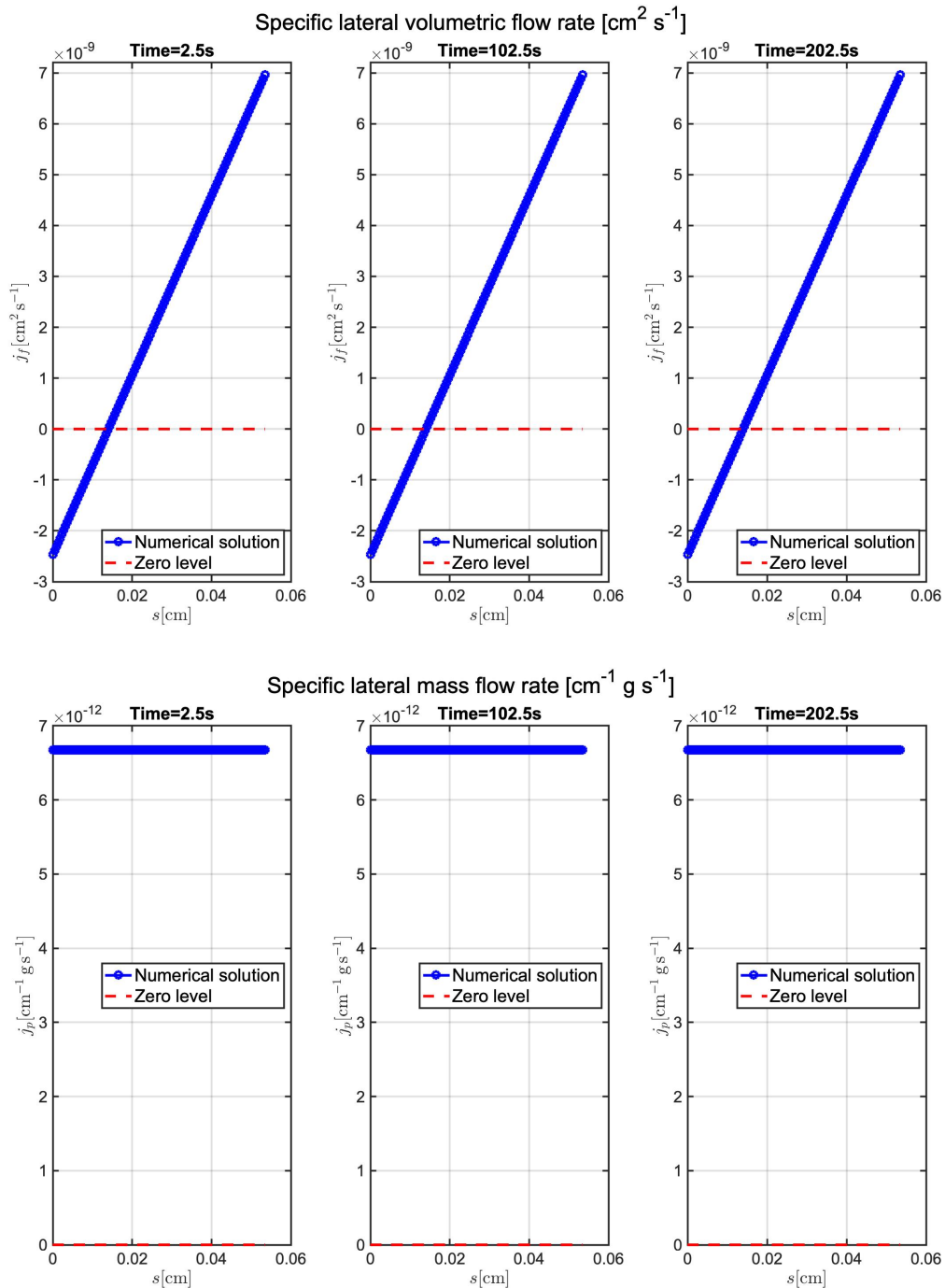


Figure 6.3: Visualization in the nonpathological case of specific lateral volumetric flow rate j_f (top row) and specific lateral mass flow rate j_p (bottom row) plotted in space at three different time instants ($T_1 = 2.5\text{ s}$, $T_2 = 102.5\text{ s}$ and $T_3 = 202.5\text{ s}$). Under normal conditions, the shape of j_f remains linear over time, whereas j_p remains constant, reflecting the behaviour of concentration C . The point of intersection between j_f (circled blue line) and the zero level (red dotted line) is the so called Starling equilibrium, a physical condition of balance between the hydrostatic and osmotic pressure differences.

6.2. Pathological scenario with sudden decrease in reflection coefficient

In this section we simulate the pathological scenario corresponding to a sudden decrease in the reflection coefficient σ . This change causes the inability of the membrane to retain proteins within the vascular space and manifests as a leakage of both protein and fluid into the tissue, leading to edema. For the purpose of simulating this condition, we change the reflection coefficient σ over time as shown in Figure 6.4. Namely, at the midpoint of the time interval, σ undergoes a sudden decrease from the basal value of 0.8 to the pathological value of 0.01.

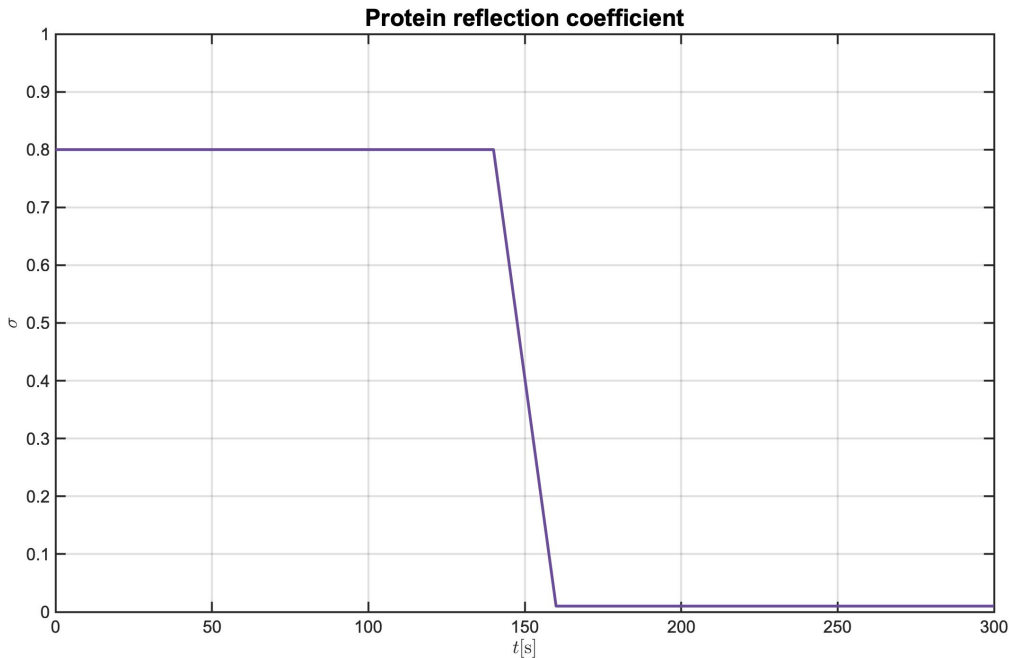


Figure 6.4: Visualization over time of the protein reflection coefficient σ assumed in the pathological scenario in which sudden structural membrane changes occur. At the midpoint of the time interval, σ undergoes a sudden decrease from the basal value of 0.8 to the pathological value of 0.01.

In this pathological scenario, we set the same boundary and initial conditions as in Section 6.1 for the hydrostatic pressure. In contrast, with regard to the concentration C , the initial condition remains constant at the basal value of 0.025 g cm^{-3} , while the boundary conditions require further consideration. More specifically, we should think of the capillary as being included in a microvascular network made up of other vessels that are

affected by the same decrease in σ . When σ is equal to 0.01 they lose an amount of protein per unit area and time equal to the specific lateral mass flow rate j_p , which we recall to be easily computed using the relation (2.60f). Therefore, the values of C at the endpoints are assumed to be equal to those of the concentrations in the vessels around the capillary adopted in our simulation. In light of this reasoning, the concentration boundary conditions are constant as long as σ remains equal to its basal value, and decrease linearly over time with a rate equal to $j_p S_{lat}$ once the pathological membrane alteration occurs (S_{lat} denoting the lateral surface of the capillary). Obviously, in the future, a more comprehensive vascular network non stationary model will include neighboring capillaries and will not require this approximation for boundary conditions.

Let us now analyze the results. Hydrostatic pressure p (shown at the top of Figure 6.5) remains linear over time as in the nonpathological case in Section 6.1. The concentration C (bottom of Figure 6.5) decreases over time due to the proteins that flow into the tissue. This protein flux influences osmotic pressure π and causes an increase in fluid flow in the tissue from a rate of $1.2 \cdot 10^{-10} \text{ cm}^{-3} \text{ s}^{-1}$ to $5 \cdot 10^{-10} \text{ cm}^{-3} \text{ s}^{-1}$ (see J_f at the top of Figure 6.6). The consequence is the condition of interstitial edema with all the damages described in Chapter 1. The lateral mass flow rate J_p (bottom of Figure 6.6) undergoes a huge increase from $3.57 \cdot 10^{-13} \text{ g s}^{-1}$ in the nonpathological scenario studied in Section 6.1 to a value of $1.34 \cdot 10^{-10} \text{ g s}^{-1}$. As expected, once this increase of 3 orders of magnitude is recorded, J_p decreases slightly, since less protein remains in the vascular space. The numerical solution meets this behavior. Similar reasoning applies to the plot of the specific lateral mass flow rate j_p at the bottom of Figure 6.7. Finally, looking at the specific lateral volumetric flow rate j_f at the top of Figure 6.7, it can be noted that the capillary switches from filtration and reabsorption mode to filtration-only action, with the loss of the Starling equilibrium point.

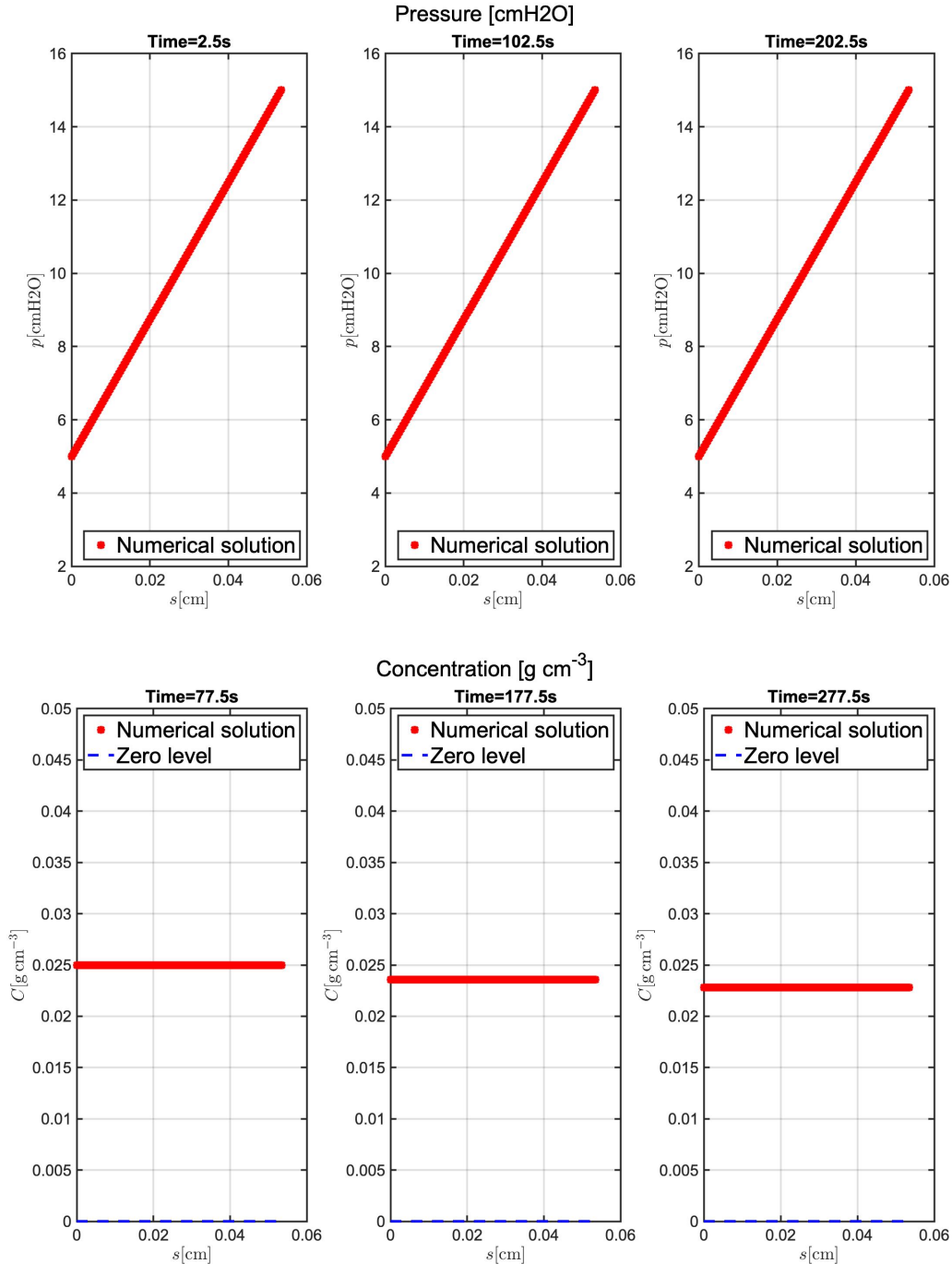


Figure 6.5: Visualization in the pathological case of hydrostatic pressure p (top row) and protein concentration C (bottom row) plotted in space at three different time instants ($T_1 = 2.5\text{ s}$, $T_2 = 102.5\text{ s}$ and $T_3 = 202.5\text{ s}$). Hydrostatic pressure p remains linear over time, as in the nonpathological case, whereas the concentration C decreases over time due to protein flow into the tissue.

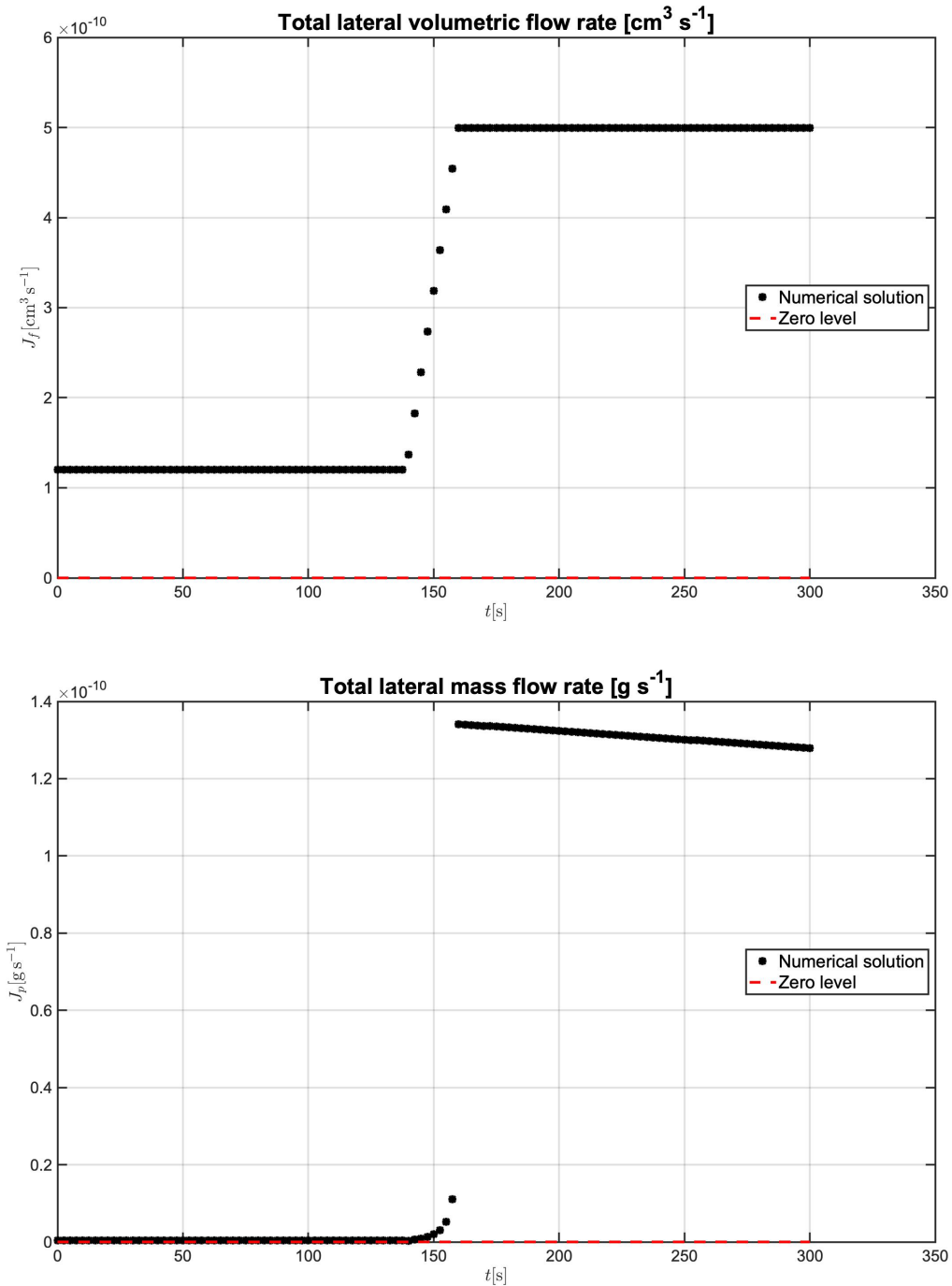


Figure 6.6: Visualization in the pathological case of total lateral volumetric flow rate J_f (top) and total lateral mass flow rate J_p (bottom) plotted in time. J_f increases from a rate of $1.2 \cdot 10^{-10} \text{ cm}^{-3} \text{s}^{-1}$ to $5 \cdot 10^{-10} \text{ cm}^{-3} \text{s}^{-1}$, because of the osmotic gradient generated by the protein flow into the tissue. J_p undergoes a huge increase from $3.57 \cdot 10^{-13} \text{ g s}^{-1}$ to a value of $1.34 \cdot 10^{-10} \text{ g s}^{-1}$. As expected, once this increase of 3 orders of magnitude is recorded, J_p decreases slightly, since a lower amount of protein remains in the vascular space.

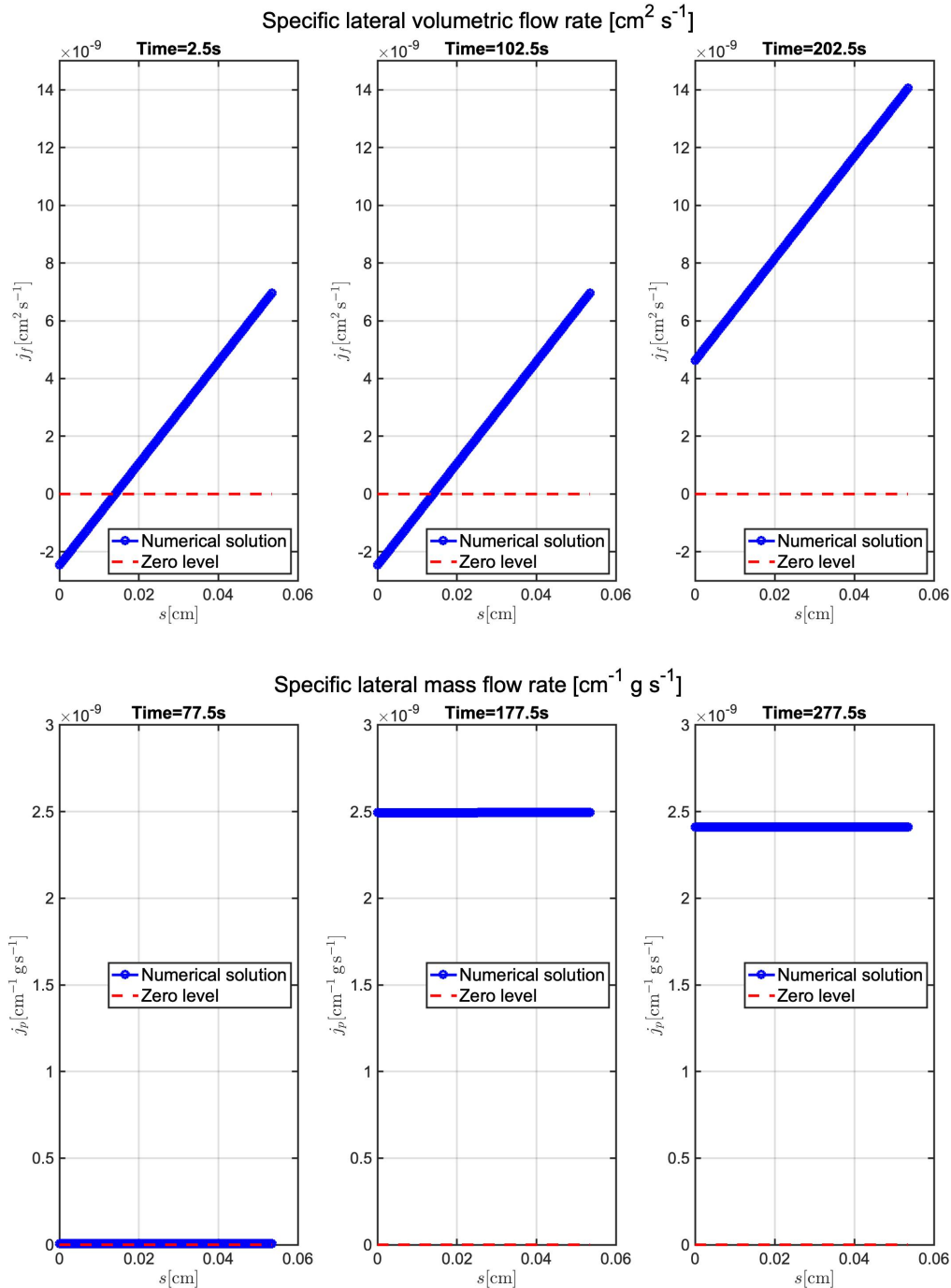


Figure 6.7: Visualization in the pathological case of specific lateral volumetric flow rate j_f (top row) and specific lateral mass flow rate j_p (bottom row) plotted in space at three different time instants ($T_1 = 2.5\text{ s}$, $T_2 = 102.5\text{ s}$ and $T_3 = 202.5\text{ s}$). After σ decreases, the Starling equilibrium point, intersection between j_f (circled blue line) and the zero level (red dotted line), is lost and the capillary switches from filtration and reabsorption mode to filtration-only action. Concerning j_p , it increases suddenly due to the structural membrane changes and then decreases slightly over time, since a lower amount of protein remains in the vascular space.

6.3. Increasing protein concentration in the capillary may prevent edema condition

In this section, we propose an option to limit the fluid flow into the tissue leading to the edema condition, simulated with the sudden decrease of the reflection coefficient σ , as seen in Section 6.2. Our goal is to limit the growth of the lateral volumetric flow rate J_f (see Figure 6.6), occurring due to the osmotic gradient established as a result of the increased concentration in the tissue and the depletion of proteins in the vascular space. The idea is to rebalance the osmotic pressures acting across the microvascular walls by injecting new proteins inside the capillary. To produce this effect we can act on the boundary conditions. Specifically, we simulate an increase in the boundary value of the concentration equal to 70 times the basal value. We chose to place this protein injection after 175 s, as a replica to the pathological membrane change which occurs after 150 s (Figure 6.4). Figure 6.8 shows the time evolution of the boundary conditions for concentration set at the endpoints of the domain. They are the only change we make in this simulation with respect to the pathological case in Section 6.2.

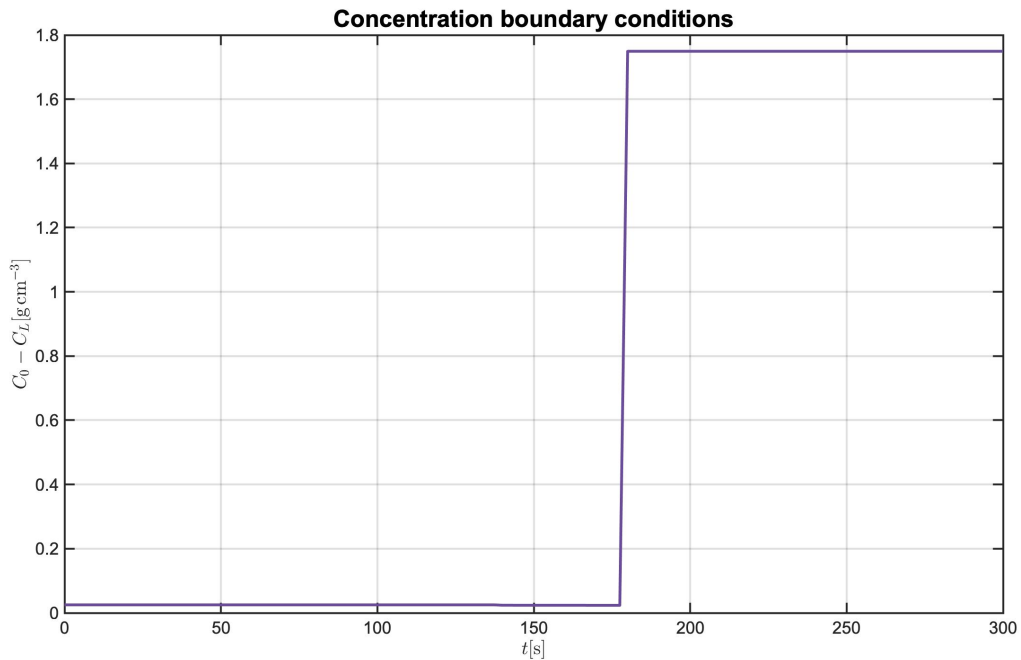


Figure 6.8: Visualization over time of the concentration boundary conditions $C(0, t)$ and $C(L, t)$. They increase 70 times higher than the basal value after 175 s, as a treatment to the pathological membrane change which occurs after 150 s.

Analyzing the results, it can be seen that the lateral volumetric flow rate J_f (shown at the top of Figure 6.9), after rising to pathological levels, is lowered when the increase in concentration in the capillary takes place. Clearly, the injection of protein into the capillary also leads to an increase in the lateral mass flow rate J_p compared to the pure pathological case where no actions were taken (bottom of Figure 6.9). The same results can be seen in Figure 6.10 where the specific lateral volumetric and mass flow rate are reported. It is of interest to note how with this treatment for the edema condition, the Starling point is recovered, see the behaviour of j_f at the top of Figure 6.10 compared with Figure 6.7 in the previous section.

6.4. Atrial natriuretic peptide increases hydraulic conductivity promoting fluid reabsorption in venular capillaries

Up to now, we have adopted for simulations an arterial capillary in which, under normal conditions, fluid filtration dominates over reabsorption (see Figure 6.3). However, in a microvascular network there are usually also venular capillaries, whose major role is reabsorption, as can be seen in Figure 6.12, where we show both the specific and total lateral volumetric flow rate across the membrane of a venular capillary under normal conditions. We note that in this case more fluid enters than exits, and the total volumetric flow rate over time is negative. Specifically, for this simulation and for all the results shown in this section, we refer to the venular capillary number 10 of the microvascular network analyzed in [5]. Its physical dimensions are a length of $37.5 \mu m$ and a radius of $321.2 \mu m$. According to the experiments reported in [10], the venular capillaries are those that exhibit greater sensitivity to the Atrial natriuretic peptide (ANP), a hormone involved in homeostatic control. In fact, the data collected in [10] prove that the presence of this hormone induces an approximately twofold increase in hydraulic conductivity L_p for venular capillary, whereas less than 25% of arterial capillaries exhibit such a response. For this reason, ANP could play a key role in the treatment of interstitial edema by increasing fluid reabsorption in venular capillaries. In our thesis, we analyze how the volumetric lateral flow rate in a venular capillary may change when hydraulic conductivity doubles over time. For the simulation we consider all parameters constant at their basal values, and the change in hydraulic conductivity shown in Figure 6.11, where L_p , starting from the venular capillary basal value of $5 \cdot 10^{-7} cm s^{-1} cm H_2O^{-1}$, suddenly increases at the midpoint of the time interval reaching a value of $10 \cdot 10^{-7} cm s^{-1} cm H_2O^{-1}$. The lateral volumetric flow rate J_f at the bottom of Figure 6.13 shows how the capillary absorbs about twice as

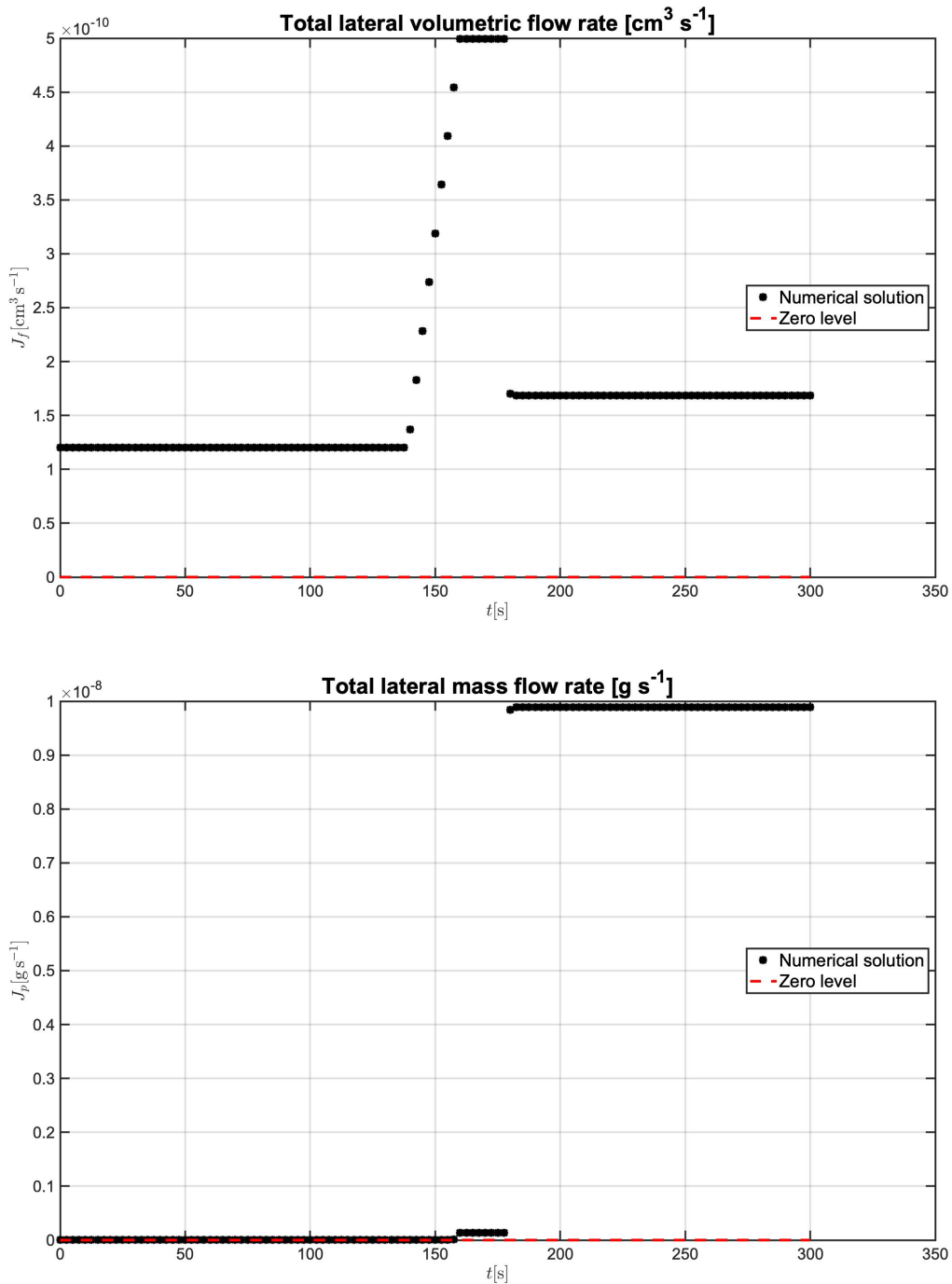


Figure 6.9: Visualization of the time evolution of total lateral volumetric flow rate J_f (top) and total lateral mass flow rate J_p (bottom), in the case where new proteins are injected inside the capillary. The lateral volumetric flow rate J_f rises to pathological levels before being scaled down by the injection of protein in the capillary. The lateral mass flow J_p increases compared to the pathological case where no actions were taken.

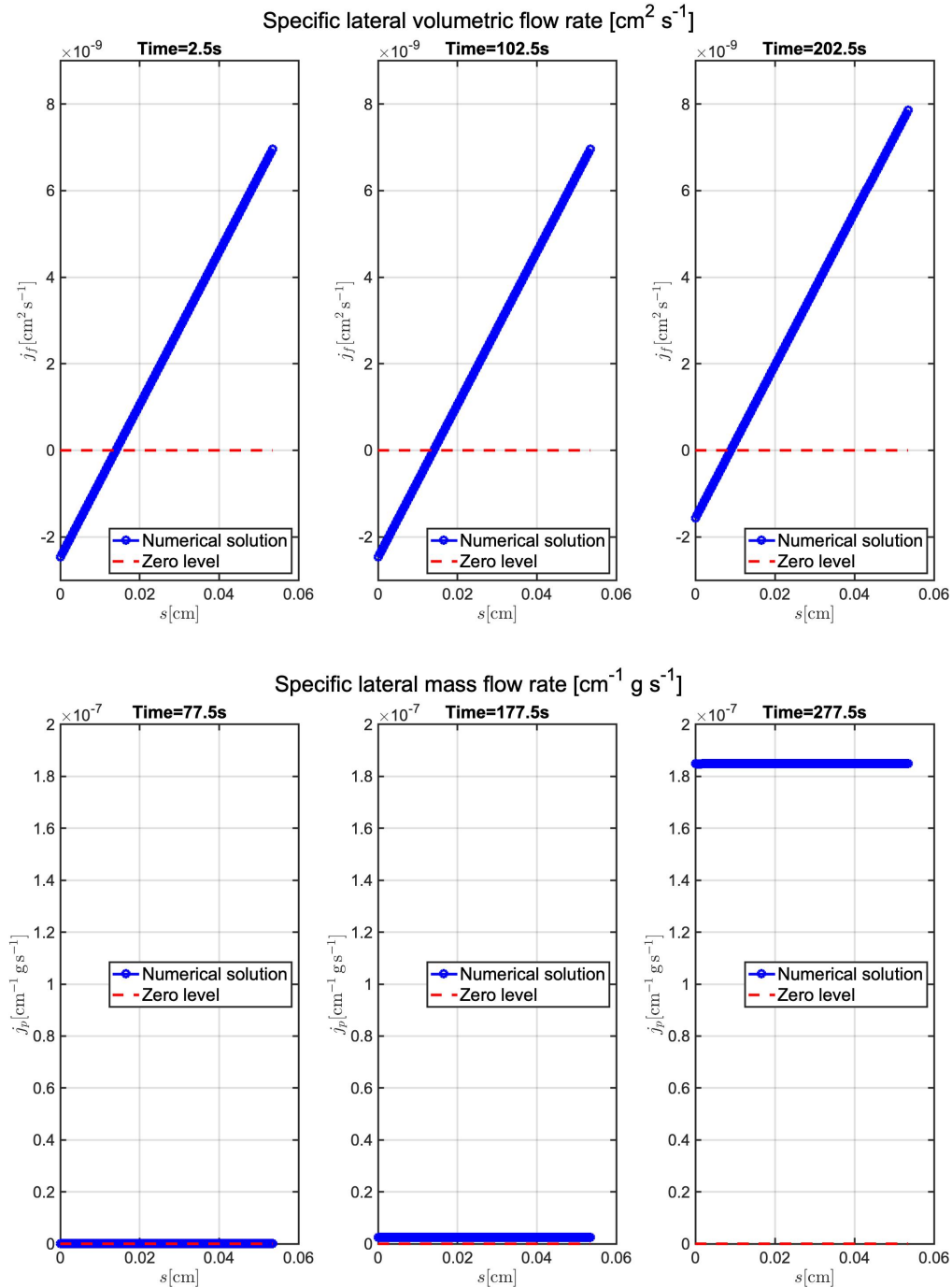


Figure 6.10: Visualization of the spatial profile of the lateral volumetric flow rate j_f (top row) and lateral mass flow rate j_p (bottom row) at three different time instants ($T_1 = 2.5\text{ s}$, $T_2 = 102.5\text{ s}$ and $T_3 = 202.5\text{ s}$), in the case where new proteins are injected inside the capillary. The Starling equilibrium point, intersection between j_f (circled blue line) and the zero level (red dotted line), is recovered with respect to the pathological case shown in Figure 6.7. The specific lateral mass flow j_p increases over time, while remaining constant in space.

amount of fluid, once the Atrial natriuretic peptide has increased hydraulic conductivity L_p . Moreover, the slope of the specific lateral volumetric flow rate j_f becomes steeper, in accordance with relationship (2.60e).

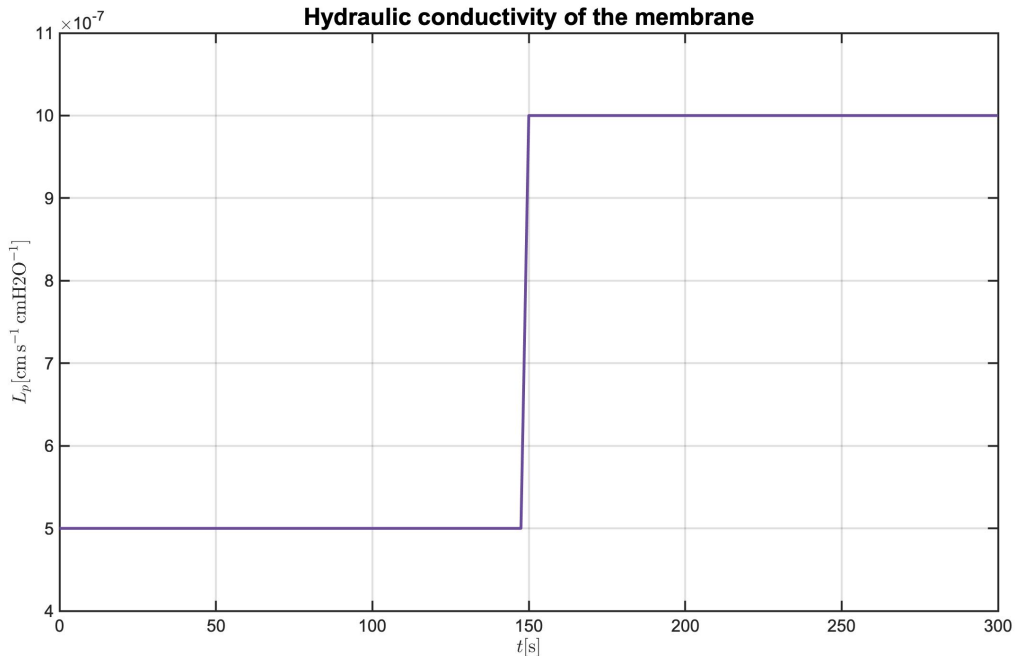


Figure 6.11: Visualization over time of the hydraulic conductivity L_p , which subjected to the action of the Atrial natriuretic peptide, increases twofold from the basal value of $5 \cdot 10^{-7} \text{ cm s}^{-1} \text{cmH}_2\text{O}^{-1}$, assumed for venular capillaries.

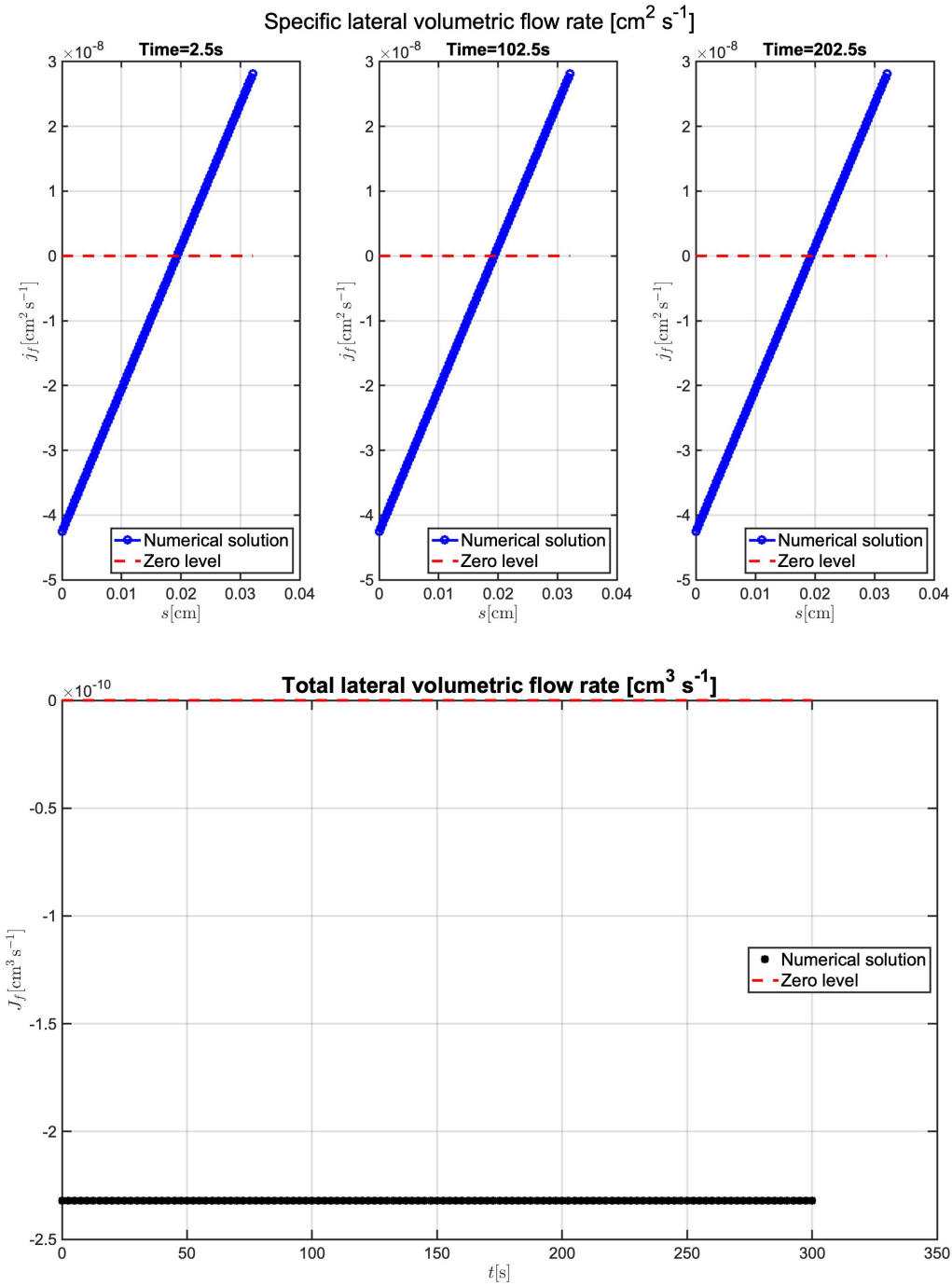


Figure 6.12: Visualization in the nonpathological case of specific lateral volumetric flow rate j_f (three time snapshots at the top) and of total lateral volumetric flow rate J_f (plotted as a function of time, bottom). In a venular capillary reabsorption dominates over fluid filtration. Indeed the Starling equilibrium point, intersection between j_f (circled blue line) and the zero level (red dotted line), is to the right of the vessel midpoint and the total volumetric flow rate J_f is negative over time.

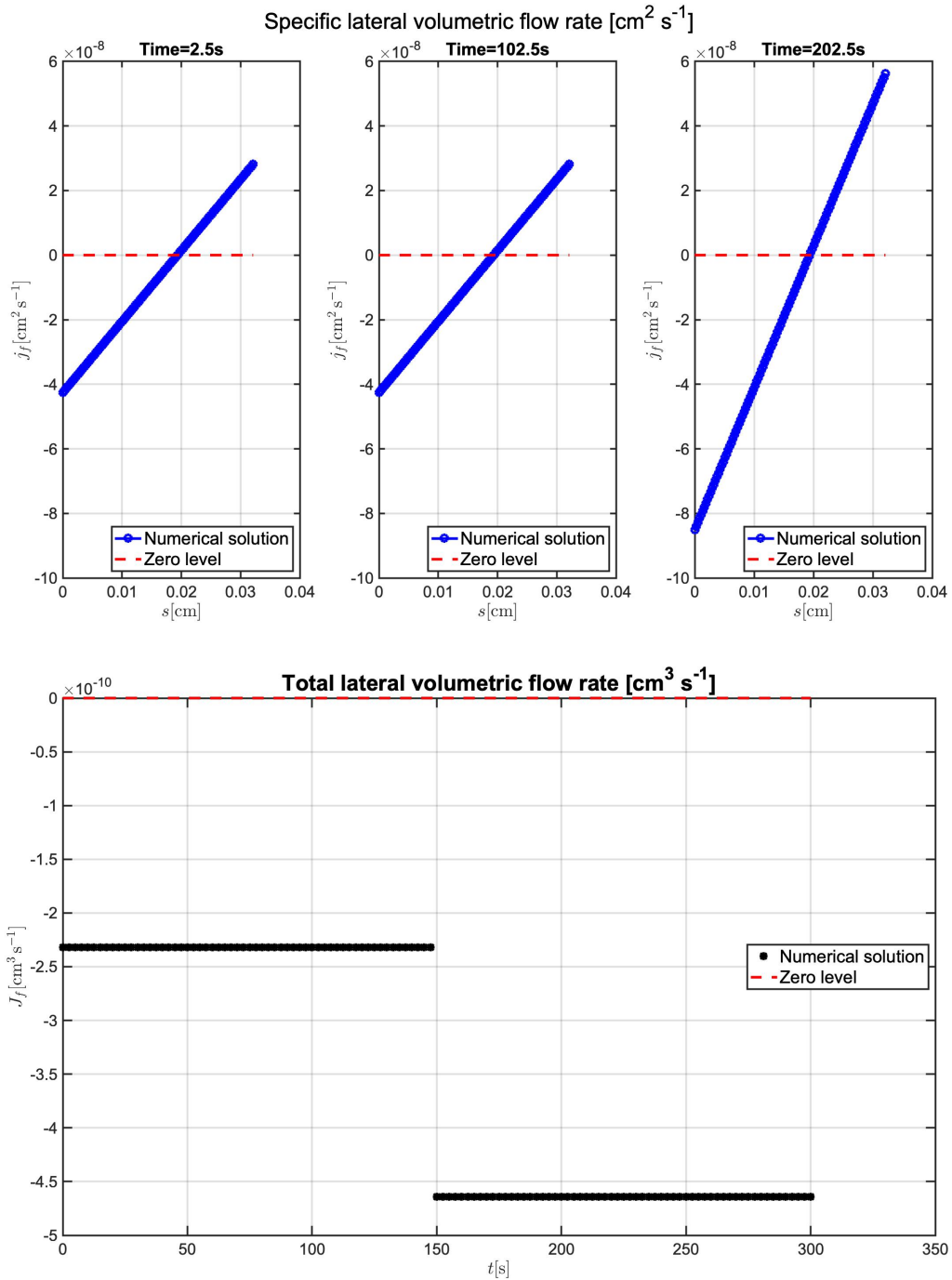


Figure 6.13: Visualization of specific lateral volumetric flow rate j_f (three time snapshots at the top) and of total lateral volumetric flow rate J_f (plotted in time at the bottom), in the case where the Atrial natriuretic peptide is administered after 150 s. The total lateral volumetric flow rate J_f doubles in magnitude, indicating that the capillary absorbs about twice as amount of fluid. The slope of the specific lateral volumetric flow rate j_f becomes steeper.

7 | Conclusions and future developments

In this thesis we developed a time-dependent mathematical model of fluid and protein transport in microvascular vessels, with the aim of investigating fluid exchanges between the vascular system and body tissues. The model was a system of nonlinearly coupled partial differential equations and we used fixed-point iterations to decouple the equations for the fluid part from the equations for the protein part. The first finding was that this decoupling is numerically stable since the fixed-point method keeps the energy bounded. Further, Backward Euler method, together with Galerkin finite element approximation, resulted in a convergent computational algorithm, as proven by the error analysis performed in the test case in Chapter 4.

As far as the physiological results are concerned, the main finding was that the protein leakage, due to a sudden decrease in the reflection coefficient, was able to induce an osmotic gradient sufficiently large to generate the pathological condition of edema. In this context, we also studied how hormones that affect hydraulic conductivity, as for example the Atrial natriuretic peptide, could provide a possible treatment. Indeed, they may promote reabsorption in venular capillaries of the microvascular network.

The major limitation of this work is that the current time-dependent model focuses on a single vessel. This results in a restricted view of the global fluid exchanges taking place in an entire microvascular network, and also requires an approximation of the boundary conditions. Of course, future work will need to extend this non-stationary model to the full network of capillaries. Another interesting development might be the testing of new methods to decouple the fluid-protein problem. A method such as operator splitting for example, which does not need to perform iterations at each time step, might be more efficient. However, its numerical stability remains a critical issue, although the energy balances derived in this thesis are an excellent starting point for tackling this new challenge.

Bibliography

- [1] K. Aukland and R. K. Reed. Interstitial-lymphatic mechanisms in the control of extracellular fluid volume. *Physiol Rev*, 73:1–78, 1993.
- [2] L. N. Cueni and M. Detmar. The lymphatic system in health and disease. *Lymphat Res Biol*, 6:109–122, 2008.
- [3] K. M. Druey and P. R. Greipp. Narrative review: the systemic capillary leak syndrome. *Ann Intern Med*, 153:90–98, 2010.
- [4] D. Goldman. Theoretical models of microvascular oxygen transport to tissue. *Microcirculation*, 15:795–811, 2008.
- [5] G. Guidoboni, N. M. Marazzi, J. Fraser, R. Sacco, K. Palaniappan, and V. H. Huxley. Fluid and protein exchange in microvascular networks: Importance of modelling heterogeneity in geometrical and biophysical properties. *J Physiol*, 599(20):4597–4624, 2021.
- [6] A. C. Guyton and J. E. Hall. The microcirculation and the lymphatic system: Capillary fluid exchange, interstitial fluid, and lymph flow. *Textbook of Medical Physiology*, 11th ed., 2006.
- [7] N. Herring and D. Paterson. Levick’s introduction to cardiovascular physiology. *CRC Press, Taylor Francis Group*, 2018.
- [8] A. Krogh. Studies on the capillariometer mechanism: I. the reaction to stimuli and the innervation of the blood vessels in the tongue of the frog. *J Physiol*, 53:399–419, 1920.
- [9] J. R. Levick. Revision of the starling principle: new views of tissue fluid balance. *J Physiol*, 557, 2004.
- [10] D. Meyer and V. Huxley. Differential sensitivity of exchange vessel hydraulic conductivity to atrial natriuretic peptide. *Am J Physiol*, 1990.

- [11] A. Popel. Theory of oxygen transport to tissue. *Crit Rev Biomed Eng*, 17:257–321, 1989.
- [12] A. Quarteroni. Modellistica numerica per problemi differenziali. *Springer Milano*, 2006.
- [13] R. Sacco, G. Guidoboni, and A. G. Mauri. A comprehensive physically based approach to modeling in bioengineering and life sciences. *Elsevier*, 2019.
- [14] J. Scallan, V. H. Huxley, and R. J. Korthuis. Capillary fluid exchange: Regulation, functions, and pathology. *San Rafael (CA): Morgan Claypool Life Sciences*, 2010.
- [15] D. Scharfetter and H. Gummel. Large-signal analysis of a silicon read diode oscillator. *IEEE Trans Electron Devices*, 16:64–77, 1969.
- [16] J. Shen and J. Xu. Unconditionally positivity preserving and energy dissipative schemes for poisson–nernst–planck equations. *Numerische Mathematik*, 148:671–697, 2020.
- [17] E. H. Starling. On the absorption of fluids from the connective tissue spaces. *J Physiol (Lond)*, 19:312–326, 1896.

List of Figures

1.1	Microlymphatic vessels intertwine vascular capillaries in a cellular tissue.	3
1.2	Capillary—interstitium—lymphatic fluid and protein exchange system depicting the Starling forces acting across the microvascular wall.	5
1.3	Graph of volume flux per unit surface area on hydrostatic pressure.	6
2.1	Schematic representation of the vessel. The vessel is assumed to be a cylinder of length L and constant circular cross-section of radius R . A local system of cylindrical coordinates is introduced, where r , s and θ denote the radial, axial and angular coordinates, respectively. The model includes fluid (blue shading) and proteins (orange dots), which are transported along the vessel and are exchanged with the tissue (red shading) across the permeable vessel walls (orange shading).	10
4.1	Geometrical notation and unit normal vectors.	38
4.2	3D plot of the pressure exact solution (left side) compared to the pressure numerical solution (right side) in the domain $(0, L) \times (0, T)$ with $T = 3 \cdot 10^{-9} s$ and $L = 0.0534 \text{ cm}$	44
4.3	3D plot of the axial volumetric flow rate exact solution (left side) compared to the axial volumetric flow rate numerical solution (right side) in the domain $(0, L) \times (0, T)$ with $T = 3 \cdot 10^{-9} s$ and $L = 0.0534 \text{ cm}$	45
4.4	The pressure numerical solution (red dots) compared to the pressure exact solution (black line) in the domain $(0, L)$ with $L = 0.0534 \text{ cm}$ at three different time instants, in particular $T_1 = 5 \cdot 10^{-11} s$, $T_2 = 1.05 \cdot 10^{-9} s$ and $T_3 = 2.05 \cdot 10^{-9} s$	45
4.5	The axial volumetric flow rate numerical solution (red dots) compared to the axial volumetric flow rate exact solution (black line) in the domain $(0, L)$ with $L = 0.0534 \text{ cm}$ at three different time instants, in particular $T_1 = 5 \cdot 10^{-11} s$, $T_2 = 1.05 \cdot 10^{-9} s$ and $T_3 = 2.05 \cdot 10^{-9} s$	46

4.6	L_∞ - error for pressure p and axial volumetric flow rate q_f , computed by progressively refining the time mesh, decreases linearly. Specifically, we set a time interval $(0, T)$ with $T = 3 \cdot 10^{-7} s$ considering a refinement vector of 10, 20, 40, 80, 160, 320 mesh time elements.	48
4.7	L_2 - error for pressure p and axial volumetric flow rate q_f , computed by progressively refining the time mesh, decreases linearly. Specifically, we set a time interval $(0, T)$ with $T = 3 \cdot 10^{-7} s$ considering a refinement vector of 10, 20, 40, 80, 160, 320 mesh time elements.	48
4.8	L_∞ - error for pressure p and axial volumetric flow rate q_f , computed by progressively refining the space mesh, decreases quadratically. Specifically, we set a space interval $(0, L)$ with $L = 0.0534 \text{ cm}$, considering a refinement vector of 10, 20, 40, 80, 160, 320 mesh space elements.	49
4.9	L_2 - error for pressure p and axial volumetric flow rate q_f , computed by progressively refining the space mesh, decreases more than linearly. Specifically, we set a space interval $(0, L)$ with $L = 0.0534 \text{ cm}$, considering a refinement vector of 10, 20, 40, 80, 160, 320 mesh space elements.	50
5.1	Fixed-point energy plotted over time. The energy is computed at each time step n , starting from the numerical solution once the fixed-point method has reached convergence.	57
6.1	Visualization in the nonpathological case of hydrostatic pressure p (top row) and protein concentration C (bottom row) plotted in space at three different time instants ($T_1 = 2.5 \text{ s}$, $T_2 = 102.5 \text{ s}$ and $T_3 = 202.5 \text{ s}$). Under normal conditions, the shape of the hydrostatic pressure p over time remains linear, whereas the protein concentration C remains constant and equal to the basal value of 0.025 g cm^{-3}	62
6.2	Visualization in the nonpathological case of total lateral volumetric flow rate J_f (top) and total lateral mass flow rate J_p (bottom) plotted in time. Under normal conditions, they remain constant over time. The positive value of J_f indicates that fluid filtration dominates over reabsorption, as expected in an arterial capillary. The low value of J_p means that in the nonpathological case the protein flux is negligible.	63

6.3 Visualization in the nonpathological case of specific lateral volumetric flow rate j_f (top row) and specific lateral mass flow rate j_p (bottom row) plotted in space at three different time instants ($T_1 = 2.5\text{ s}$, $T_2 = 102.5\text{ s}$ and $T_3 = 202.5\text{ s}$). Under normal conditions, the shape of j_f remains linear over time, whereas j_p remains constant, reflecting the behaviour of concentration C . The point of intersection between j_f (circled blue line) and the zero level (red dotted line) is the so called Starling equilibrium, a physical condition of balance between the hydrostatic and osmotic pressure differences.	64
6.4 Visualization over time of the protein reflection coefficient σ assumed in the pathological scenario in which sudden structural membrane changes occur. At the midpoint of the time interval, σ undergoes a sudden decrease from the basal value of 0.8 to the pathological value of 0.01.	65
6.5 Visualization in the pathological case of hydrostatic pressure p (top row) and protein concentration C (bottom row) plotted in space at three different time instants ($T_1 = 2.5\text{ s}$, $T_2 = 102.5\text{ s}$ and $T_3 = 202.5\text{ s}$). Hydrostatic pressure p remains linear over time, as in the nonpathological case, whereas the concentration C decreases over time due to protein flow into the tissue.	67
6.6 Visualization in the pathological case of total lateral volumetric flow rate J_f (top) and total lateral mass flow rate J_p (bottom) plotted in time. J_f increases from a rate of $1.2 \cdot 10^{-10} \text{ cm}^{-3} \text{ s}^{-1}$ to $5 \cdot 10^{-10} \text{ cm}^{-3} \text{ s}^{-1}$, because of the osmotic gradient generated by the protein flow into the tissue. J_p undergoes a huge increase from $3.57 \cdot 10^{-13} \text{ g s}^{-1}$ to a value of $1.34 \cdot 10^{-10} \text{ g s}^{-1}$. As expected, once this increase of 3 orders of magnitude is recorded, J_p decreases slightly, since a lower amount of protein remains in the vascular space.	68
6.7 Visualization in the pathological case of specific lateral volumetric flow rate j_f (top row) and specific lateral mass flow rate j_p (bottom row) plotted in space at three different time instants ($T_1 = 2.5\text{ s}$, $T_2 = 102.5\text{ s}$ and $T_3 = 202.5\text{ s}$). After σ decreases, the Starling equilibrium point, intersection between j_f (circled blue line) and the zero level (red dotted line), is lost and the capillary switches from filtration and reabsorption mode to filtration-only action. Concerning j_p , it increases suddenly due to the structural membrane changes and then decreases slightly over time, since a lower amount of protein remains in the vascular space.	69

6.8 Visualization over time of the concentration boundary conditions $C(0, t)$ and $C(L, t)$. They increase 70 times higher than the basal value after 175 s, as a treatment to the pathological membrane change which occurs after 150 s.	70
6.9 Visualization of the time evolution of total lateral volumetric flow rate J_f (top) and total lateral mass flow rate J_p (bottom), in the case where new proteins are injected inside the capillary. The lateral volumetric flow rate J_f rises to pathological levels before being scaled down by the injection of protein in the capillary. The lateral mass flow J_p increases compared to the pathological case where no actions were taken.	72
6.10 Visualization of the spatial profile of the lateral volumetric flow rate j_f (top row) and lateral mass flow rate j_p (bottom row) at three different time instants ($T_1 = 2.5$ s, $T_2 = 102.5$ s and $T_3 = 202.5$ s), in the case where new proteins are injected inside the capillary. The Starling equilibrium point, intersection between j_f (circled blue line) and the zero level (red dotted line), is recovered with respect to the pathological case shown in Figure 6.7. The specific lateral mass flow j_p increases over time, while remaining constant in space.	73
6.11 Visualization over time of the hydraulic conductivity L_p , which subjected to the action of the Atrial natriuretic peptide, increases twofold from the basal value of $5 \cdot 10^{-7} \text{ cm s}^{-1} \text{ cmH}_2\text{O}^{-1}$, assumed for venular capillaries. . .	74
6.12 Visualization in the nonpathological case of specific lateral volumetric flow rate j_f (three time snapshots at the top) and of total lateral volumetric flow rate J_f (plotted as a function of time, bottom). In a venular capillary re-absorption dominates over fluid filtration. Indeed the Starling equilibrium point, intersection between j_f (circled blue line) and the zero level (red dotted line), is to the right of the vessel midpoint and the total volumetric flow rate J_f is negative over time.	75
6.13 Visualization of specific lateral volumetric flow rate j_f (three time snapshots at the top) and of total lateral volumetric flow rate J_f (plotted in time at the bottom), in the case where the Atrial natriuretic peptide is administered after 150 s. The total lateral volumetric flow rate J_f doubles in magnitude, indicating that the capillary absorbs about twice as amount of fluid. The slope of the specific lateral volumetric flow rate j_f becomes steeper.	76

List of Tables

2.1	Summary of model variables and parameters. The table distinguishes among quantities that vary within the vessel or are constant.	22
4.1	Summary of physical dimensions and physiological properties of the capillary adopted in the numerical results.	43
4.2	Order of convergence of the errors computed by progressively refining the time mesh.	47
4.3	Order of convergence of the errors computed by progressively refining the space mesh.	50

List of Symbols

Description	Symbols	Unit
<i>Quantities that vary within the vessel</i>		
Axial coordinate along the length	s	[cm]
Time	t	[s]
Hydrostatic pressure	$p(s, t)$	[cmH ₂ O]
Protein concentration	$C(s, t)$	[g cm ⁻³]
Osmotic pressure	$\pi(s, t)$	[cmH ₂ O]
Axial volumetric flow rate	$q_f(s, t)$	[cm ³ s ⁻¹]
Specific lateral volumetric flow rate	$j_f(s, t)$	[cm ² s ⁻¹]
Axial mass flow rate	$q_p(s, t)$	[g s ⁻¹]
Specific lateral mass flow rate	$j_p(s, t)$	[cm ⁻¹ g s ⁻¹]
<i>Quantities that are constant</i>		
Radius of the vessel	R	[cm]
Length of the vessel	L	[cm]
Partial density of the fluid phase	ρ_{fp}	[g cm ⁻³]
Water dynamic viscosity	μ_w	[cmH ₂ O s]
Hydraulic conductivity of the membrane	L_p	[cm s ⁻¹ cmH ₂ O ⁻¹]
Protein reflection coefficient of the membrane	σ	[·]
Solute permeability of the membrane	P_d	[cm s ⁻¹]
Protein diffusion coefficient	D_{pt}	[cm ² s ⁻¹]
Shape factor	γ	[·]
Lateral volumetric flow rate	J_f	[cm ³ s ⁻¹]
Lateral mass flow rate	J_p	[g s ⁻¹]

